SHARE PAPRIKA-Italy

PAPRIKA –
CryosPheric responses to Anthropogenic PRessures in the
HIndu Kush - Karakoram -HimalayA regions:
impacts on water resources and Availability

Period of activity: July 2010 - June 2013

Coordination:
A. Provenzale, E. Palazzi, ISAC-CNR

Final Report of the Project

Editing by: Ev-K2-CNR

Final Report of the SHARE-Paprika-Italy project

ISBN: 9788890539848

Participating Institutions

Institute of Atmospheric Sciences and Climate (ISAC-CNR)

A. Provenzale, P. Bonasoni, E. Palazzi, J. von Hardenberg, S. Terzago, L. Filippi, P. Cristofanelli, A. Marinoni, D. Putero, R. Duchi, S. Decesari, C. Cagnazzo, F. Fierli, S. Bucci, F. Viterbo, A. Parodi

Institute of Ecosystem Study (ISE-CNR)

A. Lami, M. Rogora

University of Milan, "A. Desio" Earth Sciences Department (UNIMI)

C. Smiraglia, G. Diolaiuti, R. Ambrosini, M. Belò, L. Bonetti, C. D'Agata, C. Compostella, D. Maragno, C. Mihalcea, U. Minora, B. Mosconi, A. Senese

Bavarian Academy of Sciences and Humanities (BAW)

C. Mayer, A. Lambrecht

Politecnico di Milano (POLIMI)

R. Rosso, D. Bocchiola, A. Bianchi, A. Soncini, G. Confortola, E. Nana

International Centre for Theoretical Physics (ICTP)

F. Solmon, F. Giorgi

Istituto Nazionale di Geofisica e Vulcanologia (INGV)

S. Urbini, A. Zizzirotti, I.E. Tabacco, L. Cafarella, J. Baskaradas

Euro-Mediterranean Center on Climate Change (CMCC)

C. Cagnazzo, M. D'Errico, A. Bellucci

EV-K2-CNR

E. Vuillermoz, G. P. Verza, F. Mari, M. Gallo, D. Milanesi, V. Carminati, P. Stocchi

Table of contents

Executive Summary: Key results of the PAPRIKA-Italy project

The main focus area of PAPRIKA-Italy is the Karakoram region, in particular the Baltoro glacier and the upper Indus basin in northern Pakistan. Another focus of PAPRIKA-Italy is the Changri Nup glacier area, lying on a lateral valley of the Khumbu region in Nepal, the principal area where PAPRIKA-France was active. A fruitful collaboration between PAPRIKA-Italy and PAPRIKA-France took place during the three years of project activities, especially in the Khumbu region, to share and discuss the research results in terms of modeling activities and of the information that can be extracted from experimental data. A particularly important issue requiring a joint effort was to quantify the differences between the behaviour of the retreating glaciers in eastern Himalaya and those of the Karakoram, whose response is still largely unknown.

The main goals of the PAPRIKA-Italy project, both scientific and targeted to address societal challenges and needs, are

- Obtain a **quantitative assessment** of the current state of the **atmospheric composition and circulation**; **aerosol** load, deposition and chemical properties; **glacier status**, mass/energy balance and flow estimates; hydrologic characteristics, including **water quantity and quality**, in the two study areas, with an enhanced observational effort in the Baltoro glacier region.
- Provide an ensemble of **integrated modeling tools**, based and validated on field and remotely sensed data, **to obtain quantitative and reliable estimates of water availability and climate change impacts** on agriculture, environment and ecosystems in the coming decades (2010-2050).
- Develop **strategies for capacity building, dissemination and information transfer** to policy makers, in collaboration with the SEED project.

Following these targets, the PAPRIKA-Italy activities were structured in four main themes - Observations, Modeling, Impacts, and Capacity building and dissemination - which were organized in several specific work packages. Here we provide an overview of the main results obtained by the PAPRIKA-Italy project.

A glacier inventory for the Central Karakoram National Park (CKNP)

The Central Karakoram Nation Park is a recently (2009) established protected natural area in the Karakoram region. The park area occupies ca. 13 000 km^2, and roughly 40% of it is covered by ice. An analysis of the satellite data performed during PAPRIKA allowed to retrieve information on the variations, during the years 2001-2010, of the ice-covered areas, supra-glacial debris coverage, and snow cover in the CKNP area, to draw up an up-to-date inventory of glaciers and their characteristics and to better understand the behavior of the cryosphere and of its changes in this region. The CKNP glacier inventory highlighted that glaciers in this area have been rather stable in the last decade, confirming the anomalous behavior of the Karakoram glaciers. About 700 glaciers in the CKNP area were analyzed, and no significant area change between 2001 and 2010 was detected, owing to the interplay of meteorological conditions (increase in winter precipitation and

decrease in summer temperatures, both contributing to snow and ice preservation) and surface glacier characteristics. The analysis of satellite images showed that, in the thaw season, an increase of the snow-covered area occurred at high elevations (~5500 m a.s.l.), protecting glaciers from melting since fresh snow, with its high albedo, reflects the incoming solar radiation. At lower elevations, where snow is seldom present and ablation takes place, making the glaciers vulnerable and exposed to melting, another factor comes into play contributing to glacier stability: the presence of a thick supra-glacial debris cover. All these factors together are thought to be responsible for pushing the CKNP glacier mass balance towards positive or neutral values.

It is also worth pointing out that much of the CKNP and Karakoram glaciers behavior has still to be fully understood and that, despite satellite measurements are a valuable and precious source of information, the availability of in-situ snow depth data in the accumulation areas at highest altitudes would considerably improve our knowledge of the Karakoram cryosphere.

Hydrological observations in the upper Indus basin: water quantity and water quality

During PAPRIKA-Italy, specific activities aimed at monitoring the quantity and quality of water originating from the Karakoram glaciers were performed. Ice and snow melting due to increased temperatures may lead to changes in discharge, and to an increase in soil microbial activity and mineral weathering rates, causing enhanced nutrient and solute fluxes to mountain lakes and streams. Four dedicated hydrological campaigns were performed to assess the quantity and quality of water, specifically in April and July 2011, May 2012 and April 2013. Two permanent hydrometric stations were installed at two key sites, the Shigar Bridge and Paiju, providing continuous measurements of water level and, therefore, of discharge, and of water chemistry. The analysis of the three-year discharge data collected at the two hydrometric stations provided information on the hydrological behavior of the Shigar basin, used to calibrate the hydrological model implemented during the project. In terms of water chemistry, the analyses indicated a good quality of surface waters in the study area, with low levels of nutrient and organic substances, and very low concentrations (mostly below the detection limit of the employed measurement device) of toxic metals such as Cu, Cr, Ni, Cd and Pb. Water chemistry proved to be mainly controlled by land cover (bedrock lithology) and hydrological factors (dilution/concentration processes in relation to the amount of water). A contribution of atmospheric deposition processes to the nitrogen content of water samples (mainly as NO_3) could not be excluded: nitrate, in fact, is usually absent in surface waters at remote location, where direct anthropogenic input can be excluded.

Quantitative assessment of the atmospheric composition in the Baltoro glacier area, and installation of a permanent climate station in Northern Pakistan

The current state of the atmospheric composition variability in the Baltoro glacier region, both in terms of pollutant gases and aerosol particles and their relationship with the atmospheric circulation, was assessed during the project to obtain information on short- and long-lived climate forcing factors in this remote mountain area. To this aim, two dedicated experimental campaigns were performed at Urdukas (35°43'N, 76°17'E, 3926 m a.s.l.) and Askole (35°40’N, 75°48’E, 3015 m a.s.l.) in summer 2011 and 2012, respectively. Akole is a village (about 300 inhabitants) located in the Braldu valley on the route to the Baltoro Glacier, while Urdukas is distant more than 40 km

from Askole and it is located along the Baltoro Glacier; both sites are well suited for investigating the transport processes which can occur along the valley and the possible influence of local-regional anthropogenic emissions in affecting the atmospheric composition of this pristine environment.

During summer 2011, aerosol measurements at Urdukas revealed relatively low PM10 values on average (7.7 ± 7.1 $\mu g/m^3$), with episodic enhancements in the aerosol load (an event of 300 $\mu g/m^3$ was detected) due to transport of mineral dust from the Taklimakan desert. The experimental campaign carried out at Askole in summer 2012 indicated that domestic combustion could represent a possible systematic source of contamination in the valley. Excluding these local contamination events, the mountain thermal wind regime was found to dominate the diurnal variability of particle number concentration (Np), Ozone (O_3) and Carbon Dioxide (CO_2). Nevertheless, the variability of these observed climate forcing factors appeared to be dominated by day-to-day changes. Part of the day-to-day atmospheric composition variability can be ascribed to synoptic circulation variability. In particular, the observed low O_3 and high CO_2 values were linked to possible air-mass transport from South Asia and the Taklamakan desert area. Long-range transport from South Asia was found to be a major source of fine particles in the Karakoram, while higher O_3 values have been mostly tagged with air-masses possibly coming from the free troposphere.

In addition to these field campaigns, a permanent climate station, powered by solar energy, was installed is summer 2013 in the Pakistani Deosai National Park, at 4200 m a.s.l., in collaboration with the Water and Power Development Authority (WAPDA) of Pakistan, the Pakistan Meteorological Department (PMD) and in synergy with SHARE-ABC. The station is operating since September 2013 (a battery failure in November 2013 caused the suspension of the measurements for about a month) measuring pollutant/climate-altering compounds (ozone, black carbon, aerosol size distribution) and standard meteorological parameters.

From climate projections in the HKKH region to water availability scenarios

Reliable estimates of water availability in future decades in the HKKH region require the implementation and use of a modeling chain starting from the output of Global Climate Models (GCMs), which provide climate scenarios at coarse resolution, going through a procedure to downscale the GCM projections to provide a higher-resolution estimate of climatic conditions, and finally running a hydrological model to simulate the hydrological response at basin scales. Downscaling of the GCM outputs, performed using different techniques, is a necessary step to obtain climatic information at the high spatial and temporal resolutions required for running hydrological and impact models.

During PAPRIKA-Italy, the output of state-of-the-art GCMs, used in the fifth IPCC assessment report (*AR5 2013),* was analyzed to provide climate projections for the whole HKKH region under different emission scenarios. In particular, climatic variables such as temperature, precipitation and snow depth were considered and, after validating the models against observed data in the historical period, the climate conditions estimated by the models for the twenty-first century were analyzed.

The GCMs projections indicated positive summer precipitation changes in the Karakoram and in the eastern Himalaya for both near (2021-2050) and far (2071-2100) future with respect to the

historical baseline (1971-2000), consistent with a gradual increasing trend in summer precipitation throughout the twenty-first century found for these regions. In general, GCM projections of winter precipitation changes turned out to be more scattered than for summer (in some case, half of the models gave positive precipitation changes and the other half negative changes in winter), with a slight prevalence towards drier future condition, except for the Karakoram region, were positive winter precipitation changes in the nearest future are expected.

Future projections of snow depth indicated a general decrease throughout the winter season in both Karakoram and Himalaya regions, which is strongest in the most extreme emission scenario. For the Himalaya region, in particular, the models indicated an expected shift in the snow depth maximum from March to February, resulting in an earlier spring snow melt and a consequent shift in the timing of water discharge.

A glacio-hydrological model, driven by high-resolution climate scenarios obtained after downscaling the GCM projection outputs, was run to investigate future ablation flows from the Shigar river, a glacierized watershed in the Karakoram mountains, and provided a range of possibilities for the expected future changes in different components of the hydrological cycle in this catchment. The hydrological projections for the Shigar basin indicated a strong decrease of both ice-covered areas (up to -45% in the most extreme emission scenario) and ice volume (up to -91%) from mid-century onwards. Consistently, a negative trend in the in stream flows and discharge was projected for the second half of the century, which is opposite to the trend projected for the first half of the century, where the hydrological model simulations indicated an increasing in stream flow trend, in a range from +5% to +25% depending on the emission scenario.

Summary of Work packages

WP	WP Title		Activities	Participants
WP 1	**Cryospheric observations**	1.1	Cryospheric resources, snow cover contribution and glacier melting (quality and quantity) on Baltoro (Pakistan) and on Changri Nup (Nepal). On this latter also meltwater discharge measurements	UNIMI / BAW
		1.2	Feasibility study on the determination of ice thickness of the Baltoro glacier (Karakorum) by radar measurements	INGV
		1.3	Determination of glacier properties and ice flow by remote sensing	UNIMI / BAW
WP 2	**Hydrological observations**	2.1	Hydrological characteristics and water quantity	POLIMI
		2.2	Water quality	ISE
WP 3	**Atmospheric observations**	3.1	Physical and chemical characterization of aerosol: absorption, scattering, size distribution, atmospheric optical depth, chemistry; atmospheric deposition	ISAC / Ev-K2-CNR
		3.2	Impact of anthropogenic (ABC) and natural (STE) processes on surface ozone concentrations and contribution to radiative forcing	ISAC
		3.3	Variability of the atmospheric circulation (from time series and new in-situ measurements)	ISAC / Ev-K2-CNR
WP 4	**Integrated Climate-glacier-water modelling**	4.1	Global climate simulations and atmospheric variability, including aerosol transport	ISAC
		4.2	Regional climate modeling of the atmosphere/glacier/hydrosphere system, including sources and transport of aerosols at regional scale and sub-grid scale parameterizations based on stochastic downscaling methods	ICTP / ISAC
		4.3	Modeling the interaction between snow-pack, radiation and the absorbing material deposited in the snow. Modeling the interaction between ice melting, ice surface features, debris coverage properties and albedo	ISAC / ICTP / UNIMI / POLIMI
		4.4	Development of a hydrological model for the upper basin of the Indus river (Pakistan) and for the Koshi basin (Nepal)	POLIMI
WP 5	**Future scenarios on water availability**	5.1	Cryospheric characteristics in regional climate change scenarios	ISAC / ICTP / UNIMI
		5.2	Hydrological characteristics in regional climate change scenarios	ISAC/ ICTP / POLIMI
WP 6	**Impacts and adaptation (SEED project)**	6.1	Impacts of future streamflow regimes on water resources for the communities	SEED
		6.2	Impacts of climate and seasonal water availability on the ecosystem	SEED
WP 7	**Capacity building**	7.1	Capacity building, dissemination and information to policy makers	Ev-K2-CNR / ISAC / UNIMI

WP1: Cryospheric observations

C. Smiraglia, G. Diolaiuti, U. Minora, C. D'Agata, D. Maragno, B. Mosconi,
A. Senese, C. Compostella (UNIMI)

C. Mayer (BAW)

E. Vuillermoz, U. Minora (EvK2CNR)

D. Bocchiola and co-workers (POLIMI)

1.1 Introduction

During the PAPRIKA project the UNIMI and BAW team carried out three field missions in the Pakistani Karakoram aimed at measuring supraglacial debris cover thickness; evaluating magnitude and rates of ice melt; taking snow samples for isotopic analysis and for evaluation of glacier snow water equivalent (SWE); performing radar investigations for evaluation of ice thickness; carrying out GNSS (Global Navigation Satellite System) surveys to assess glacier flow. Whenever possible the field campaigns were performed in the same time windows chosen for the hydrological surveys thus taking advantage from the presence of researchers and technicians from POLIMI. Moreover the UNIMI team in close cooperation with personnel from POLIMI also performed a field mission in Nepal, in order to acquire ablation data on the upper (debris free) sector of the Changri Nup Glacier and to install a hydrometer for measuring meltwater amount deriving from bare ice and snow melt. These activities have provided important data for the modeling activities foreseen within WP1, WP4 and WP5.

1.2 Summary of the field campaigns

All field campaigns were carried out in spring and summer: surveys in Pakistan took place on July 2011, May 2012 and July 2013, while mission in Nepal on April 2012. Table 1.1 resumes the main activities carried out during the field missions.

1.3 Ablation and debris measurements, topographic and geophysical surveys in the Pakistani area

All field measurements were essential for calibrating and validating the models developed during the project to assess melting amount and water discharge. Pictures in Figs. 1.1-1.7 summarize the various experimental activities performed during the project.
In addition, processing and analysis of remote sensing data were performed to describe glacier coverage and features on the Central Karakoram National Park (CNKP) area, another focus area and representative sector of the glacierized Karakoram chain.

Table 1.1 Activities performed during the field missions

Location	***Survey details***
Pakistan: Baltoro Glacier Tongue	***2011*** *Ablation measurements by ablation stakes drilled into the ice up to 8 m depth by a steam drill; GNSS surveys to evaluate ice flow; Debris measurements to evaluate thickness and distribution along the glacier tongue* ***2012*** *Ablation measurements by ablation stakes (re-drilling whenever necessary the 2011 stakes), debris measurements and sampling* ***2013*** *Ablation measurements by ablation stakes (re-drilling whenever necessary the 2012 stakes), debris measurements and sampling to perform Lab analysis in Italy (grain size, SEM, chemical composition, TOC, etc..), radar surveys to evaluate ice thickness*
Pakistan: Baltoro upper basins (accumulation areas)	***2011*** *Snow sample collection for isotopic analysis and performing snow pits to evaluate SWE, radar measurements to assess snow thickness* ***2013*** *Snow sample collection for isotopic analysis and performing snow pits to evaluate SWE, radar measurements to assess snow and ice thickness*
Pakistan: Liligo Glacier	***2011*** *GNSS surveys to evaluate snout position to support our analysis of Liligo Glacier surge-type events*
Nepal: Changri Nup Glacier	***2012*** *ablation surveys at the glacier debris free sector (up to 5700 m asl); Installation of a Hydrometer to measure meltwater discharge from the glacier debris free part*

Figure 1.1: Drilling an ablation stake with the Heucke steam drill at Concordia – Baltoro Glacier

Figure 1.2: Drilling an ablation stake with the Heucke steam drill at Concordia – Baltoro Glacier

Figure 1.3: Drilling an ablation stake with the Heucke steam drill at Khoburtse Glacier

Figure 1.4: An ablation stake installed at at Khoburtse Glacier. This stake is also equipped with thermistors and data loggers to record debris temperature data along the debris vertical profile.

Figure 1.5: The GNSS Master station located at Urdukas (Baltoro Glacier). It was used as reference station to evaluate stake positions and then glacier surface velocity (the measurements were acquired twice, at the beginning and the end of the field work thus permitting a comparison of the surveyed data).The GNSS Master station was located close to the Share AWS (on the right in the photo).

Figure 1.6: Digging a snowpit at the Gasherbrum basin

Figure 1.7: Radar measurements to evaluate snow and firn depth at the Godwin Austen Glacier. A Gssi system was used equipped with a 400MHz antenna.

1.4 Remote sensing analysis to evaluate glacier coverage and features, and their recent changes in the CKNP area

A glacier inventory was developed (in collaboration with the SEED project, see also WP6 chapter and http://www.evk2cnr.org/cms/files/evk2cnr.org/Brochure_Seed.pdf) including all fundamental information on 700 glaciers located in the Central Karakoram National Park, a wide and representative sector of the Pakistani Karakoram. Glacier data derived from the analysis of 2001 and 2010 Landsat images and they permitted to describe the actual glacier coverage in the CKNP area and the changes undergone during the last decade.
The snow coverage in the 2001-2011 time window was analysed, through the processing of the satellite MODIS snow product, to evaluate the role of snow variability in driving glacier evolution.
The supraglacial debris coverage distribution over the whole CKNP area was analysed by applying a supervised classification of Landsat images as rock debris is largely indicated by the recent literature as a fundamental factor driving rates and magnitude of buried ice melt.

Table.1.2: Area coverage of glaciers within the CKNP according to satellite images (2001 and 2010) (columns 2 and 3). Surface area changes of the CKNP glaciers during 2001-2010 (column 4). Surface area changes of CKNP glaciers with respect to the 2001 class area coverage, and to total area change (columns 5 and 6 respectively). The area changes are computed considering each glacier according to the class it belonged to in 2001.

Size class [km²]	2001 Area [km²]	2010 Area [km²]	ΔA 2001-2010 [km²]	Glacier area change (%) with respect to the 2001 class value	Glacier area change (%) with respect to the 2001 total glacier change
<0.5	66	66	-0.1	-0.2	-0.4
0.5-1.0	99	100	0.2	0.2	0.8
1.0-2.0	170	171	0.2	0.1	0.8
2.0-5.0	230	232	1.6	0.7	6.0
5.0-10.0	246	247	0.4	0.2	1.5
10.0-20.0	236	238	1.9	0.8	7.1
20.0-50.0	525	526	0.2	0.0	0.8
>50.0	3012	3034	22.2	0.7	83.5
Total	**4587± 18**	**4613 ± 38**	**26.6 ± 42**		**100**

Landsat images displayed that the total supraglacial-debris-coverage was 977 km^2 ±138 km^2 in 2001, and 1070 km^2 ±194 km^2 in 2010, about 20% of the total ice covered area. When considering only the ablation area, the percentage rose up to 31 %. The accuracy of the surface comparison is ±238 km^2, then the change in the debris cover area of +92 km^2 falls within the error range. In spite of this non-significant area change, debris cover increment can be appreciated by comparison of two FCC images upon some selected glaciers (see Figure 1.9).
The maximum cover was found at 4300 m a.s.l., in the glacier ablation zone. Supraglacial debris increase may likely be labeled as another cause of the stable conditions of the Karakoram glaciers. In fact supraglacial debris coverage, whenever thicker than a "critical thickness" (*sensu Mattson et al., 1993*), could reduce buried ice melting rates (*Mihalcea et al., 2006*; *Hagg et al, 2008*; *Bocchiola et al., 2010; Sherler et al., 2011*). Potential sources of debris cover may have been rocky avalanches due to steep slopes, glacier dynamics, wind action and other factors. In particular, hillslope-erosion rates usually increase with hillslope angle, so the flux of rocky debris to the glacier surfaces and

therefore the formation of debris-covered glaciers are linked to steep (>25°) accumulation areas (*Sherler et al., 2011*), such as those present in the Karakoram range.

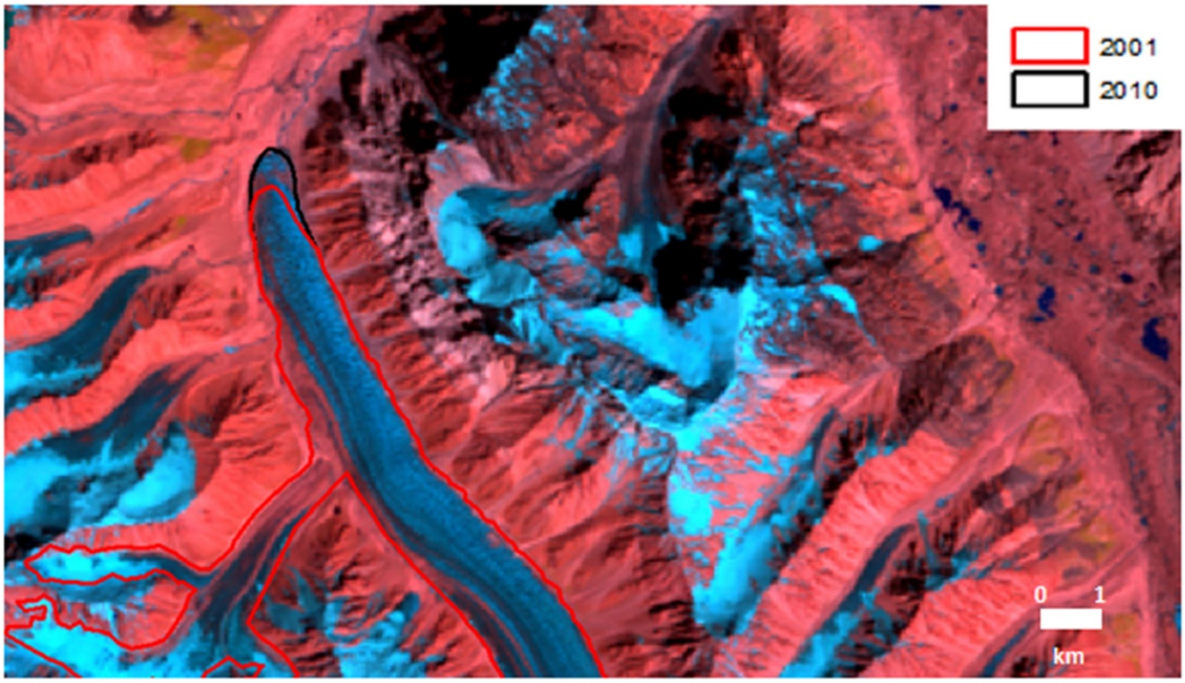

Figure 1.8. Example of an advancing glacier terminus near Braldu glacier from 2001-2010.

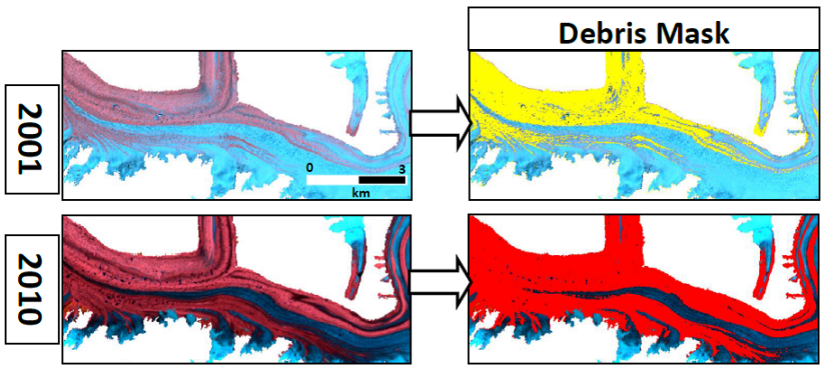

Figure 1.9. Supraglacial debris coverage change for 2001 (upper figures) and for 2010 (lower figures).

In Figure 1.10, we report average (2001-211) SCA_{LS}, or snow covered area in late Summer, as per altitude bins of 1000 m (i.e. 2000-3000 m a.s.l., etc.), refined into 500 m bins from 3000-6000 m a.s.l., where most of the snow dynamics likely occurs, and ELA is expected to dwell. We report within the radar plot snow cover areas as per aspect (8 bins of 45°), to illustrate variability of snow cover with slope orientation.

From Figure 1.11, one sees that on average 88% of the snow covered area at Fall is contained between 4000 and 6000 m a.s.l. ($SCA_{LS}^{\%}$), thus demonstrating how snow dynamics is mostly played in this altitude bin, and that such range of altitude is utmost critical, also in view of potential changes of snow cover in response to climate change. From the shape of SCA_{LS}^{*} curve one clearly sees how on average, above 5500 m a.s.l. or so and up to 8000 m a.s.l., snow cover at Fall is stably at 85% or so of the maximum seasonal value. Below this altitude, SCA_{LS}^{*} decreases quickly. $SCA_{Max}^{\%}$ indicates the contribution to snow cover of each altitude belt during Winter time, *i.e.*

when snow cover area reaches its largest value. The comparison of $SCA_{LS}^{\%}$ against $SCA_{Max}^{\%}$ quantifies the relative importance of the loss of snow cover at the end of Summer in each belt, i.e. as quantified by SCA_{LS}^{*}. One notices that the greatest cumulated loss of snow cover area (i.e. the vertical distance between $SCA_{LS}^{\%}$ and $SCA_{Max}^{\%}$) is reached towards an altitude of ca. 5000 m a.s.l. (ca. 20%), with decrease there above, meaning that areas above that altitude tend to contribute almost entirely to snow cover even after thaw. This is consistent with the pattern of SCA_{LS}^{*}, displaying swift increase above between 5000 and 5500 m a.s.l.

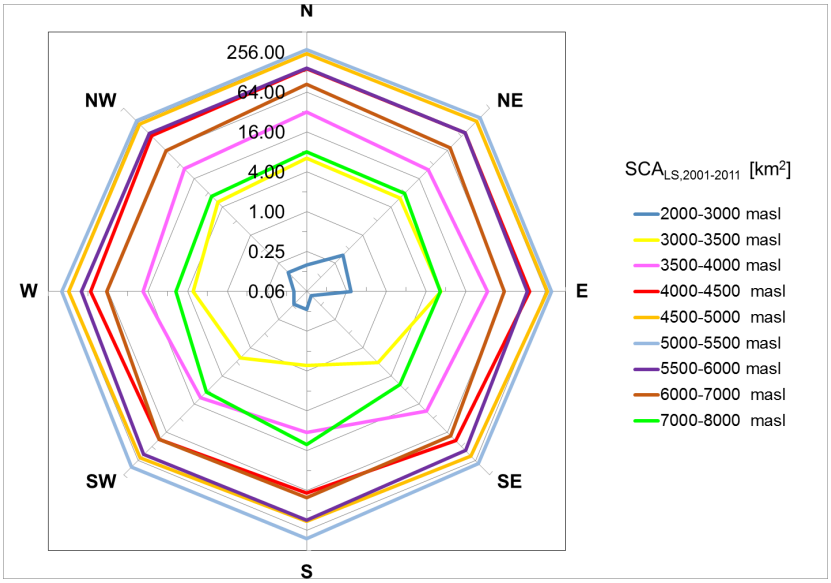

Figure 1.10. Average Snow Covered Area in late Summer (SCA_{LS}) as per altitude bins, and aspect. Logarithmic scale (base 2) is used to enhance small snow covered areas at very low (and very high) altitudes.

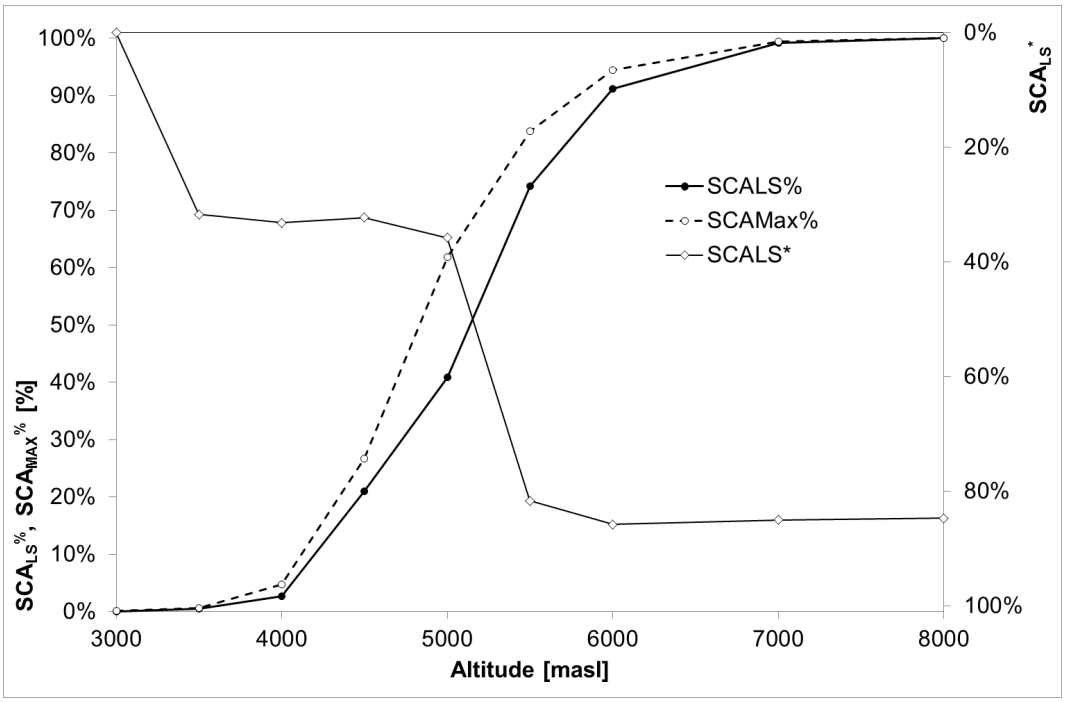

Figure 1.11. Distribution as per altitude bins of average snow covered area in late Summer with respect to the whole area $SCA_{LS}^{\%}$, of average snow covered area in late Summer SCA_{LS}^{*} with respect to greatest (maximum) snow covered area in that bin, and of the greatest snow covered area in each bin with respect to the sum of maximum values of snow covered areas in the whole park $SCA_{Max}^{\%}$. Logarithmic scale (base 2) is used to enhance small snow covered areas at very low (and very high) altitudes.

In Belt A (Fig. 1.11), a gain of +0.09 km^2 yr^{-1} (or 2 % of snow cover area per year), was observed. In Belt B, snow cover area increased by +2.35 km^2 yr^{-1}, or +0.6 % yr^{-1}. Belt C has increasing snow cover of +14.86 km^2 yr^{-1}, or +0.2 % yr^{-1}. These results are qualitatively similar to those of *Tahir et al. (2011),* and seem to confirm a slight gain of snow covered area within the upper Karakoram recently, albeit again no conclusions can be drawn about the significance of such gain, in view of the short time series.

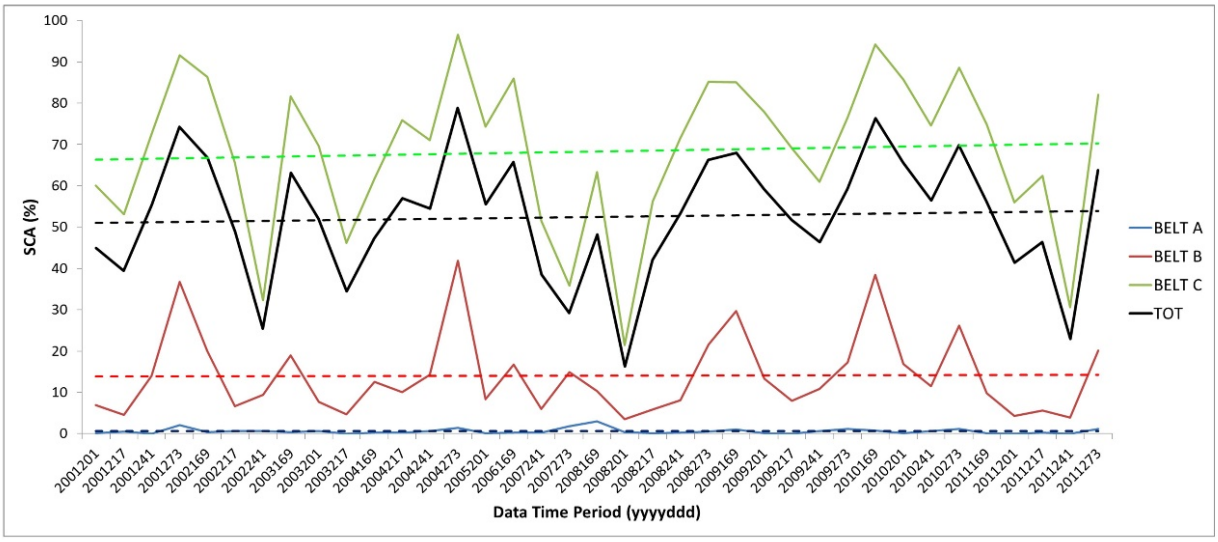

Figure 1.12. Snow cover distribution (SCA) in three different altitudinal zones of the CKNP for the May-September windows of 2000/2011 period. Data Time Period is given in years and Julian days.

Summarizing, the CKNP glacier inventory we developed indicates a situation of stationarity. Our close watch on CKNP for the last decade confirmed the exceptional behavior of glaciers in the Karakoram. In facts, we analyzed a sample of more than 700 glaciers, and we found no significant area change between 2001 and 2010 (+27 km^2 ± 42 km^2). Understanding the reasons of such anomaly is a paramount important. Observations on meteorological data revealed that precipitation has been substantially constant during the last 30 years in our study area, and yet the number of wet days has increased, particularly in Winter. In a Park where most of the lands lay between 4000 and 5000 m a.s.l. this could result into an increased supply of fresh snow, and fresh snow can then be long-lasting here because of the favorable temperature gradient. In addition, analysis of thermal data from 1980 to 2009 revealed a significant decrease in minimum Summer temperatures at Gilgit, which may be considered as representative of climate within the park area, thus potentially contributing to snow and ice preservation.

Analysis of MODIS images during 2001-2010 confirmed that an increase of SCA has occurred in thaw season. Snow cover protects glaciers from melting by reflecting incoming solar radiation. We could place late Summer snowline around 5500 m a.s.l., which roughly corresponds to the average altitude of the largest glaciers here (*i.e.* > 50 km^2). Whenever snow would be permanent at such critical elevations, ice ablation therein would decrease, so possibly contributing to Karakoram anomaly.

At lower altitudes, where snow is seldom present, and where ablation takes place (meaning more vulnerable conditions for glaciers), CKNP ice bodies are mostly covered by a thick layer of debris. In particular, supraglacial debris covers 31 % of the total ablation area, and its maximum coverage is found at an altitude of 4300 m a.s.l. (below the estimated snowline). This may have played an important role in ice preservation during Summer, as a thick debris layer may slow down melting

rates (*Mihalcea et al., 2006*; *Hagg et al., 2008; Bocchiola et al. 2010*; *Mayer et al., 2010*; *Sherler et al., 2011),* as found out for several areas worldwide (*Mattson et al., 1993*).
These factors altogether may have pushed CKNP glacier mass balances towards positive net values. When focusing upon single glacier entities however, some variety is found. In facts, an in depth analysis revealed the presence of some potentially surge type glaciers in the study area. Surging may be statistically connected to various size-related variables, including perimeter and shape. Perimeter may increase the availability of avalanche-fed snow and debris material that may in turn affect the incidence of surging events (*Barrand and Murray, 2006*). In our case, those big glaciers representing most of the total icy coverage have complex shape (*i.e.* they are far from their equivalent circled shape), because of the many tributaries and the complex terrain. Areal changes here can then be caused not only by glacier expansion, but also by sudden advances, which most of the times do not translate into mass increase.
The stable superficial conditions we have found in CKNP glaciers agree, among others, with the results *Gardelle et al. (2012; 2013),* who found out a slight mass gain for glaciers in the same area for the same period.

1.5 Assessing glacier volume and thickness in the CKNP area

Furthermore, for assessing the recent evolution of water resources deriving from the CKNP glaciers, an indirect approach was applied. According to the method introduced by *Haeberli and Hoelzle (1995)*, ice thickness and volume data were estimated from ice shear stress values obtained by considering glacier geometry data recorded in the inventory (2001 data base).
The method was also applied by *Baumann and Winkler (2010)* for the analysis of glaciers in the New Zealand Alps and in Norway thus suggesting a wide applicability. Moreover *Hoelzle et al (2003)* applied such method to estimate changes and evolution of glaciers worldwide thus supporting the use of this parameterization for CKNP glaciers. The geometry data needed in the *Haeberli and Hoelzle (1995)* analytical approach are the glacier altitudinal range (i.e.: DH = glacier maximum elevation - glacier minimum elevation), the glacier maximum length (measured along the main flow line) and the area. Average ice depth along the central flow line was estimated from average surface slope (derived from the ratio of altitude range and glacier maximum length) and a mean basal shear stress along the central flow line (t_f = frg$h_f$sina, with f= shape factor chosen 0.8 for simplicity in all cases, r = ice density g= acceleration due to gravity, a= average surface slope), whereby t_f depends in a nonlinear way on the altitudinal range as a function of mass turnover (cf. *Driedger and Kennard, 1986*; *Haeberli, 1985*; *Haeberli and Hoelzle, 1995; Hoelzle et al; 2003*). See Table 1.3 for the applied parameterizations.
The input data are glacier length, area and elevation from 2001 CKNP Glacier Inventory. For this approach we considered 711 glaciers.

From our calculation we obtained a total ice volume of 666.38 km^3 over a glacier surface of 4606,061 km^2 thus giving a mean ice thickness of about 145 m. The maximum ice thickness value was found at the Biafo Glacier (1361 m) and deep ice thicknesses were also found at the Virjerab (1028 m), Baltoro (1016 m), Braldu (984 m) and Hispar (906 m) glaciers. The mean ice thickness over the whole glacier was found ranging from more than 200 m (285, 215, 213, 206 and 190 m at Biafo, Virjerab, Baltoro, Braldu and Hispar respectively) to less than 5 m at very small glaciers (i.e: with a surface area smaller than 0.1 km^2). The unique possible comparison is with Baltoro data which were acquired in 1954 during the well known expedition led by A. Desio, during which a glacier depth of about 900 m was derived from gravimetric surveys (*Desio, 1964*).

Table 1.3: Applied parameterizations

Name	Term	Calculation	Unit
Surface area	F	–	km^2
Length	L_0	–	km
Minimum altitude	H_{min}	–	m a.s.l.
Maximum altitude	H_{max}	–	m a.s.l.
Length change	δL	$L_{0,old}-L_{0,new}$	m
Mean altitude	H_{mean}	$(H_{max}+H_{min})/2$	m a.s.l.
Range	ΔH	$H_{max}-H_{min}$	m
Length of the central flowline in ablation area	L_a	$0.5*L_0$ if $L_0 \leq 2$ km; $0.75*L_0$ if $L_0 > 2$ km	km
Average surface slope	α	$\arctan(\Delta H/L_0)$	rad
Average surface slope in ablation area	α_a	$\arctan[(H_{mean}-H_{min})/L_a]$	rad
Mean basal shear-stress	τ	$0.005+1.598*\Delta H-0.435*(\Delta H)^2$ if $\Delta H \leq 1.6$; 1.5 if $\Delta H > 1.6$	bar
Average ice thickness at central flowline	h_f	$\tau/(f*\varrho*g*\sin\alpha)$	m
Average ice thickness at central flowline in ablation area	$h_{f,a}$	$\tau/(f*\varrho*g*\sin\alpha_a)$	m
Average ice thickness over whole glacier	h_F	$(\pi/4)*h_f$	m
Total glacier volume	V	$F*h_F$	km^3
Maximum ice thickness	h_{max}	$2.5*h_{f,a}$	m

1.6 Analysing energy fluxes and albedo variability at the Changri Nup Glacier surface (Nepal) and its relation to black carbon and dust deposition

The micro-meteorology and the energy fluxes at the surface of the accumulation area of the Changri Nup Glacier (through the analysis of data collected by the SHARE AWS installed at the glacier surface which has been running since February 2010) were characterized.
The glacier surface energy budget was calculated, as well as glacier melt over two ablation seasons. The results were crosschecked against ablation data collected on the field in 2011 and 2012.
Glacier albedo variability was described, along with its relation with dust and black carbon (BC) deposition and the BC influence on glacier melting rates.

In order to better understand the impact of BC on the albedo characteristics, the data have been correlated calculating their respective weekly moving average (Fig. 1.16). This has allowed to better highlight the correlation between the high values of BC concentration measured during the pre-monsoon season (April 2010) in the Changri Nup Humalayan area (NCO-P) and the consequent dramatic reduction of albedo values measured on the Glacier from late pre-monsoon season up to monsoon season.

To understand the influence of BC deposition in snow on the albedo reduction, the amount of BC deposition had to be calculated from the knowledge of the BC concentration in the atmosphere.

Therefore, total BC mass deposition flux per 30 minutes (1800 seconds) was calculated using assumption by *Yasunari et al., 2010:*

$$BC\ deposition = [atmospheric\ BC] \times (the\ minimal\ deposition\ velocity\ of 1.0 \times 10^{-4}\ ms^{-1}) \times (interval\ time = 1800\ s)$$

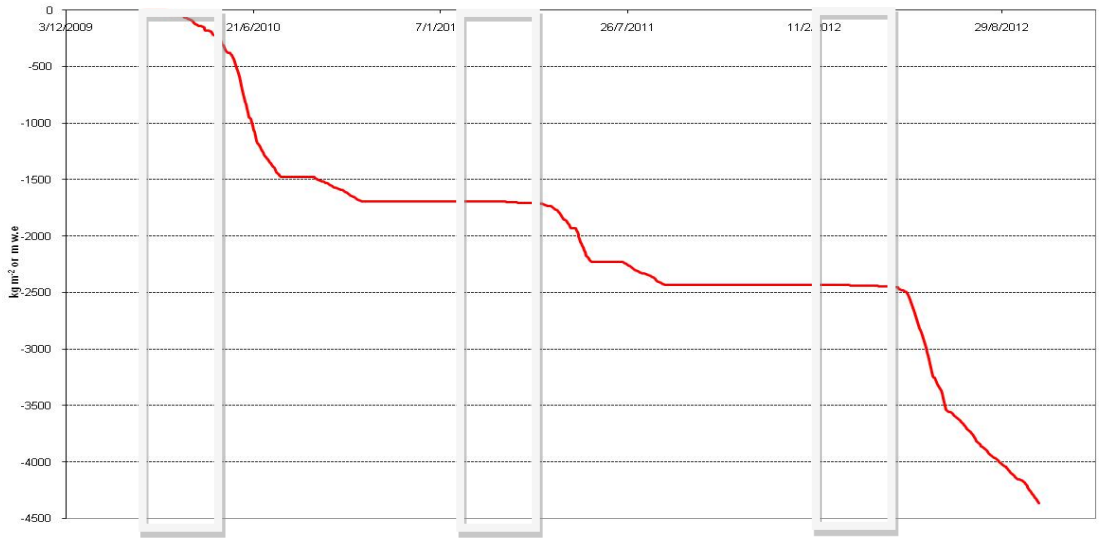

Figure 1.13: Cumulative daily melt at Changri Nup AWS in the period 2010-2012. Ice ablation is highlighted in grey.

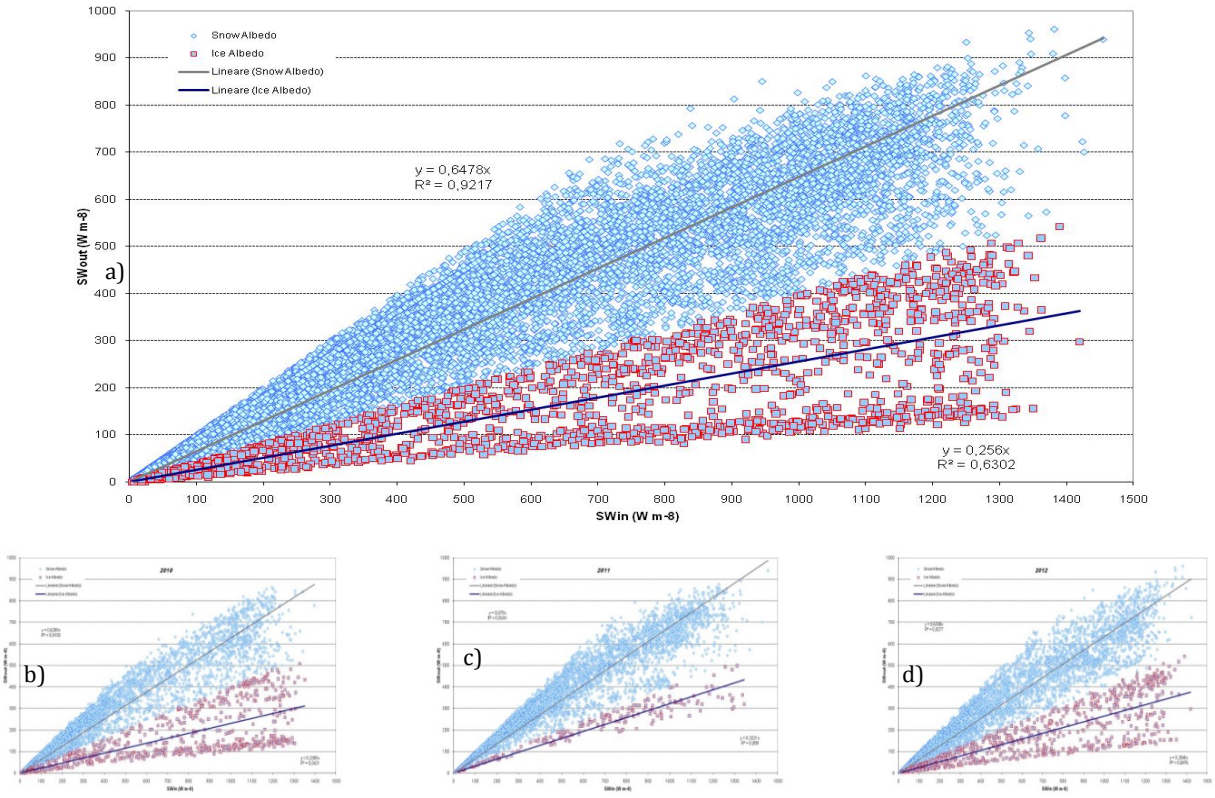

Figure 1.14: Daily albedo values characterizing exposed ice and snow covered surface in the period 2010-2012 (a) and per year (b, c, d)

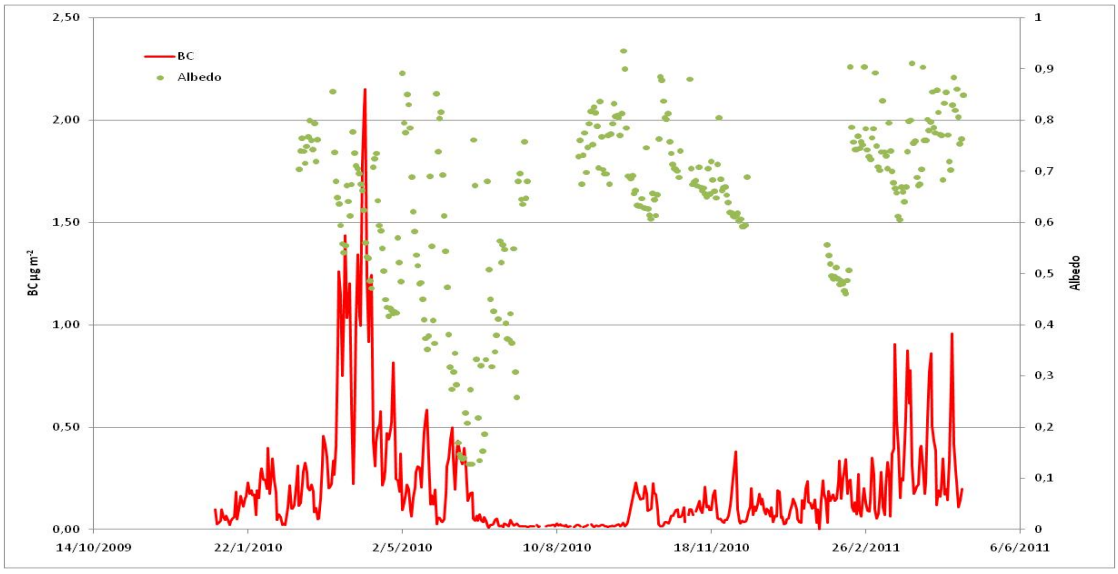

Figure 1.15: Daily mean albedo values measured at Changri Nup AWS and daily mean atmospheric BC (Black Carbon) concentration measured at NCO-P station in the period 2010-2012.

In this way, summating the BC flux for March–June 2010, a total deposition amount of BC equal to 394µg m^{-3} was derived.

Usually, the 2-cm top layer (5-cm top layer in *Aoki et al., 2000*) of snow on the glacier surface is more contaminated than the deeper part because snow impurities are derived from dry depositions of atmospheric aerosols (*Aoki et al., 2000, 2007; Tanikawa et al., 2009*). In addition, *Tanikawa et al. (2009)* showed that the mass concentrations of snow impurities deposited in the 2 cm-thick surface layer were about 30–50 ppmw (part per million by weight) whereas the concentrations within the first 2–10 cm were about 2–6 ppmw. Theses differences between the surface snow layer and the deeper snow layer impurities were consistent for elemental carbon, organic carbon, and dust in the study by *Tanikawa et al. (2009).* This indicates that the impurity concentration at the top 2-cm is much higher than that below, and the top snow layer is considered to play the key role in the albedo reduction process (*Yasunari et al., 2010*).

For this reason, assuming that the total BC amount of 394 µg m^{-3} is deposited on the 2 cm-thick surface layer of pure snow, without pre-existing contaminations from either BC or other particles such as dust, BC concentration in snow surface at Changri Nup, considering a measured snow density of 400 kgm−3, has been calculated as:

[BC concentration in snow] = BC dep / snow depth / snow density

Calculated amount of BC concentration in snow has been: 49 µg kg^{-1}, consistent with the concentration range of BCC in snow of 26.0–68.2 µg kg^{-1} due to snow density variations between 195–512 kg m^{-3} as reported in *Yasunari et al., 2010.*

The percentage of the albedo reduction correspondent to the peak of atmospheric BC concentration deposited and measured at ChangrI Nup has been determined as:

(Min Albedo after [atmosph. Max BC] – natural snow albedo) / natural snow albedo

that gave rise to the value 4.29.

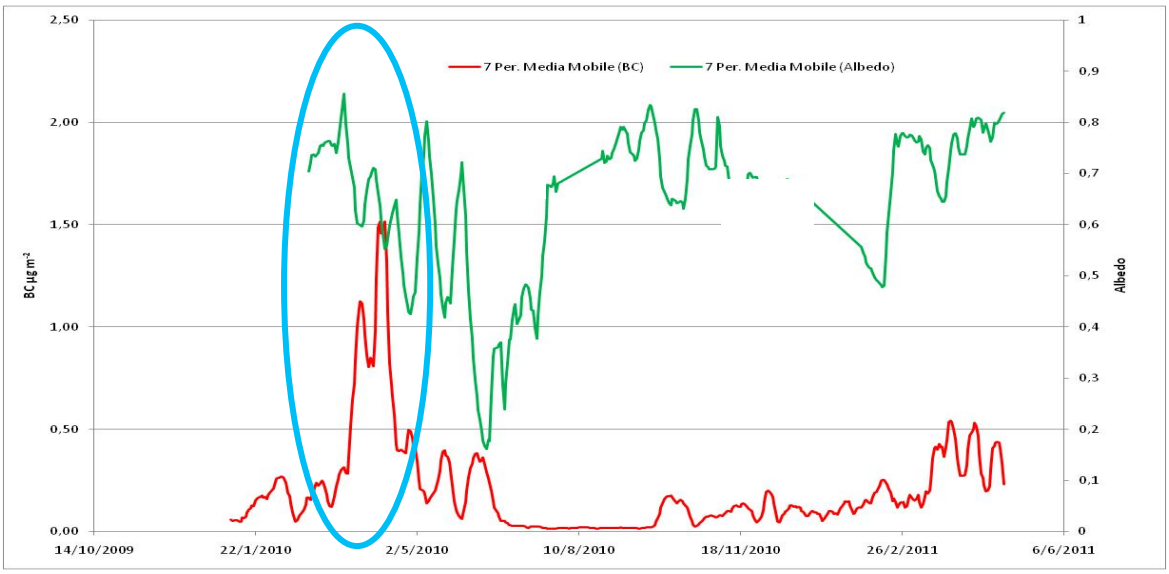

Figure 1.16: Moving average (7 Per.) of daily mean albedo values measured at Changri Nup AWS and daily mean atmospheric BC concentration measured at NCO-P station in the period 2010-2012.

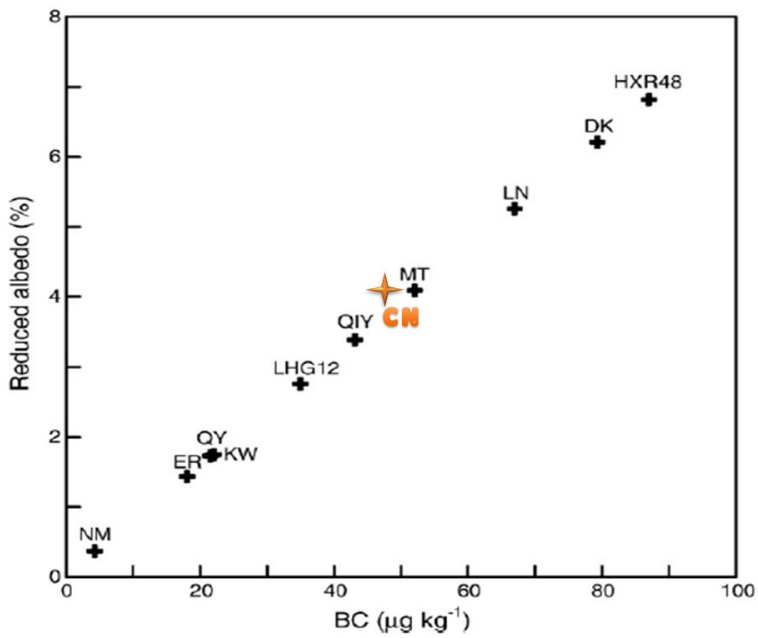

Figure 1.17: Albedo reduction vs BC concentration in snow (*Ming et al., 2009* modified). Orange indicator is related to ChangriNup glacier data.

In order to find a link between the estimated BCC in snow and the measured snow albedo reduction at Changri Nup, the obtained results have been compared with the correlation equation calculated by *Ming at al. (2009)* from available field and modeling data of BC concentration and % of albedo reduction on different worldwide glaciers. As reported in figure 1.17, the percentage of albedo

reduction measured at Changri Nup related to BCC in snow estimated from atmospheric [BC] measured at NCO-P station are well correlated.

In order to better verify the percentage of albedo reduction measured at Changri Nup with theoretical estimation of albedo reduction by *Ming et al., 2009,* the correlation equation:

$$y = 0.0757x + 0.575$$

has been applied considering as x value the BCC in snow estimated at Changri Nup glacier. The percentage of albedo reduction turbed out to be 4.23, very close to the value measured at Changri Nup, as reported in Table 1.4 .

Table 1.4: Estimated BCC in snow and % of albedo reduction deriving from Ming equation and measured at Changri Nup AWS.

BC deposition in snow (µg kg^{-1})	% Albedo reduction (from ChangriNup measurement)	% Albedo reduction (Calculated from Ming equation)
49	4.29	4.30

1.7 Changri Nup seasonal meltwater amount

Moreover melting values obtained from the Changri AWS data were also applied to evaluate the whole meltwater production at the Changri Nup debris free glacier. This evaluation was performed also with the aim of obtaining data to be compared with the glacier runoff amount measured by an automatic hydrometer installed at the debris free snout of the Changri Nup Glacier..

The NASA DEM RSTM (Radar Shuttle Topography Mission) surveyed in 2001, with a resolution of 90 x 90 m, available for free at the NASA site, was downloaded, useful to analyse glacier melting in the Changri Nup area. Recent satellite imagines (SPOT and Landsat) (Fig. 1.18) were also analysed to define the Changri Nup glacier debris free area, which turned out to about 0,99 km^2 wide. By coupling DEM and glacier boundary data the glacier surface area distribution was calculated, a fundamental input data to distribute glacier melt.

The glacier melt was distributed following a simple approach. We started from melt amount calculated in 2010, 2011 and 2012 from an automatic weather station data at 5700 m asl.

We applied a vertical ablation rate of 0.007 m w.e./m of elevation (see also *Oerlemans, 2001*). It means that ablation increases of 0.007m w.e. per an elevation decrease of 1 m. Then glacier zones located upper the AWS result with an ablation minor than the one we calculated at the AWS and glacier areas located lower the AWS have an ablation stronger. The glacier debris free area features an elevation range between 5358 m asl and 5791 m asl.

We divided the glacier area into 293 glacier belts and by a GIS software we evaluated their surface coverage. By applying the vertical melt rate we evaluated for each elevation belt the glacier melt and considering elevation belt area we computed the derived volume of meltwater. The total

volume variation resulted to be -2,61 x $10^6 m^3$w.e. in 2010 corresponding to -2.62 m of mean thickness variation. In 2011 the volume variation resulted to be-2,095 x $10^6 m^3$w.e. corresponding to -2.02 mw.e. of mean thickness variation and in 2012 the volume change resulted -2,73 x $10^6 m^3$ w.e. corresponding to -2.74 mw.e. of thickness variation.

Figure 1.18: Changri Nup glacier area estimated by analyzing SPOT Imagines.

Moreover through this simple modelling approach we also evaluated ELA (Equilibrium Line Altitude) of the Changri Nup Glacier. When melt amounts evaluated by applying the vertical gradient results equal to zero it means that ELA has been reached. It has been estimated at 6,000 masl in 2010 and 2012 as highlighted from the previous results showing a similarity in there two years, while in 2011 ELA was estimated at 5,850 m asl.

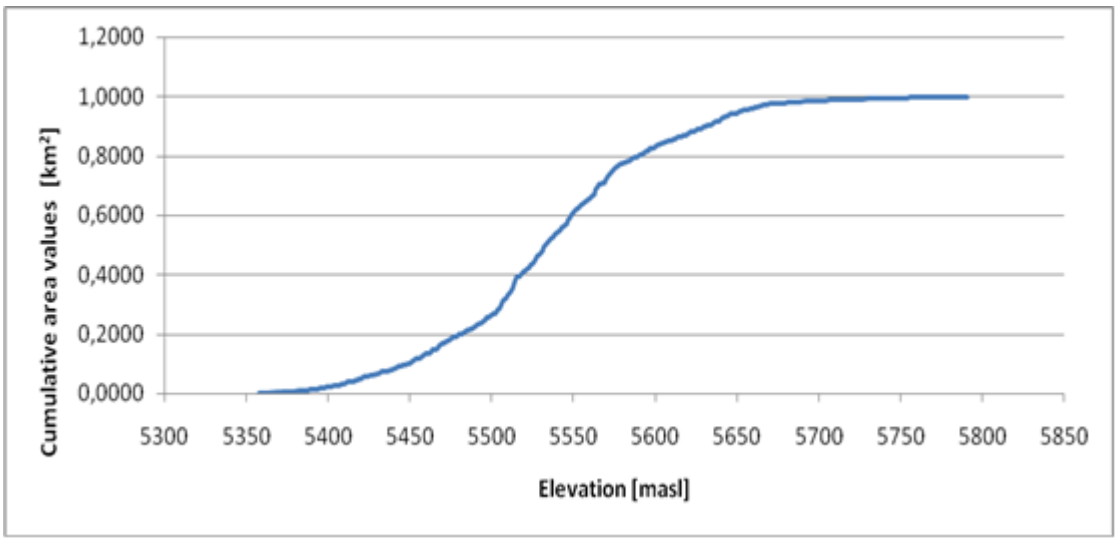

Figure 1.19: The surface area distribution of the ChangriNup glacier evaluated by coupling glacier boundary from SPOT with glacier DEM from SRTM NASA.

1.8. Radar surveys

Radar exploration supports glaciological studies since it allows for the determination of the ice thickness and volume, description of ice and snow internal layering and characterization of crevassed areas. The method has been successfully applied on regional glaciers (e.g., in the Polar zones), while, to date, it has encountered more difficulties for surveying smaller-scale (local) glaciers, like the Alpine and Himalayan ones. This is mainly due to three reasons: 1) the different physical characteristics of ice in the temperate climatic regions; 2) the lack of instruments specifically devised to investigate this kind of ice; and 3) logistic obstacles, related to the difficulty of performing field campaigns in high-elevated areas where crevasses and ice falls might occur.
In the framework of the SHARE-PAPRIKA project a series of tests was performed on Alpine glaciers to evaluate efficiency and applicability of an airborne Radio Echo Sounding (RES) instrument designed and developed at the INGV (Istituto Nazionale di Geofisica e Vulcanologia) laboratories, to be then used over the Karakoram-Himalayas.
The original idea was to create a system devised to work on local mountain glaciers such as the Himalayan ones, that is, high-elevations, deep (more than 1000 m) glaciers, characterized by steep mountain walls and reduced glacier width (with respect to the glacier length), and such that the commercial GPR instruments cannot be used. For several glaciers in the central Karakoram, supraglacial debris coverage is present which, together with the occurrence of ice seals and pinnacles, increase the logistic difficulties in transporting the radar and antenna systems along the glaciers surface (see *Mayer et al., 2006; Mihalcea et al., 2008*).
We performed the preliminary radar tests on July 2012 on three different Alpine glaciers located in the central Italian Alps: Careser Glacier, Sforzellina Glacier and Forni Glacier, with the main goals of:

1) verify the RES system reliability;
2) assess the effectiveness of a power pulse to ice opacity phenomena;
3) evaluate the effectiveness of airborne measurements;
4) collect information on ice thickness and bedrock assessment on the investigated glaciers.

We were able to collect 100% of high quality data on glaciers featuring the smallest dynamics, that is, the Careser (Fig. 1.21) and Sforzellina (Fig. 1.22) glaciers while we got about the 65% of information for the Forni glacier (Fig. 1.23). It is interesting to observe that the presence of thick supraglacial debris coverage did not affect the effective bedrock reflections, which is important since most Karakoram glaciers are debris-covered (e.g., Mayer et al., 2006; Mihalcea et al., 2008). Unfortunately, the expedition initially planned on October 2013 on the Baltoro was not carried out due to unexpected logistic difficulties in aviation support.

Figure 1.20 RES instrument mounted inside the helicopter and antenna support

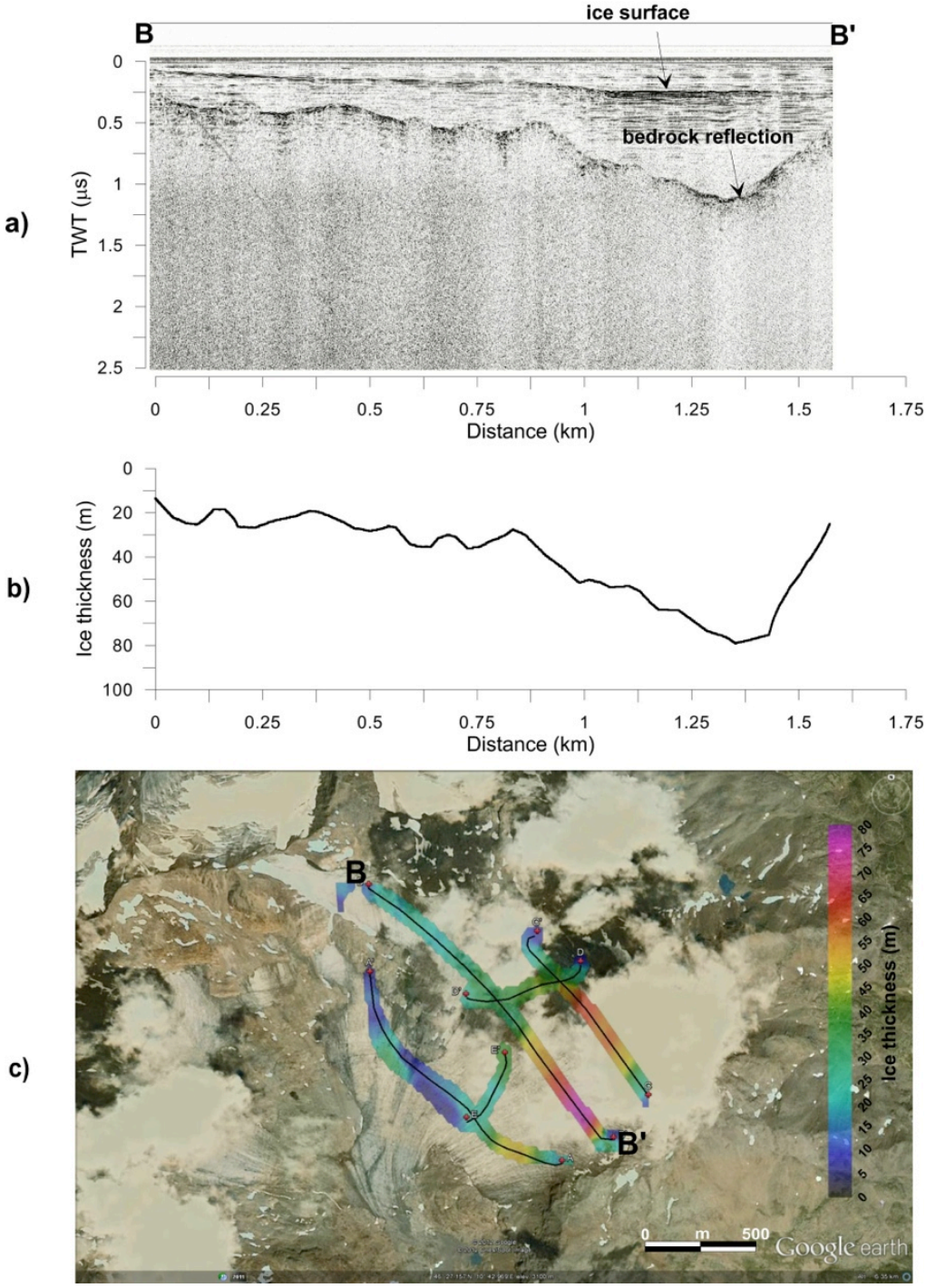

Figure 1.21. Radargrams and interpretation on Careser Glacier (central Italian Alps)

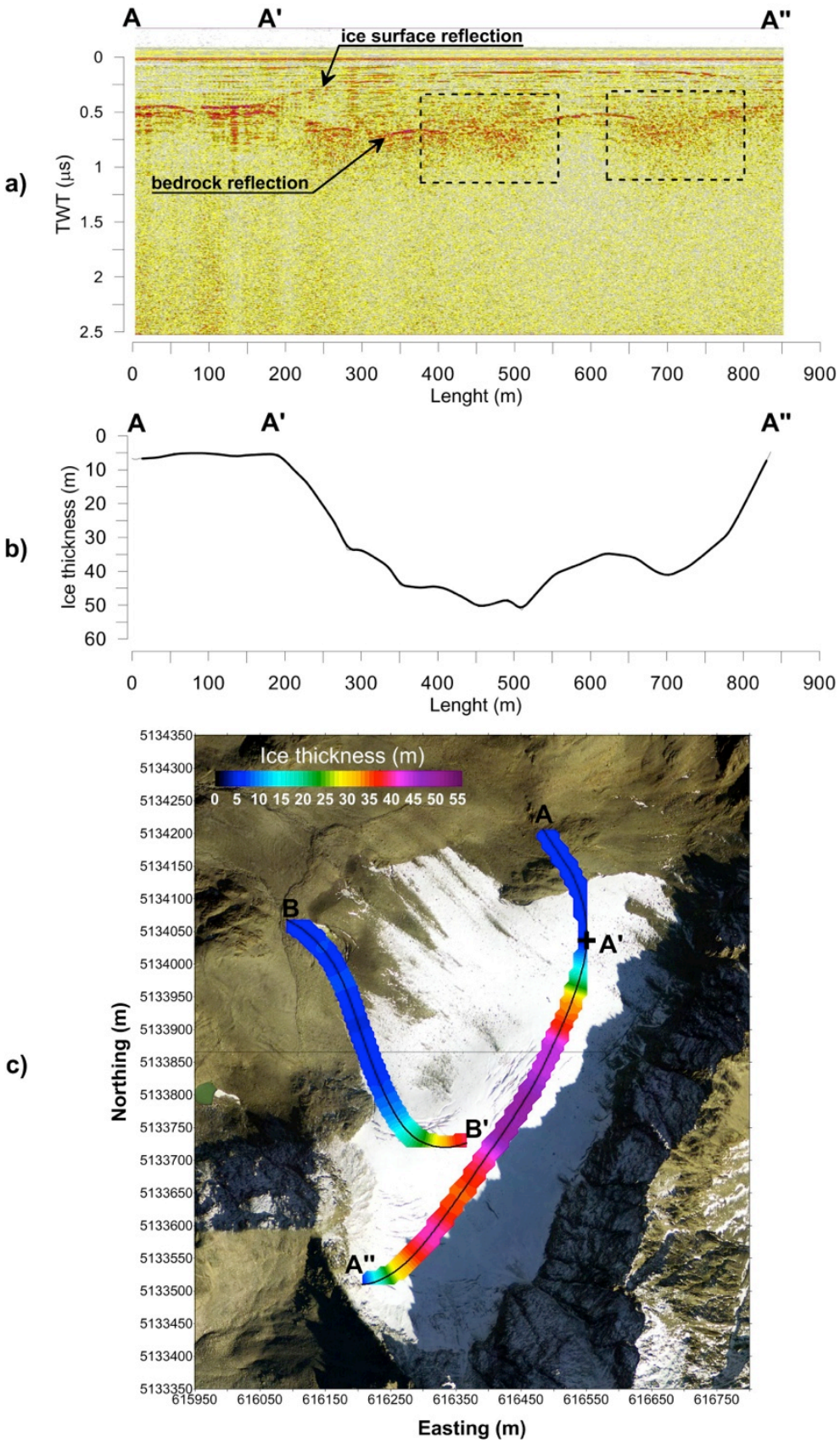

Figure 1.22. Radargrams and interpretation on Sforzellina Glacier (central Italian Alps)

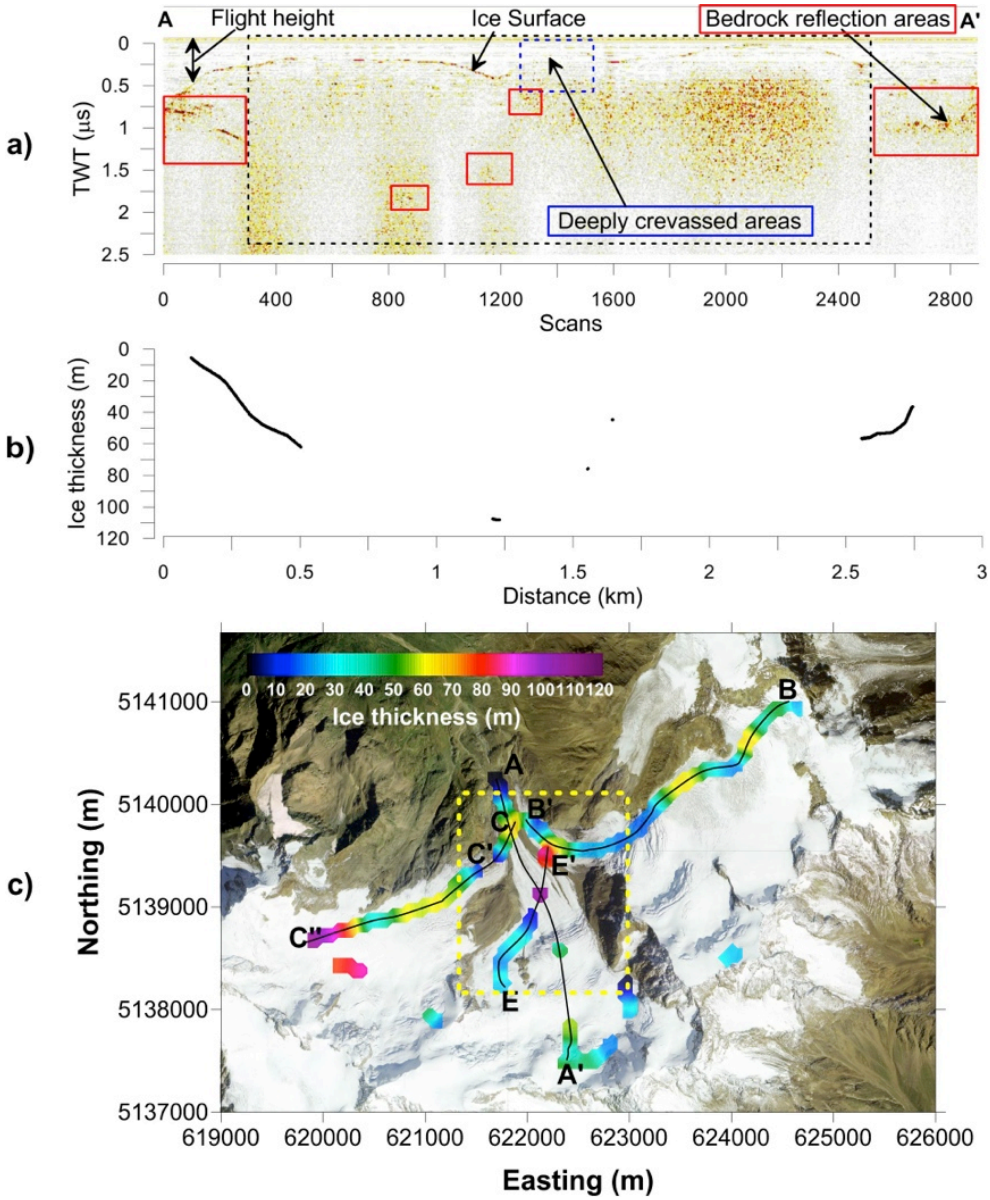

Figure 1.23. Radargrams and interpretation on Forni Glacier (central Italian Alps)

References

AR5 2013: Intergovernmental Panel on Climate Change (IPCC): Working Group I Contribution to the IPCC Fifth Assessment Report, Climate Change 2013: The Physical Science Basis, Approved Summary for Policymakers, September 27, 2013.

Aoki, T., T. Aoki, M. Fukabori, A. Hachikubo, Y.Tachibana and F. Nishio. (2000). Effects of snow physical parameters on spectral albedo and bidirectional reflectance of snow surface. Journal of Geophysical Research , vol. 105, no. D8, 10219-10236

Aoki, T., H. Motoyoshi, Y. Kodama, T.J. Yasunari and K. Sugiura. (2007). Variations of the snow physical parameters and their effects on albedo in Sapporo, Japan. Annals og Glaciology, 46, n. 1, 375-381

Barrand, N. and Murray, T.: Multivariate controls on the incidence of glacier surging in the Karakoram Himalaya, Arct. Antarct. Alp. Res., 38, 489-498, 2006.

Baumann S and Winkler S (2010) – Parameterization of glacier inventory data from Jotunheimen /Norway in comparison to the European Alps and the Southern Alps of New Zealand. Erdkunde, vol 64 (2), 155-177.

Bocchiola, D., Mihalcea, C., Diolaiuti, G., Mosconi, B., Smiraglia, C., and Rosso, R.: Flow prediction in high altitude ungauged catchments: a case study in the Italian Alps (Pantano Basin, Adamello Group), Adv. Water Resources, 33(10), 1224-1234, 2010.

Desio, A.: Italian Expeditions to the Karakorum (K2) and Hindu Kush, in: Leader II, vol. 1, edited by: Marussi, A., E. J. Brill, Leiden, 1964.

Driedger, C.L., Kennard, P.M., 1986. Glacier volume estimation on Cascade Volcanoes: an analysis and comparison with other methods. Annals of Glaciology, 8, 59-64.

Gardelle, J., Berthier, E., and Arnaud, Y.: Slight mass gain of Karakoram glaciers in the early 10 twenty-first century, Nat. Geosci. Letters, 5, 322-325, doi:10.1038/NGEO1450, 2012.

Gardelle, J., Berthier, E., Arnaud, Y., and K¨a¨ab, A.: Region-wide glacier mass balances over the Pamir-Karakoram-Himalaya during 1999-2011, The Cryosphere Discuss., 7, 975-1028, doi:10.5194/tcd-7-975-2013, 2013.

Hagg, W., Mayer, C., Lambrecht, A., and Helm, A.: Sub-debris melt rates on Southern Inylchek glacier, Central Tian Shan. Geogr. Ann. 90A (1): 55-63, 2008.

Haeberli W., 1985. Global land-ice monitoring: present status and future perspectives. United States Department of Energy, Glaciers, Ice sheets and Sea level: Effect of a CO2 – Induced Climate Change. Report DOE/EV 60235-I. National Academy Press, Seattle, WA, pp. 216-231.

Haeberli, W. and Hoelzle, M., 1995: Application of inventory data for estimating characteristics of and regional climate-change effects on mountain glaciers: a pilot study with the European Alps. Annals of Glaciology., 21: 206-212.

Hoelzle, M., Haeberli, H., Dischl, M. and Peschke, W., 2003: Secular glacier mass balances derived from cumulative glacier length changes. Global Planetary Change, 36: 295-306.

Mattson, L. E., Gardner, J. S., and Young, G. J.: Ablation on debris covered glaciers: an example from the Rakhiot Glacier, Punjab, Himalaya, in: Snow and Glacier Hydrology, Proc. Kathmandu Symp., November 1992, edited by: Young, G. J., IAHS Publ. no. 218, IAHS Publishing, Wallingford, 289-296, 1993.

Mayer, C., Lambrecht, A., Mihalcea, C., Belò, M., Diolaiuti, G., Smiraglia, C., Bashir, F., Analysis of Glacial Meltwater in Bagrot Valley, Karakoram, Mountain Research and Development, 30(2), 169-177, 2010.

Mihalcea, C., Mayer, C., Diolaiuti, G., Lambrecht, A., Smiraglia, C., and Tartari, G.: Ice ablation and meteorological conditions on the debris covered area of Baltoro Glacier (Karakoram, Pakistan), Ann. Glaciol., 43, 292-300, 2006.

Ming J., C. Xiao, H. Cahier, D, Qin, X. Qin, Z. Li, J. Pu (2009). Black Carbon (BC) in the snow of glaciers in west China and its potential effects on albedos. Atmospheric Research 92, 114–123

Oerlemans, J., (2001). Glaciers and Climate Change. Lisse: Balkema, 115 pp.

Sherler, D., Bookhagen, B., and Srecker, Manfred, R.: Spatially variable response of Himalayan glaciers to climate change affected by debris cover, Nature Geoscience, Vol. 4, doi: 10.1038/NGEO1068, 2011.

Tahir, A. A., Chevallier, P., Arnaud, Y., and Ahmad, B.: Snow cover dynamics and hydrological regime of the Hunza River basin, Karakoram Range, Northern Pakistan, Hydrol. Earth Syst. Sci., 15, 2275-2290, doi:10.5194/hess-15-2275-2011, 2011.

Tanikawa, T., Stamnes, K., Aoki, T., Kuchiki, K., Hachikubo, A., and Sugiura, K.: Effect of snow impurities and vertical profile on snow albedo and reflectance, Eos Trans. AGU, 90(52), Fall Meet. Suppl., Abstract C33C-0519, 2009.

Yasunari, T.J., P. Bonasoni, P. Laj, K. Fujita, E. Vuillermoz, A. Marinoni, P. Cristofanelli, R. Duchi, G. Tartari & K.M. Lau. (2010). Estimated impact of black carbon deposition during pre-monsoon season from Nepal Climate Observatory-Pyramid data and snow albedo changes over Himalayan glaciers. In: Special Issue "Atmospheric brown cloud in the Himalayas" Atmospheric Chemistry and Physics, 10: 6603-6615.

WP2: Hydrological observations

D.Bocchiola, A. Soncini, G. Confortola, E. Nana, A. Bianchi, R. Rosso (POLIMI)

A. Lami, M. Rogora (ISE-CNR)

2.1. Hydrological characteristics and water quantity

2.1.1 Introduction

During the PAPRIKA project, the POLIMI team has carried out four field missions aimed at measuring the quantity of water that originates from glaciers and starting a continuous discharge monitoring through the installation of two hydrometric stations. These activities have also provided important data for model evaluation and validation purposes.

2.1.2 Field campaigns summary

The four missions were carried out in spring and summer, particularly on April and July, 2011, May 2012 and April 2013 (Table 2.1).

Table 2.1. Activities performed during the field missions

Site	Survey details
Shigar bridge	- Topographic survey of the river section, float and stopwatch velocity measurements, flow velocity measurements using 3-d Doppler flow tracker. - Hydrometric station installation and maintenance. - Stage-discharge curve estimation. - Water sample collection.
Dasso	Water sample collection.
Askole	Water sample collection.
Biafo River	- Discharge measurements using salt tracer method. - Water sample collection.
Korophon	- Topographic survey of the river section, float and stopwatch velocity measurements, flow velocity measurements using 3-d Doppler flow tracker. - Discharge measurements using salt tracer method. - Water sample collection.
Jula River	- Discharge measurements using salt tracer method. - Water sample collection.
Bardumal	- Discharge measurements using salt tracer method. - Water sample collection.
Paiju	- Topographic survey of the river section, float and stopwatch velocity measurements, flow velocity measurements using 3-d Doppler flow tracker. - Hydrometric station installation and maintenance. - Stage-discharge curve estimation. - Water sample collection (from the river and from the campsite water supply)
Golabital	- Discharge measurements using salt tracer method. - Water sample collection.
Liligo	Water sample collection.
Koburtze	Water sample collection.
Urdukas	Water sample collection.

Discharge measurements and topographic survey

To measure stream flows in natural or artificial channels, several methods are available. A rough distinction of these methods can be made as follows:

- *Eulerian methods.* Flow is evaluated through the observation of some physical variables related to discharge (velocity, flow depth, pressure ...) in a fixed point, in particular the *direct velocity measurement* has been used. Flow discharge is derived from flow velocity and flow area (3-d Doppler flow tracker);

Area/velocity method provide the discharge by integration of the flow velocity over the flow area, and the flow velocity is usually measured in a number of small areas.The discharge is then estimated as the sum over the whole area.

- *Lagrangian methods.* A stem of the river is considered and the along-track change in physical variable (float, tracer, etc..) provides indication of flow discharge. In detail we used NaCl as tracer. In sites with excessive turbulence, high velocity and depth, where wading or using whirl would be complicate/dangerous, tracers can be used alone, and calibration of stage discharge curve can be done by coupling flow measurements (as many as possible) with water depth measurements. Otherwise, if section geometry can be measured but velocity cannot be estimated using a flow meter, the tracer method provide a discharge estimation that can be used to calibrate Manning's equation. Given the initial quantity of salt injected and measuring the salt concentration in the river it is possible to estimate the quantity of water where salt is diluted. Since the tracer must be homogeneous within the flow, injection must occur several meters upstream of the flow measuring section.

The spot measurements made during the field missions are essential for the stage-discharge curve estimation (relation to evaluate discharge from measured water level). In addition to discharge measurements it is necessary to know the geometry of the river cross section, for this reason we carried out a high precision topographic survey of the river in correspondence of the hydrometric stations (Shigar and Paiju). During these surveys we marked some points so that in the future we will update the geometry survey monitoring the river bed variations due to erosion/sedimentation phenomena to properly adjust the stage-discharge relation.

Employed devices:

- Topcon station for topographic surveys (tripod, stake, and spot);
- GPS navigator for site referencing;
- Conducimeter for NaCl flow measurements;
- Eco-sounder for flow depth;
- Digital camera for post-processing and float-stop watch velocity assessment;
- Notebook for data handling.
- Flow tracker, Doppler velocimeter 3-D.

Hydrometric stations and stage-discharge curve estimation

During the first and third field missions, in 2011 and 2012, respectively, we installed two hydrometric stations at Shigar bridge and at Paiju to collect water level data continuously (Figs. 2.1-2.4). These stations measure the water level every 15 minutes and they are essential to calibrate and validate the hydrological model we implemented and used in PAPRIKA (see chapter on WP4 activities). The technical characteristics of the Shigar and Paiju stations are reported in Table 2.2.

For the two stations we estimated the stage-discharge curve (updated every year) allowing for the calculation of the discharge value starting from the measured water level value (Fig. 2.5). If many observations corresponding to the different flow conditions are available it is possible to get the

stage-discharge curve by the interpolation of the data and calculating immediately the *a* and *m* value of the power law equation. If the observed data are not sufficient to validate the interpolated stage-discharge curve, different simulations are carried out with a hydraulic software, such as HEC-RAS (one-dimensional steady flow analysis) developed by the US Army Corps of Engineers - under steady flow hypothesis. The obtained values are then interpolated and compared to the available observed data

Figure 2.1: Shigar hydrometric station

Figure 2.2: Paiju hydrometric station

Figure 2.3:Installation of the Paiju hydrometric station

Figure 2.4: Topo & flow tracker surveys, Shigar (left) and Korophon (right)

Measured data

At the end of these three years of field work on the Shigar basin we have a good knowledge of the hydrological behaviour of this area. In particular we have 2 years of continuous discharge data at 15 minutes time resolution at Shigar bridge and, unfortunately, only one month in 2012 and the 2013 ablation season at the Paiju station. In Fig. 2.6 we report the measured series used for the calibration of the hydrological model for the whole the Shigar basin.

The Shigar station, installed in April 2011 and repaired in May 2012, is working perfectly apart from the solar panel that was found damaged and that has been replaced during the 2013 field mission. At present, a complete series of level measures from May 20th 2012 to July 13th 2013 is available and through the stage calibrated discharge curve it will be possible to estimate the discharge and the calibration of the hydrological model for the entire basin of the Shigar at the Shigar bridge.
In the Braldo valley we carried out, as described above, different spot flow measurements with the salt tracer method, in order to estimate quantitatively the flow of the river and the contribution of the main tributaries.
The station at Paiju bridge, seriously damaged by the high flow rate during the last summer, was repaired in April 2013 through the installation of two new piezometric sensors which were fixed to the rock. The location of this station is fundamental for the study of the outflows and the calibration of the sub-basin limited to the Baltoro glacier, as it excludes the contribution of other secondary tributaries.

Table 2.2: Technical specifications of the Shigar and Paiju hydrometric stations.

Shigar station technical specifications	
Altitude	2221 m a.s.l.
Watershed area	6923 km^2
Datalogger	Campbell Scientific - CR200X
Sensor	sonic sensor Vegason 63, 4-20 mA, 24V
Power supply	solar panel 20W + battery Pb 12V 40 Ah
Installation date	24 April 2011
Repair date	19 May 2012
Functioning period	24/04/11 - 27/05/11
	19/05/12 - today

Paiju station technical specifications	
Altitude	3356 m a.s.l.
Watershed area	1331 km^2
Datalogger	Campbell Scientific - CR200X
Sensor	piezometric STS atm.eco/n, 4-20 mA, 12V
Power supply	solar panel 20W + battery Pb 12V 16 Ah
Pipe	HDPE 1 ¼ “”
Installation date	23 May 2012
Functioning period	23/05/12 - 21/06/12
	23/04/13 - today

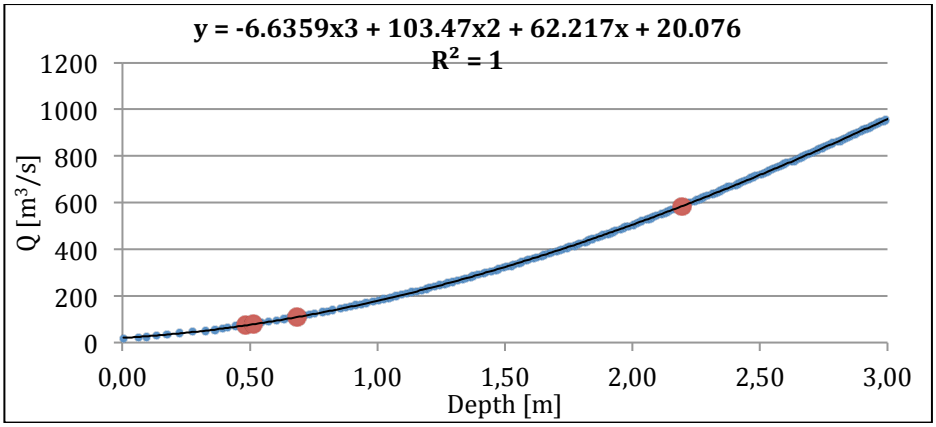

Figure 2.5: Estimated stage-discharge curve for the Shigar river section

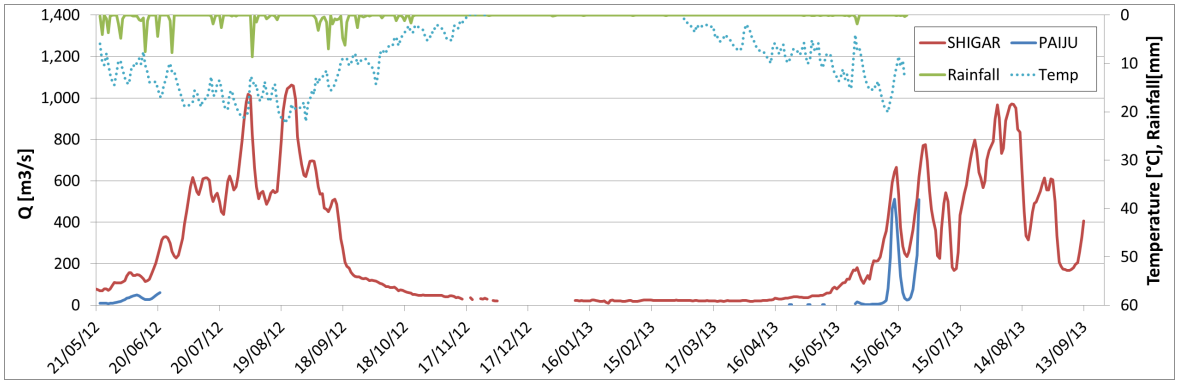

Figure 2.6: Discharge daily data for the two stations (temperature and rainfall are from Askole Ev-K2 CNR AWS)

2.2. Water quality

Lakes and streams in mountain or remote regions are sensitive to the effects of global and regional warming: ice and snow melting due to air temperature increase may lead to increase in soil microbial activity and in mineral weathering rates, causing enhanced nutrient and solute fluxes to mountain lakes and streams (*Lami et al., 2010; Baron et al., 2009; Rogora et al., 2003*). In regions suffering the impacts of long-distance transported pollutants, warming may also lead to an increase in nitrogen leaching and the release of toxic substances from rock and ice glaciers (*Thies et al., 2007; Williams et al., 2007*). The activities performed within WP 2.2 focused on chemical analysis of surface waters in order to assess their quality in relation to possible anthropogenic stressors such as long-range transboundary air pollution and climate change.
Water samplings were performed partly by researchers of CNR Institute of Ecosystem Study (CNR ISE) and partly by personnel of Politecnico di Milano (POLIMI) during four sampling campaigns (April and July-August 2011, May-June 2012, April 2013; Fig. 2.7). The main objectives of these campaigns were:

(1) to characterize the water chemistry in a number of sites in the Shigar watershed, located along geographical gradients;
(2) to assess spatial differences in water chemistry, in particular as regards ionic composition and nutrient concentrations;
(3) to assess temporal variations (seasonal and interannual) in the chemical composition of water at a few selected sites, subject to repeated sampling during the study period.

Figure 2.7. Sampling stations along the Shigar Valley (from left to righet: Jula river, Baltoro front, Khoburtze glacier).

In total 45 samples have been collected and analyzed for water chemistry at the laboratory of CNR ISE. Variables, analytical methods and QA/QC programs in use at the laboratory are described in details at http://www.idrolab.ise.cnr.it/.

According to the data collected in April, which are representative of base flow conditions, the study area is characterized by quite homogeneous water chemistry in terms of major ions. As an example, the ionic composition of a number of sites along a west to east (and altitudinal) gradient is shown in Fig. 2.8 (data of April 2013). The sites of Askole and Shigar Bridge are shown separately because of the higher ionic concentrations with respect to the other sites.
The dominant cation and anion are calcium and bicarbonate, respectively, representing together 60-75% of the total ionic content at most of the sites. The only exception is Askole, where sulfate is the dominant anion, and magnesium is as much important as calcium among cations. A different lithological composition probably characterizes the Askole area, with a prevalence of $CaSO_4$ and $MgSO_4$ in the mineral bedrock. Despite a similar ionic composition, the different sites show an increasing solute content from the highest (i.e. close to the Baltoro glacier) to the lowest sites: for instance conductivity increased form 90 µS cm^{-1} at the sampling site before Khoburtse to about 250 µS cm^{-1} at LomarSpang and Chukil. The lower ionic content of water at higher altitude is due to a dilution effect: a bigger amount of water is present in the upper part of the watershed in spring months, because of ice and snow melting.

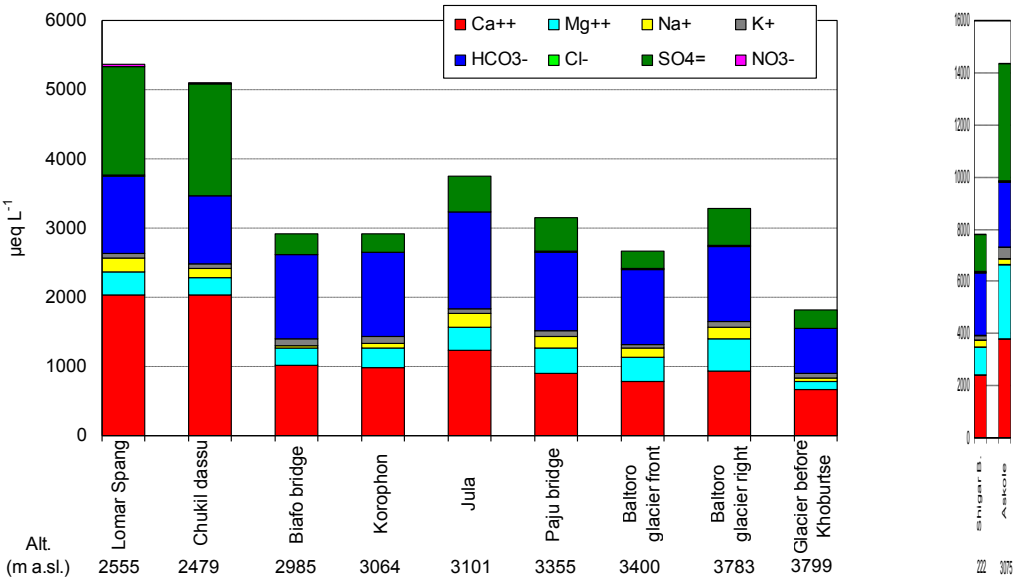

Figure 2.8: Ionic composition of water samples collected in April 2013. For each site the altitude in m a.s.l. is shown.

The concentrations of the various forms in nitrogen in water samples throughout the study period is shown in Fig. 2.9. Nitrate (NO_3) is the dominant form in nitrogen in surface waters at the study sites; only in a few cases organic nitrogen dominates, while ammonium (NH_4) is almost negligible. Both reactive and total phosphorus concentrations were low at the study sites (usually below 10 µg P L^{-1} as total P). Slightly higher concentrations (20-25 µg P L^{-1}) were measured at Shigar and at Korophon and Paju Bridge (only in 2013). Total nitrogen concentrations were mostly below 0.2 mg N L^{-1}; higher values (0.5-0.8 mg N L^{-1}) were found in 2012 at several sites, but they were due to a higher presence of organic N. TOC concentrations were also low (< 1.0 mg C L^{-1}). Results as a whole indicate a good quality of surface water in the study area, with low nutrient and organic substance levels. Only one episode of water contamination has been detected during the study period (at Urdukas in May 2012) buy it was not confirmed by repeated samplings, so that it can be ascribed to a temporary and spatially limited situation (e.g. a local contamination by sewage from the camp).

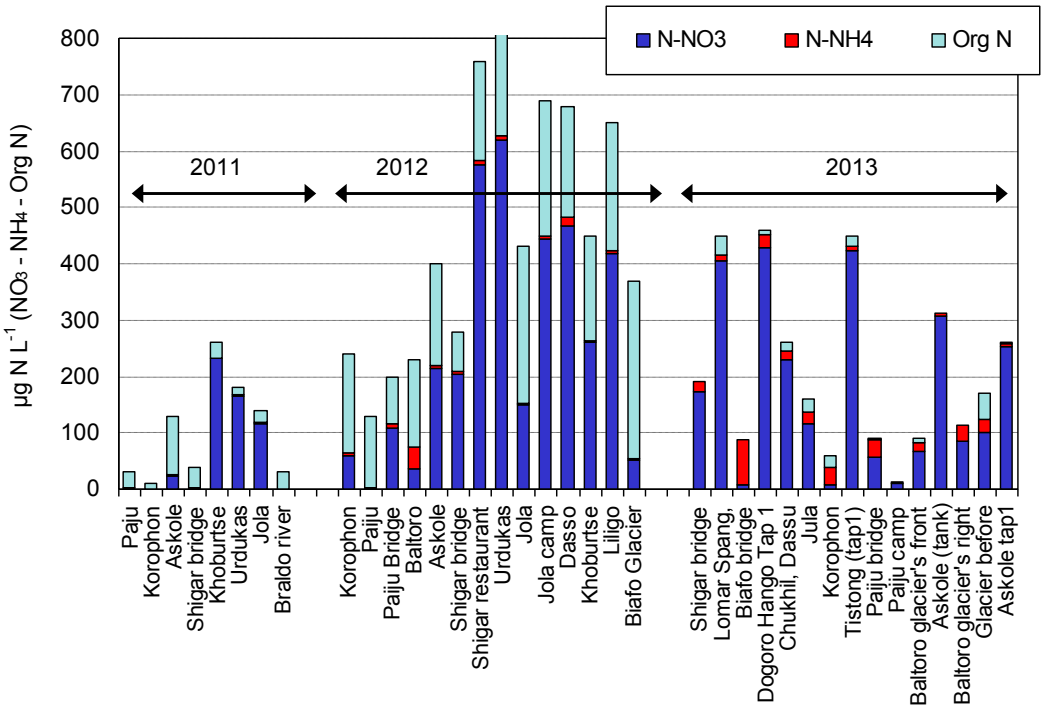

Figure 2.9: Concentrations of N compounds in the water samples collected during the three year period.

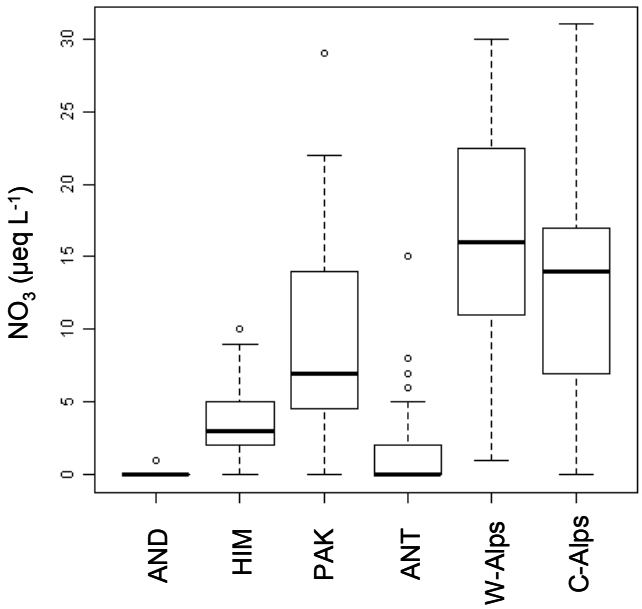

Figure 2.10: Comparison of NO_3 concentrations detected in water chemical surveys at different remote locations: AND: Andes (Argentinean Patagonia); HIM (Himalaya, Nepal); PAK (Pakistan, this study); ANT: Antarctica; W-Alps (Western Alps, Italy); C-Alps (Central Alps, Italy).

The good quality of water in the study area was also confirmed by the analysis of trace metals, performed on the samples collected in 2012: toxic metals such as Cu, Cr, Ni, Cd and Pb always showed very low concentrations, in most cases below the detection limit of the used method.

The presence of NO_3 in the water samples, even if at very low concentrations, may derive from atmospheric contribution. Indeed nitrate is usually absent in surface waters at remote location, where direct anthropogenic inputs can be excluded (*Rogora et al., 2003).* Nitrate concentrations were highly variable at the study sites, but they often reached 200-400 µg N L^{-1} (15-30 µeq L^{-1}).

These levels are normally found in lakes of the Western and Central Alps, in Italy, where atmospheric deposition of N compounds are quite high, due to the long-range transport from emission sources in the lowlands; furthermore they proved to be higher with respect to levels found in water samples in other remote areas (e.g. Himalaya, Antarctica, Andes) (Fig. 2.10).

A subset of 4 sites was subject to repeated samplings, to assess temporal variability in the water chemical composition. No relationships were found between chemical variables and meteorological drivers such as temperature and precipitation. On the other hand, the solute content proved to be mainly driven by hydrology: sampled collected in July 2011 and June 2012 were usually characterised by lower conductivity and ionic concentrations, due to a dilution effect. Water discharge measured at Shigar was indeed much higher in July, at the snowmelt (538 m^3 s^{-1} in July 2011) compared to April, in base flow conditions (5-7 m^3 s^{-1}). This result highlights the prominent role of hydrology and glacier melting dynamics in affecting water chemistry.

The results of water chemical surveys performed in the Shigar watershed over a three year period put in evidence the good quality of water in this area: trace metals and other inorganic contaminants were almost absent and only in a very few cases episodes of water contamination by local sources were found. Water chemistry proved to be mainly controlled by land cover (bedrock lithology) and hydrological factors (dilution/concentration processes in relation to the amount of water). A contribution of atmospheric deposition to the N content of water samples (mainly as NO_3) cannot be excluded. In the future it would be useful to investigate the atmospheric fluxes of nitrogen and other chemical compounds affecting this area.

References

Baron J.S., Schmidt T.M., Hartman M.D. 2009. Climate-induced changes in high elevation stream nitrate dynamics. Global Change Biology, 15, 1777–1789.

Lami, A., Marchetto A., Musazzi S., Salerno F., Tartari G., Guilizzoni P., Rogora M., Tartari G.A. 2010. Chemical and biological response of two small lakes in the Khumbu Valley, Himalayas (Nepal) to short term variability and climatic change as detected by long-term monitoring and paleolimnological methods. Hydrobiologia, 648: 189–205.

Rogora, M., Massaferro J., Marchetto A., Tartari G.A., Mosello R. 2008. The water chemistry of Northern Patagonian lakes and theirnitrogen status in comparison with remote lakes in different regions of the globe. J. Limnol. 67 (2): 75-86.

Rogora, M., R. Mosello& S. Arisci. 2003. The effect of climate warming on the hydrochemistry of alpine lakes. Water Air Soil Poll., 148: 347-361.

Thies H., Nickus U., Mair V., Tessadri R., Tait D., Thaler B., Psenner, R. 2007. Unexpected Response of High Alpine LakeWaters to Climate Warming. Environ. Sci. Technol., 41 (21): 7424–7429.

Williams M.W., Knauf M., Cory R., Caine N., Liu F. 2007. Nitrate Content and Potential Microbial Signature of Rock Glacier Outflow, ColoradoFront Range. Earth Surf. Process. Landforms 32, 1032–1047.

WP3: Atmospheric Observations

Paolo Cristofanelli, Paolo Bonasoni, Angela Marinoni, Davide Putero (ISAC-CNR)

Elisa Vuillermoz, Gian Pietro Verga (EV-K2-CNR)

3.1 Introduction

With the purpose of providing a first quantitative assessment of the current state of the atmospheric composition variability, atmospheric aerosol properties and their relationship with atmospheric circulation, two experimental campaigns have been carried out in the Baltoro glacier region. Specifically, these experimental campaigns have been carried out at Askole (3015 m a.s.l.) and Urdukas (3926 m a.s.l.) during summer 2011 and 2012, respectively. Trace gases and aerosol properties have been analyzed as a function of local meteorological parameters and "synoptic-scale" air-mass back-trajectories. This allowed to obtain the first information about climate forcers (short- and long-lived) in this remote mountain area.

3.2 Measurement sites

Akole (35°40'N, 75°48'E) is a village (about 300 inhabitants) located in the Braldu valley on the route to the Baltoro Glacier. Urdukas (35° 43' N, 76° 17') is distant more than 40 km from Askole and it is located along the Baltoro Glacier (Fig. 3.1). Both the measurement sites are well suitable for investigating the transport processes which can occur along the valley and the possible influence of local-regional anthropogenic emissions in affecting atmospheric composition in that pristine environment.
During summer months, meteorological conditions in the study area are predominantly dry and precipitations related to the wet Asian Monsoon are episodic and scarce. The local wind is strongly affected by the development of thermal circulation along the valley, with westerly up-valley winds during the day and night-time easterly down-valley winds.

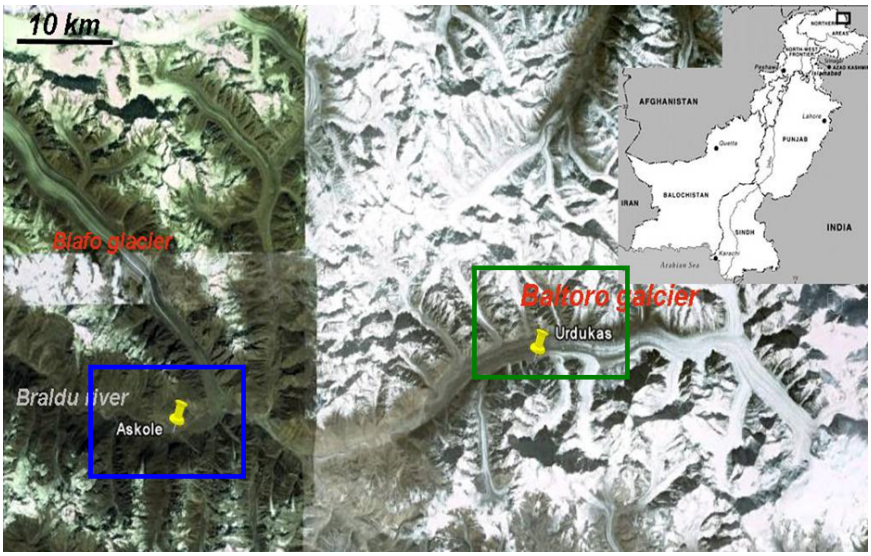

Figure 3.1: Satellite image of the Braldu Valley in the Pakistan Northern Areas, where the sampling sites Urdukas (green square: year 2011) and Askole (blue square: year 2012) are located.

3.3 Materials and methods

During Summer 2011, a 40-days intensive field campaign was carried out in August at Urdukas. Measurements of aerosol concentrations were performed by using an embedded Aeroqual AQM60 system, which was able to derive aerosol mass values (PM10, i.e. mass of particulate atmospheric aerosol with diameter lesser than 10 mm) throughout an optical particle counter (OPC).
During Summer 2012, trace gases (surface ozone and carbon dioxide) and aerosol measurements have been executed by using the SHARE – NANO system. This is a transportable (dimension: 38 × 50 × 65 cm, weight: 50 kg) embedded system, characterized by limited power consumption (50 W) which allows the system to be powered by solar panels. The system used during the PAPRIKA field campaign was equipped with an integrated weather station (Vaisala WXT 520), a condensation particle counter (TSI 3772) able to provide total number concentration for particles with diameters lower than 3 mm, an ozone analyzer (Ozone Monitor 220 2B Technologies) and a probe for carbon dioxide measurements (Vaisala CARBOCA GMP 343).

HYSPLIT Back-trajectories
In order to determine the synoptic origin of air masses reaching the measurement sites, 5-day back-trajectories were calculated every 6 hours (at 4:00, 10:00, 16:00 and 22:00) with the HYSPLIT back-trajectories model (*Draxler and Hess, 1998*). The model calculations were based on the GDAS meteorological field produced by NCEP with a horizontal resolution of 1° x 1°. Sub-grid scale processes, such as convection and turbulent diffusion, were not represented by the model. To partially compensate such uncertainties, additional back-trajectories were calculated, with endpoints shifted by ± 1° in latitude/longitude.

3.4 Results

Summer 2011 field campaign
Hourly PM10 values observed at Urdukas from July 21st to August 30th 2011 (Fig. 3.2), have been characterised by an average value of 7.7 ± 7.1 μg/m^3 (± 1-sigma). Such PM10 levels are rather low with respect of those observed during typical summer time conditions at other sites located in the central and southern Asia. As an instance *Shafer et al. (2010*) reported average PM10 values of 25 μg/m^3 at Biskhek (1250 m) and Karakol (2050 m), Kirghizstan, while PM10 ranging from 55 to 45 μg/m^3 have been observed at Manora Peak (1940 m asl), northern India (*Ram et al. 2011*). Nevertheless, the PM10 at Urdukas appeared higher than the values observed during the same period at the Himalayan site of NCO-P (Nepal, 5079 m a.s.l.) where the average PM10 was 1.1 ± 1.6 μg/m^3.
The PM10 time series inspection suggests that two different regimes of aerosol variability characterized the sampling site during the field campaign: the first period (21-27 July) was characterized by low PM10 values (about 3 μg/m^3), while the second period (28 July-30 August) was characterized by an increase of a factor 2.4 of the mean PM10 concentrations.
With the aim of investigating the possible role played by the large-scale atmospheric circulation in modulating the observed PM10 behavior, air-mass back-trajectories ensembles have been calculated by the HYSPLIT model. From this analysis, we preliminary assessed that during the first measurement period (21-27 July, when lower PM10 have been observed) the Baltoro region was affected by a "regional" circulation, while from the following days (when higher PM10 characterized the measurement site) the air masses flow were significantly different, with more "long-range" fingerprints which possibly favored the advection of air-masses richer in mineral dust from the Taklimakan region (Fig. 3.3). Under these conditions a "special event" with PM10 hourly value exceeding 300 μg/m^3 was detected.

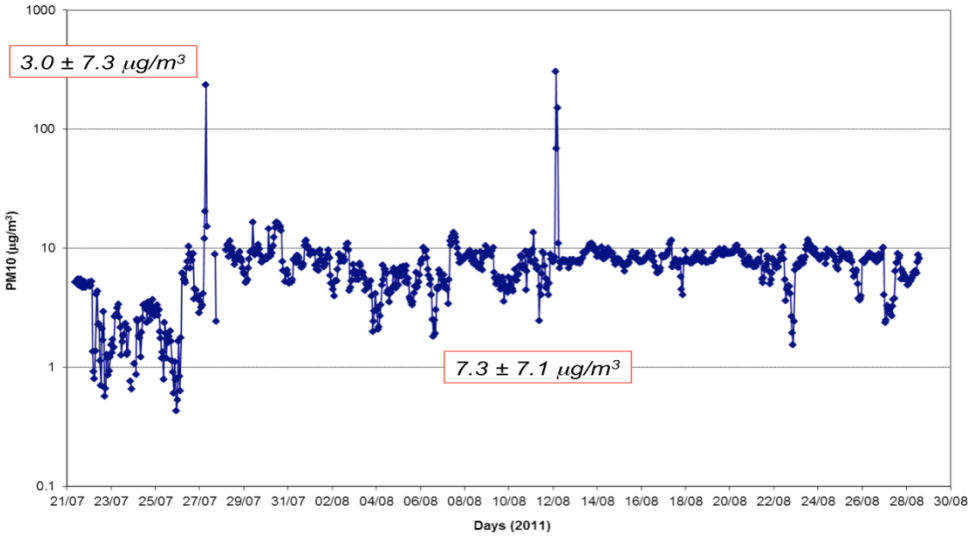

Figure 3.2: PM10 concentrations at Urdukas during the summer of 2011 (July 21st - August 30th). Red boxes report mean and standard deviation of PM10 concentrations associated to two different periods, 21–27 July upper box) and 28 July–30 August 2011 (lower box).

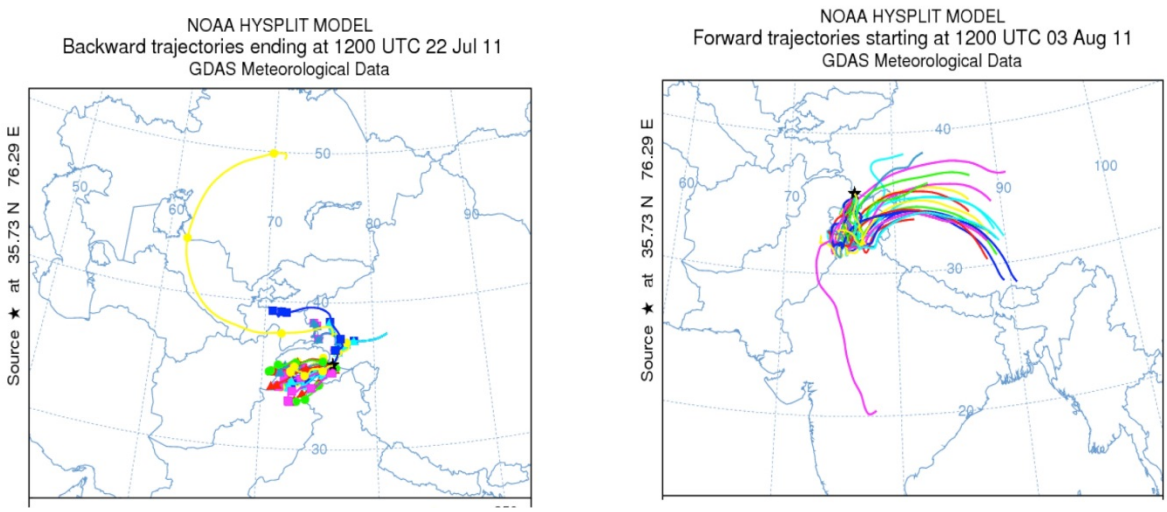

Figure 3.3: HYSPLIT back trajectories ending at 12:00 UTC of July 22nd (August 3rd) on the left (right) panel.

Summer 2012 field campaign

During the experimental campaign carried out at Askole on summer 2012, the first continuous characterization of trace gases and aerosol particles variability has been obtained for the Baltoro region. Meteorological parameters and carbon dioxide (CO_2: 394.3 ± 6.9 ppm, N=6057) data have been collected for the whole campaign period (with a major data gap on19th - 31st October due to a failure of the acquisition system), while surface ozone (O_3: 31.7 ± 10.4 ppb, N=3711) and particle number concentration (N_p: 1571 ± 2670 cm^{-3}) were collected until 7th October and 23rd September, respectively.

The mountain wind regime clearly influenced the diurnal behavior of atmospheric composition at the measurement site. In fact, aerosol particle and trace gases showed a typical diurnal cycle. The lowest particle concentrations have been observed at night, while a considerable increase was present around noon (Fig. 3.4). This behavior suggests that aerosol particles from the lower troposphere can reach Askole thanks to the day-time up-valley winds, while during the night cleaner air masses, more representative of the upper troposphere, are transported by down-valley

winds. The influence of the mountain wind regimes on O_3 and CO_2 was investigated by considering the average diurnal variation of normalized values (ΔO_3, ΔCO_2), obtained by subtracting daily means from the actual 15-min O_3 and CO_2 mixing ratio values.
As pointed out by this analysis, the surface O_3 average diurnal variation is also characterized by lower values during the night (00:00 – 4:00) and a peak during the afternoon-evening (14:00 – 19:00), with average diurnal cycle amplitude of about 8 ppb. On average, the diurnal O_3 peak occurred with a few hours delay in respect to the Np peak and the maximum of the up-valley wind speed (Fig. 3.5). As also reported considering data from other mountain stations in the world (see e.g. *Cristofanellli et al., 2010; Cristofanelli and Bonasoni 2009*), this suggests the transport of air-masses richer in O_3 from along the valley, possibly influenced by photochemical production due to the regional-scale anthropogenic precursor emissions. The presence during day-time (nigh-time) of air-masses representative of the lower troposphere (free troposphere) is also testified by the CO_2 average diurnal variation, which showed lower mixing ratios (on average: -4 ppm) in respect to night-time values. In fact, during summer season, air masses from the atmospheric boundary layer are depleted in CO_2 in respect to free-troposphere or upper tropospheric air masses due to the vegetation uptake by photosynthesis (e.g. Colombo et al., 2000).

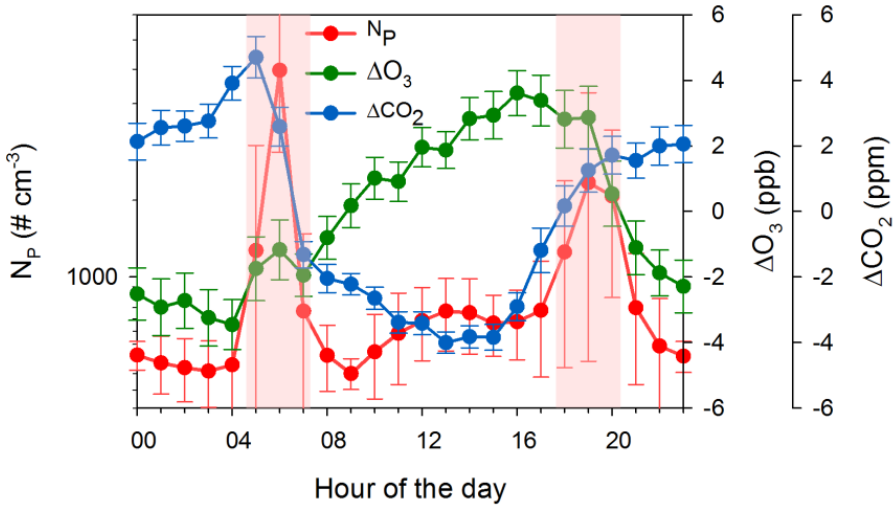

Figure 3.4: Typical diurnal variations for Np (red), DO3 (green) and DCO2 (blue). The vertical bars denote the expanded uncertainties (p<0.05) of the mean, while the shadow areas the periods possibly affected by the "local pollution events".

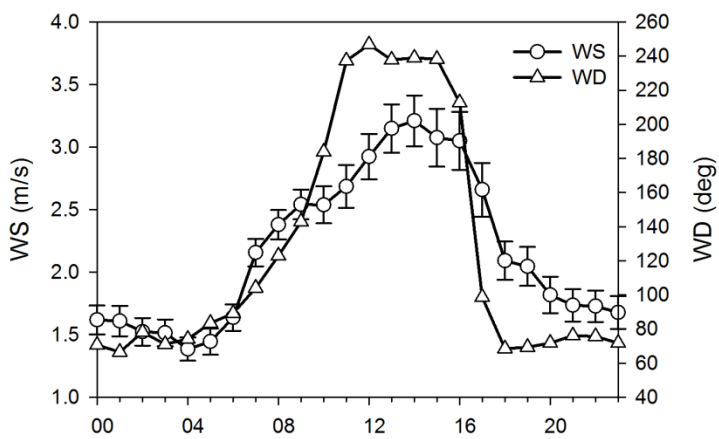

Figure 3.5: Average diurnal variations for wind speed (WS) and direction (WD). The vertical bars denote the expanded uncertainties (p<0.05) of the mean.

The most striking feature in the Np observations (Fig. 3.6) is the presence of systematic concentration peaks which occurred at the early morning (from 5:00 to 7:00) and at evening (from 18:00 to 20:00).A detailed inspection of the internal working parameters of the SHARE-NANO system, did not reveal any evident malfunctioning able to explain these anomalous peaks. The time of day at which these peaks occurred perfectly corresponds to the time at which the people from the village burn biomass, especially for cooking. At Askole, during summer season, the population uses very simple cooking systems, often represented by open fires with rough chimneys that guarantee the smoke ventilation from traditional houses to the outdoor. It is thus conceivable that the particle peaks could be ascribed to the domestic emissions from the near village.

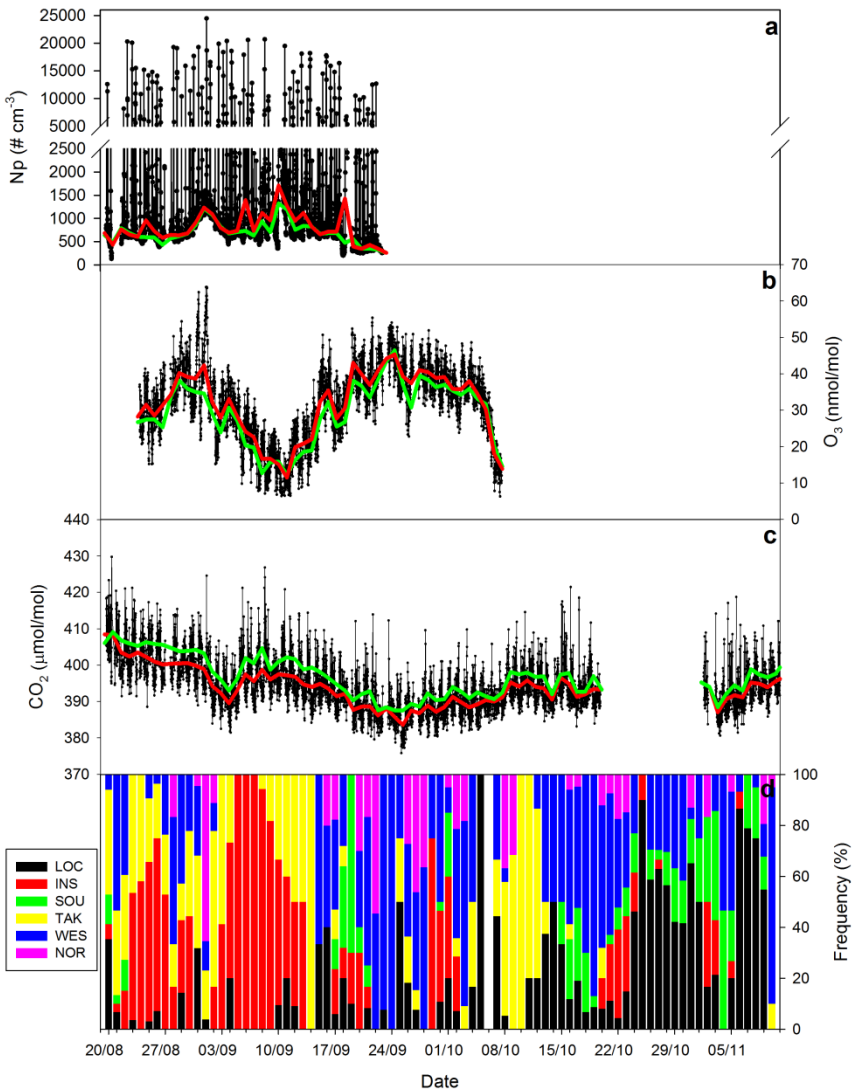

Figure 3.6: Time series of CPC particle number concentration (Np, panel a), surface ozone (O_3, panel b), carbon dioxide (CO_2, panel c) and daily air-mass circulation occurrences (panel d, WES-Westerly; TAK-Taklamakan; LOC-Local; SOU-Southern Pakistan; INS-Indian Subcontinent; NOR-Northerly). Red lines denote daily averages (computed excluding the "local contamination events"), while green lines represent night-time (between 21:00 and 4:00) averages.

Excluding the "local contamination events", the Np median concentration at Askole (676 cm^{-3}) is comparable with the median value (657 cm^{-3}) obtained during the same period at the NCO-P. For NCO-P the Np variability appeared to be in agreement with early measurement results provided by *Sellegri et al (2010*). However, it should be pointed out that NCO-P is strongly affected by the occurrence of new particle formation events, which can significantly affect Np. With the aim of

comparing Askole results with other mountain measurements performed in Asia, we calculated Np for STP conditions (i.e. 1013 hPa and 0 °C). At the Mukteshwar station (at the foothills of the Indian Himalayas at 2180 m a.s.l.) and at Mount Waliguan (China, 3816 m a.s.l.), as presented by Komppula et al. (2009) and Kivekäs et al. (2009), average particle (10–800 nm) number concentrations were more than 50% higher (3480 cm^{-3} and 3280 cm^{-3}, respectively) than the ones collected at Askole (1038 cm^{-3}). The Mukteshwar station, located at a lower height, is much more influenced by the very high concentrations encountered in the boundary layer of the Indo-Gangetic plains.

By neglecting the "local contamination events", the O_3 average values (31.8 ± 9.9 ppb) were lower than the mixing ratios values observed during the same period at the NCO-P (38.6 ± 8.0 ppb) which were not statistically different from the "representative" monsoon values reported by *Cristofanelli et al. (2010)* for years 2006 and 2007 (39 ± 10 ppb). The lower O_3 values observed at Askole are significantly influenced by the transport of air-masses poor in O_3 from Indian Subcontinent and Taklimakan desert, as deduced by HYSPLIT analyses. As pointed out by laboratory/model studies (e.g. *Hanisch and Crowley, 2003*) and atmospheric observations (e.g. *Bonasoni et al., 2004; Umann et al., 2005*), mineral dust may decrease tropospheric O_3 due to heterogeneous chemistry and a decreased efficiency of photochemical production. It is thus conceivable that air-masses coming from Taklamakan desert were characterised by low O_3 values. During these specific periods, also increases of CO_2 daily values have been observed. Indeed, due to the stronger anthropogenic emissions, CO_2 is expected to have high source over the Indo-Gangetic plains (e.g. Baker et al., 2010); while the Taklamakan desert, having an arid climate and being covered by barren land or sparse vegetation, can be considered as a region short of sinks of CO_2 (Hou et al., 2013), especially during the vegetative season.

As already mentioned, besides being affected by a significant diurnal variability, the atmospheric composition measurements at Askole were also characterized by significant day-to-day variations (Fig. 3.6), thus indicating that processes occurring at synoptic (or larger) scales can play a role in determining aerosol and trace gas behaviors in this remote region. With the aim of specifically investigating this point, hourly Np, O_3 and CO_2 values were analyzed as a function of the different air-mass origin and paths. Even if particular caution should be used in interpreting these modeling tools in a complex high mountain region like the Karakorum, some robust features have been pointed out. To summarize, lower O_3 and higher CO_2 values were observed in concomitance with possible air-mass transport from South Asia and Taklamakan desert, while higher O_3 mixing ratios have been mostly tagged with westerly and northerly air-masses, possibly indicating transport from the free troposphere. Concerning Np, contributions from the Indian Sub-continent appeared to be the dominant one for "intermediate" values (from 500 to 900 cm^{-3}). This can be understood as indicative particles concentration background in the free troposphere over the HKKH region, driven by long-range transport. In parallel, INS air-masses also contribute for the 50% of the upper Np values (> 1300 cm^{-3}), indicating that long-range transport from South Asia is a major source of fine particles in the Karakorum.

3.5 Summary

During summer 2011, PM10 measurements were carried out at Urdukas, along the Baltoro Glacier. Even if relatively low PM10 values were observed on average (7.7 ± 7.1 $\mu g/m^3$), transport of mineral dust from the Taklimakan desert episodically increased the aerosol loading (with a peak event of 300 $\mu g/m^3$).

The experimental campaign carried out at Askole on summer 2012, indicated that the domestic combustion could represent a possible systematic source of contamination in the valley. Excluding these local contamination events, mountain thermal wind regime dominated the diurnal variability of Np, O_3 and CO_2. Nevertheless, the variability of the observed climate forcers appeared to be dominated by day-to-day changes. Part of the day-to-day atmospheric composition variability can

be ascribed to synoptic circulation variability. In particular, low O_3 and high CO_2 values were observed associated with possible air-mass transport from South Asia and Taklamakan desert, while long-range transport from South Asia was a major source of fine particles in the Karakorum, and higher O3 have been mostly tagged with air-masses possibly from the free troposphere.

References

Bonasoni, P., Cristofanelli, P., Calzolari, F., Bonafè, U., Evangelisti, F, Stohl, A., Zauli Sajani, S., van Dingenen, R., Colombo, T., and Balkanski, Y., 2004. Aerosol-ozone correlations during dust transport episodes. Atmospheric Chemistry and Physics 4, 1201-1215.

Bonasoni, P., Laj, P., Marinoni, A., Sprenger, M., Angelini, F., Arduini, J., Bonafè, U., Calzolari, F., Colombo, T., Decesari, S., Di Biagio, C., di Sarra, A. G., Evangelisti, F., Duchi, R., Facchini, MC., Fuzzi, S., Gobbi, G. P., Maione, M., Panday, A., Roccato, F., Sellegri, K., Venzac, H., Verza, GP., Villani, P., Vuillermoz, E., and Cristofanelli, P., 2010. Atmospheric Brown Clouds in the Himalayas: first two years of continuous observations at the Nepal Climate Observatory-Pyramid (5079 m). Atmospheric Chemistry and Physics 10, 7515-7531.

Colombo, T., Santaguida, R., Capasso, A., Calzolari, F., Evangelisti, F., and Bonasoni, P., 2000. Biospheric influence on carbon dioxide measurements in Italy. Atmospheric Environment 34, 4963-4969.

Cristofanelli, P., and Bonasoni, P., 2009. Background ozone in the southern Europe and Mediterranean area: Influence of the transport processes. Environmental Pollution 157, 1399-1406.

Cristofanelli, P., Bracci, P., Sprenger, M., Marinoni, A., Bonafè, U., Calzolari, F., Duchi, R., Laj, P., Pichon, J.M., Roccato, F., Venzac, H., Vuillermoz, E., and Bonasoni, P., 2010. Tropospheric ozone variations at the Nepal Climate Observatory-Pyramid (Himalayas, 5079 m a.s.l.) and influence of deep stratospheric intrusion events. Atmospheric Chemistry and Physics 10, 6537-6549.

Draxler, R. R., and Hess, G. D., 1998. An overview of the HYSPLIT_4 modelling system for trajectories, dispersion and deposition. Australian Meteorological Magazine 47, 295-308.
correlations during the June 2000 MINATROC intensive measurement campaign at Mt. Cimone. Atmospheric Chemistry and Physics 3, 725-738.

Hanisch, F., and Crowley, J. N., 2003. Ozone decomposition on Saharan dust: an experimental investigation. Atmospheric Chemistry and Physics 3, 119-130.

Hewitt, K., 2005. The Karakoram anomaly? Glacier expansion and the 'Elevation Effect', Karakoram Himalaya. Mountain Research and Development 25(4), 332-340.

Kivekäs, N., Sun, J., Zhan, M., Kerminen, V.-M., Hyvärinen, A., Komppula, M., Viisanen, Y., Hong, N., Zhang, Y., Kulmala, M., Zhang, X.-C., Deli-Geer, and Lihavainen, H., 2009. Long term particle size distribution measurements at Mount Waliguan, a high altitude site in inland China. Atmospheric Chemistry and Physics 9, 5461-5474.

Komppula, M., Lihavainen, H., Hyvärinen, A.-P., Kerminen, V.-M., Panwar, T. S., Sharma, V. P., and Viisanen, Y., 2009. Physical properties of aerosol particles at a Himalayan background site in India. Journal of Geophysical Research, 114, D12202.

Sellegri, K., Laj, P., Venzac, H., Boulon, J., Picard, D., Villani, P., Bonasoni, P., Marinoni, A., Cristofanelli, P., and Vuillermoz, E., 2010. Seasonal variations of aerosol size distributions based on long-term measurements at the high altitude Himalayan site of Nepal Climate Observatory-Pyramid (5079 m), Nepal. Atmospheric Chemistry and Physics 10, 10679-10690.

WP4: Integrated climate-glacier-water modeling

Elisa Palazzi, Antonello Provenzale, Jost von Hardenberg, Silvia Terzago,
Letizia Congedi, Luca Filippi, Francesca Viterbo, Antonio Parodi,
Chiara Cagnazzo, Federico Fierli, Silvia Bucci (ISAC-CNR)

Fabien Solmon, Filippo Giorgi (ICTP)

Daniele Bocchiola and co-workers (POLIMI)

4.1 Introduction

Reliable estimates of hydrological responses and of water availability in future decades in the Hindu-Kush Karakoram Himalaya (HKKH) region require the use of a modeling chain based on a sequence of steps. At the largest scales, Global Climate Models (GCMs) provide climate scenarios for the whole planet. At intermediate scales, Regional Climate Models (RCMs) nested in the global models and downscaling procedures provide a higher-resolution estimate of the climatic conditions. Finally, hydrological models for runoff and groundwater flow simulate the hydrological response at the basin scales. In the framework of the PAPRIKA project, such a modeling chain, schematically shown in Fig. 4.1, was implemented.

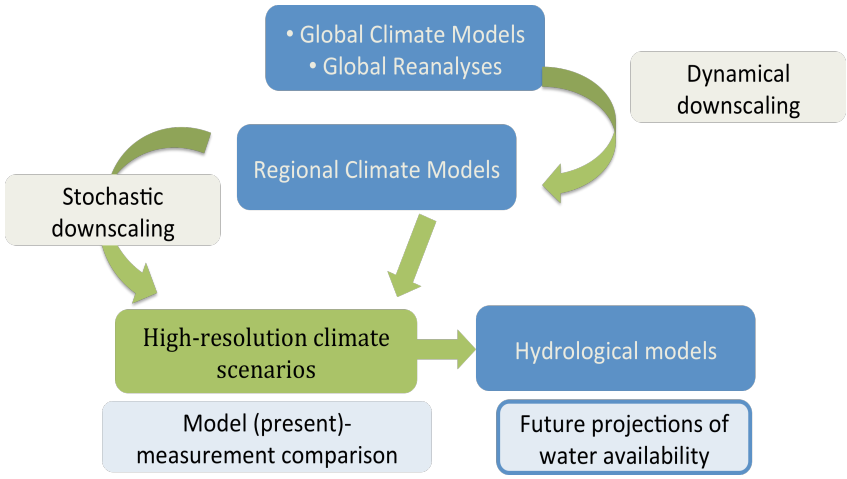

Figure 4.1: Scheme of the modeling chain connecting global climate models to hydrological models, for future projections of water availability.

Here we focus on the description of the single elements of the modeling chain, by presenting the results obtained during the project from both GCM and RCM simulations -including hydrostatic and non-hydrostatic models-, the implemented stochastic rainfall downscaling procedure, as well as the hydrological model used during the project. These tools have been employed to address a number of research questions, especially focused on a better understanding of the hydrological cycle in the HKKH region, particularly on precipitation, snow cover and snow depth, circulation patterns, on the direct and indirect effects of aerosol on atmospheric dynamics and precipitation in this area, and on the hydrological response to the meteorological and climate forcing. As already mentioned, we used an ensemble of modeling tools including coarse-scale GCMs, hydrostatic and

non-hydrostatic RCMs, downscaling methods and one hydrological model. Different kinds of observed data and reanalysis data, have also been used to perform model validations and process-oriented evaluations. The comparison between model outputs and the observations/reanalysis data is a necessary step before using models to make climate projections and critically analyzing future conditions.
In this report, we describe the various modeling tools developed and employed during the project, providing an overview of the obtained results on various aspects of the current state of hydrological cycle in the HKKH region, particularly in terms of models evaluation, validation, inter-comparisons, and calibration. We leave to the report on WP5 a description and discussion of the climate projections produced during the project for the HKKH region, aimed at analyzing the projected changes of the hydrological cycle and its various components in the next decades.

4.2 Modeling tools

4.2.1 The EC-Earth GCM

EC-Earth is one state-of-the-art fully-coupled GCM, based on the concept of seamless prediction (*Hazeleger et al., 2012),* developed in the framework of the European Consortium EC-Earth, which gathers more than 20 institutions, including ISAC-CNR, from 10 different European countries. The configuration of the EC-Earth version (v2.3) employed in PAPRIKA runs at T159 horizontal spectral resolution (corresponding to about 1.125° latitude-longitude) with 62 vertical levels for the atmosphere, and an irregular grid with about 1° resolution and 42 vertical levels for the ocean. The EC-Earth simulations were performed by ISAC-CNR using CASPUR supercomputing resources. In the framework of PAPRIKA we used the historical (1850-2005) model output and two scenario outputs for the period 2006-2100, based on the Representative Concentration Pathways (RCPs) for anthropogenic emissions, RCP 4.5 and RCP 8.5 (*Moss et al., 2010).* RCP 4.5 is a scenario that stabilizes anthropogenic radiative forcing at 4.5 Wm^{-2} (compared to preindustrial) in the year 2100, while the RCP 8.5 scenario assumes no effective climate change policies and a continuation of high energy demand and greenhouse gas emissions, leading to 8.5 Wm^{-2} of anthropogenic radiative forcing in 2100.

4.2.2 The Coupled Model Intercomparison Project Phase 5 (CMIP5) models

We also analyzed the historical and scenario simulations of an ensemble of climate models participating in the CMIP5 experiment (the EC-Earth simulations performed by the members of the EC-Earth consortium are also included in the CMIP5 model ensemble), available at the Program for Climate Model Diagnosis and Intercomparison (PCMDI) web page (http://cmip-pcmdi.llnl.gov/cmip5/). With respect to the previous generation of climate models (CMIP3, *Meehl et al, 2007),* CMIP5 includes more and new GCMs with generally higher spatial resolution (from about 0.5° to 4° for the atmospheric component and from 0.2° to 2° for the oceanic component), an expanded variable list, a broader range of experiments and, in general, more Earth System Models (ESMs), including a representation of various biogeochemical cycles (*Taylor et al, 2012*). In comparison to the CMIP3 models, CMIP5 climate models generally have improved representation of aerosol-cloud interactions (*Wilcox et al, 2013)* and represent both the direct effect of sulfate aerosol and some of the indirect effects involving cloud droplet number and size. With respect to the past, moreover, a higher number of CMIP5 ESMs includes an interactive representation of aerosol species *(Wilcox et al, 2013*). It is worth underlying that some CMIP5 climate models share a common lineage and are not really independent each other. *Masson and Knutti (2011),* by analyzing the previous CMIP 2/3 climate models, showed that one reason some models are closely related is because they share common code (in particular the same atmospheric model) or they are developed in the same center.

4.2.3 ECHAM-HAM

We performed global aerosol simulations with the model ECHAM5-HAM, for a series of different anthropogenic forcing datasets. The model couples the global climate model ECHAM5 (*Roeckner et al. 2003*) with the HAM module (Hamburg Aerosol Module, *Lohmann et al. 2009),* which models the dynamics, the microphysics and the transport of the main atmospheric aerosols and their radiative feedbacks. In particular HAM contains the microphysical core M7 (*Vignati et al. 2004),* based on the representation of particle distributions as the superposition of log-normal modes peaked at different particle size classes, and reproduces the main aerosol emission, sedimentation and wet and dry scavenging processes. The included aerosol compounds are sulfates, black carbon, organic matter, sea salt and mineral dust. The emissions of dust, sea salt and oceanic dimethyl sulfide (DMS) are computed on-line, while other natural and anthropogenic emissions are prescribed. Secondary Organic Aerosols (SOA) emissions are prescribed monthly and added to Particulate Organic Matter emissions. The main aerosol optical and microphysical properties (optical depth, number and mass concentrations) are simulated by the model. The spatial resolutions used were T42 and T63 in spectral space (corresponding to resolutions of about 2.8° and 1.8°, respectively, on a Gaussian grid), with 19 and 31 vertical levels respectively. In addition to aerosol emissions provided from the AeroCom 2000 archive (*Dentener et al., 2006)* we considered also ACCMIP emissions (*Lamarque et al., 2010)* for year 2000, integrated by yearly wildfire emissions from the GFED3 archive (*van der Werf et al., 2010).* We also considered a correction of SO2 emissions in South-East Asia based on the REAS archive (*Ohara et al., 2007).* In the course of the project we ported HAM1 from ECHAM 5.3 to a version of ECHAM 5.4 coupled with the ocean model OPA 8.2 (*Madec et al. 1999*) and the LIM2 model for sea ice (*Timmermann et al., 2005).*

4.2.4 RegCM4 RCM

Regional climate simulations have been performed with the hydrostatic regional climate model (RCM) RegCM4, originally developed at the National Center for Atmospheric Research (NCAR), and now maintained at ICTP (http://www.ictp.it/research/esp/models/regcm4.aspx). RegCM4 represents a recent development of the previous RegCM3, and includes new land surface, planetary boundary layer, and air-sea flux schemes, a mixed convection and tropical band configuration, modifications to the pre-existing radiative transfer and boundary layer schemes, and a full upgrade of the model code towards improved flexibility, portability, and user friendliness. RegCM4 includes a simplified aerosol module, particularly suited for long-term climate simulations, which represents the dynamics of Sulfate, Organic and Black Carbon (OC and BC), desert dust and sea spray. For each of the tracers the aerosol module includes emission sources, transport by resolvable scale winds, sub-grid scale turbulence and deep convection, dry and wet removal processes, simplified chemical transformations, direct radiative forcing both in the solar and infrared spectrum, and a simplified representation of indirect aerosol effects on cloud microphysics. The module provides deposition fluxes of light-absorbing aerosols such as Black Carbon and dust, making it suitable for simulating the effects of aerosol deposition on the snow and the related changes in snow texture and optical properties. The model was run by ICTP at 50 km resolution on the standard domain defined for the Indian subcontinent region for the CORDEX project. Three simulations were performed, in which the external boundary conditions have been provided for present conditions (2000-2009) by the ERA-Interim (ECMWF) reanalysis project and by the CMIP5 EC-Earth v2.3 simulations performed by ISAC-CNR during the project. A future scenario simulation was also performed for the decade 2040-2050, forced using the RCP4.5 scenario run of EC-Earth v2.3. In this future scenario simulation the RCP 4.5 - CAM large scale aerosol boundary concentrations and the RCP 4.5 anthropogenic emissions of SO2 and carbon aerosols were used. Dust and sea-salt aerosol emissions were computed online.

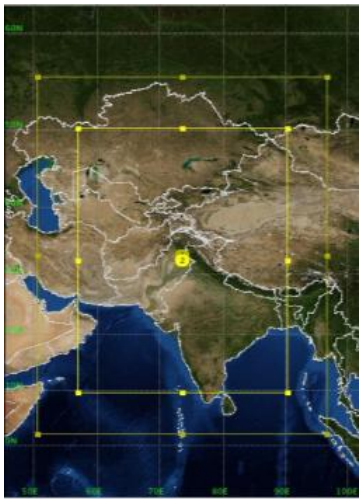

Figure 4.2: The two nested WRF simulation Domains, d01 and d02.

4.2.5 WRF RCM

In the framework of PAPRIKA we used the Advanced Research Weather Research and Forecasting model (WRF, www.wrf-model.org/), version 3.3.1, to simulate the atmospheric conditions that characterized the most intense days of 2010 Pakistan flood (July 26th-31st, 2010). WRF is a fully compressible, 3D, Eulerian, non-hydrostatic model conservative for scalar variables, used both for regional and global application and in many research fields.

In the framework of PAPRIKA, we performed simulations over two domains, one with a 14 km grid spacing and the other, nested in the former, at 3.5 km resolution (Fig. 4.2), covering the upper and lower boundaries of the cloud-permitting range (*Arakawa 2004),* in a two-way nesting mode.

The vertical coordinate was discretized in 42 levels, equally spaced in hydrostatic pressure coordinates, with 10 levels in the lowest 2.5 km. A higher number of layers near the surface was used to better resolve the atmospheric flow over the complex orography of the simulated mountainous region and its associated convective activity. The turbulent parameterization employed in the simulations is the Mesoscale 1D scheme, and the planetary boundary layer scheme is the Yonsei University (YSU) one (*Hong et al., 2006*). The boundary and initial conditions for the experiments were provided by the ERA-Interim reanalysis project at its native resolution, namely 0.7° (~78 km). We performed a set of model simulations employing different convection and microphysics configurations, and tested the model with different initialization days. The best configuration was selected through a comparison with the observations in terms of daily rainfall, columnar water vapor content, wind speed and direction.

4.2.6 Stochastic rainfall downscaling with RainFARM

An effective approach to bridge the scale gap between climate change scenarios obtained from GCM and even RCM simulations and the small scales needed for impact and assessment studies is stochastic downscaling. The Rainfall Filtered AutoRegressive Model (RainFARM) (*Rebora et al. 2006*) is a stochastic downscaling procedure, specifically devised for precipitation, based on the nonlinear transformation of a linearly correlated stochastic field, generated by small-scale extrapolation of the Fourier spectrum of a large-scale field. The original RainFARM technique, developed at ISAC-CNR for the spatial-temporal downscaling of individual precipitation events on meteorological time scales (a few days), has been recently modified to perform the downscaling of precipitation fields on climatic time scales. We tested this RainFARM variant over an orographically complex area in northern Italy for which a dense network of rain gauges is available, by applying the downscaling procedure to the output of one state-of-the-art Regional Climate Model and then comparing the downscaled model results with the raingauge observations, obtaining a satisfactory agreement between the downscaled model results and the point-scale observations (*D'Onofrio et al., 2014).*

Our first use of the RainFARM model in the framework of PAPRIKA, was its application to satellite precipitation measurements (TRMM, 25 km resolution) over the Karakoram area rather than to model data. In fact, few and sparse in-situ rain gauges are still available for the mountainous regions of Northern Pakistan, and their measurements are strongly biased by altitude (since rain gauges are mainly located in valley floors, at lower elevations than those where maximum precipitation occurs). Therefore, the application of the downscaling procedure to coarse-scale satellite measurements can be thought of as an effective way to obtain high-resolution synthetic precipitation estimates for poorly gauged regions.

4.2.7 The glacio-hydrological model

To reproduce the hydrological dynamics we use a semi-distributed model based on altitude belts, able to reproduce ice and snow dynamics, evapotranspiration, recharge of groundwater reservoir, discharge formation and routing to the control section. This model needs a few input data, i.e. a DEM, daily values of precipitation and temperature, information about soil use, altitudinal gradient of temperature and precipitation (estimated from PMD and Ev-K2 CNR meteorological stations) and a few others parameters. The model considers two mechanism of flow formation: superficial and groundwater flow. The full model equations are reported e.g. in *Groppelli et al. (2011),* and *Bocchiola et al. (2011),* and we refer to those papers for details. To describe the ice and snow melting process, a simple degree-day approach is used. The ice melt factor is based upon data from ice ablation stakes deployed during the PAPRIKA field campaigns, taking into account also the debris thickness effects. Snowmelt was also tackled using a degree-day approach and melt factor. For the Shigar basin model, the degree-day factor for snow melt (DDs) was estimated from MODIS snow cover images (*Bocchiola et al., 2011),* depending also on the month of the year (the maximum value being in August). To better describe the ice contribution, a module which is specifically designed to take into account glacier dynamics, as driven by gravity, was introduced. Specifically, the model uses a simplified ice flow approach, by shifting a proper quantity of ice from an altitude belt to the lower one. The quantity of ice is evaluated using an ice velocity value. After a screening of literature approaches to ice flow modeling (*Oerlemans, 1997; 2001*) we chose to model the ice flow velocity using an equation depending upon ice depth:

$$V_{ice,i} = f_d \cdot h_{ice,i}^{\ 4} + f_s \cdot h_{ice,i}^{\ 2} \qquad (4.1)$$

with $h_{ice,i}$ [m] the ice water equivalent in the belt i, and f_s and f_d are two parameters (of internal deformation and basal sliding) which were calibrated against the observed velocity values at stakes and from remote sensing (Quincey *et al.*, 2011). Ice flow occurs then by

$$h_{ice,i}(t+\Delta t) = h_{ice,i}(t) - F_{i\to i-1}(t) + F_{i+1\to i}(t)$$
$$F_{i\to i-1} \propto V_{ice,i} \qquad (4.2)$$

where the amount of ice water equivalent $h_{ice,i}$ in the belt i at time t results from the balance of the ice passing from belt i to the lower belt i-1, $F_{i\to i-1}$, and the ice coming from the upper one. Ice flow module is routed once a year, using ice depth as resulting from the seasonal mass budget. To initialize ice thickness in the model, we adopted values based upon the 2013 estimates, carried out in Concordia, of about 850 m ice thickness at the study site. Depth along the flow line has been estimated from a simple evaluation of the basal shear stress. The equations of the model are solved using fifty equally spaced elevation belts inside the basin. The flow discharges from the belts are routed to the outlet section through a semi-distributed flow routing algorithm, based upon the conceptual model of the instantaneous unit hydrograph, IUH. For calculation of the in stream discharge we hypothesize two (parallel) systems (groundwater, overland) of linear reservoirs (in series) each one with a given number of reservoirs (ng and ns) for each belt. In this way, each belt possesses a different lag time (and the farther belts have the larger lag times). The hydrological model uses a daily series of precipitation and temperature from one representative station, here Askole, and the adopted vertical gradients to project those variables at each altitude belt. Topography is represented by a DTM model, with 30m spatial resolution, derived from the ASTER (2006) mission, used to define altitude belts and local weather variables against altitude.

4.3 Global and regional climate simulations and atmospheric variability, including aerosol transport

4.3.1 Simulation of the current precipitation in the HKKH region

We have analyzed the properties of precipitation in the Hindu-Kush Karakoram Himalaya (HKKH) region using currently available data sets. We have considered satellite rainfall estimates (TRMM), reanalyses (ERA-Interim), gridded in situ rain gauge data (APHRODITE, CRU, and GPCC), and a merged satellite and rain gauge climatology (GPCP). The data are compared with simulation results from the global climate model EC-Earth (v2.3). Figure 4.3 shows, as an example, the spatial map of summer precipitation, averaged over the decade 1998-2007, in the HKKH region from the various employed data sets.

We have defined two domains, shown in Fig. 4.4, which contain two sub-regions of the HKKH affected by different circulation and precipitation patterns: the Hindu-Kush Karakoram (HKK) in the west (containing the focus region of the PAPRIKA project), prone to the arrival of westerly winds in winter and early spring and the Himalaya in the east, affected by the summer monsoon.

We have analyzed the precipitation annual cycle (see Fig. 4.5) and long-term trends (summarized in Table 4.1) of summer and winter precipitation in the two domains, focusing on mountain areas with elevation higher than 1000 m. All data sets, despite having different resolutions, coherently reproduce the mean annual cycle of precipitation in the western and eastern stretches of the HKKH. While for the Himalaya only a strong summer precipitation signal is present, associated with the monsoon, the data indicate that the Hindu-Kush Karakoram, which is exposed to mid-latitude western weather patterns (WWP, see section 3.1 for a better analysis of the mechanisms associated with these systems), receives water inputs in winter. Winter precipitation in the Karakoram, essentially occurring in form of snow, represents the main nourishment for the Karakoram glacier system.

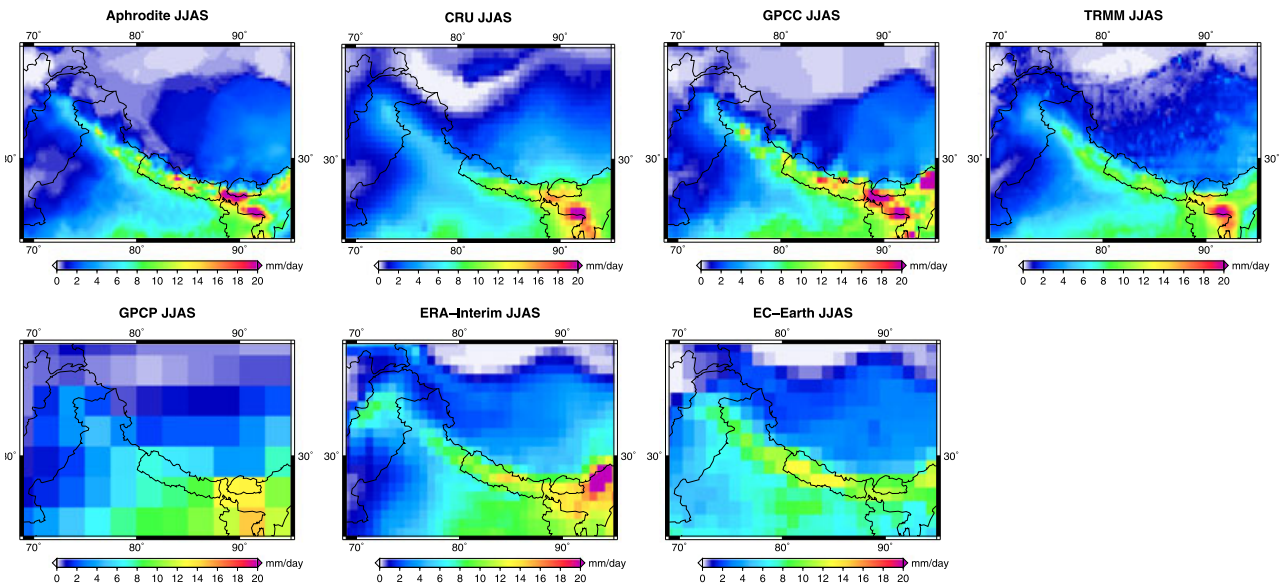

Figure 4.3: Multiannual mean (1998–2007) of summer (JJAS) precipitation over the region between 69°E–95°E and 23°N–39°N from the APHRODITE, CRU, GPCC, TRMM, GPCP, ERA-Interim, and EC-Earth model data sets.

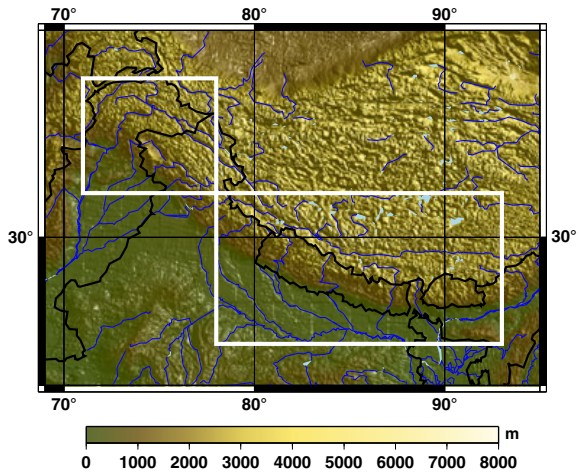

Figure 1.4: Map of the study area and the HKK (West) and Himalaya (East) domains.

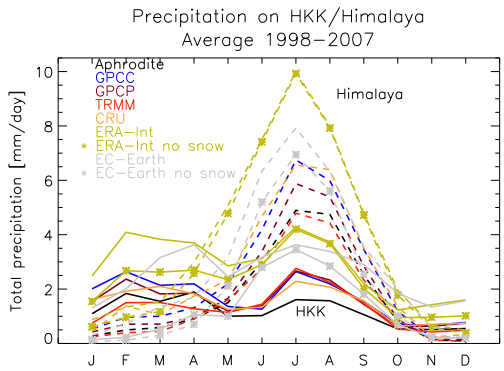

Figure 4.2: Monthly climatology of precipitation (averaged over 1998–2007) for the HKK (solid lines) and the Himalaya (dashed lines) sub-regions, for the datasets indicated in the legend. The lines with stars indicate liquid precipitation only.

The time series of seasonal precipitation (not shown here) confirm that the various data sets, in spite of their relative biases, provide a consistent measurement of interannual variability of precipitation in the HKKH region. As summarized in Table 4.1, the longest observational data indicate a statistically significant decreasing trend in summer (monsoon) precipitation in the Himalaya. None of the data sets, on the contrary, gives statistically significant precipitation trends, either positive or negative, in HKK during winter.

Table 4.1: Precipitation Trends (in mm/d/yr) in the HKK and Himalaya During Summer (JJAS) and Winter (DJFMA) for the Various Data Sets (in Parentheses the Years Over Which Trends Have Been Calculated). Bold Figures are Significant at the 95% Level (p-value Indicated in Brackets)

	JJAS		DJFMA	
	Himalaya	HKK	Himalaya	HKK
APHRODITE (1951–2007)	**–0.010(*p*=0.001)**	0.0	0.0	–0.003
CRU (1950–2009)	–0.008	0.002	**0.005(*p*=0.004)**	–0.001
GPCC (1950–2009)	**–0.021(*p*=0.001)**	0.0	**–0.004(*p*=0.000)**	0.002
TRMM (1998–2010)	0.015	0.057	–0.006	0.041
GPCP (1979–2010)	–0.012	**0.017(*p*=0.045)**	**–0.010(*p*=0.001)**	–0.007
ERA-Interim (1979–2010)	0.027	–0.011	–0.002	–0.012
EC-Earth (1950–2009)	**0.008(*p*=0.002)**	0.005	–0.001	0.0
* ERA-Interim (1979–2010)	0.027	–0.011	0.0	–0.007
* EC-Earth (1950–2009)	**0.014(*p*=0.000)**	**0.007(*p*=0.027)**	**0.001(*p*=0.050)**	0.001

Precipitation data from EC-Earth are in good agreement with the climatology of the observations, in terms of the overall rainfall spatial distribution (see, as an example, Fig. 4.3) and rainfall seasonality, i.e., the identification of the seasonal precipitation sources in the western and eastern stretches of the HKKH region. Unlike the observations, however, the model shows an increasing summer precipitation trend in the period 1950–2009 in the Himalayan region (see Table 4.1), possibly as a result of the poor representation of aerosols in this type of GCMs.

To better understand the impact of the modeled aerosols, as well as of other model features on the simulated HKKH precipitation, we have extended the EC-Earth analysis outlined above to an ensemble of thirty-two CMIP5 models. Differences in the employed models are related to their spatial resolution, the inclusion of interactive schemes for e.g., the chemistry-transport module, the representation of the aerosol radiative and indirect effects on clouds and precipitation. We have evaluated the historical model output against two precipitation data sets, the CRU and GPCC data, being the longest available data sets. The models have been evaluated in terms of both individual model outputs and multi-model ensemble mean (MMM).

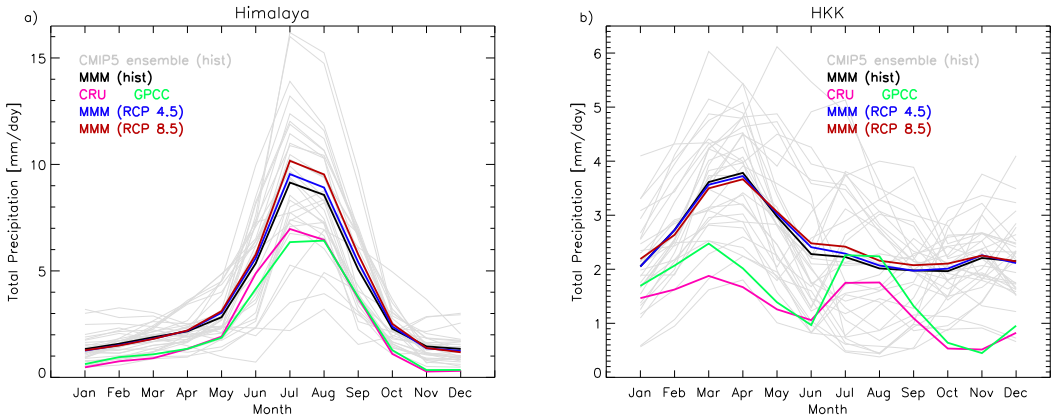

Figure 4.6: Mean annual cycle of precipitation in the Himalaya (a) and HKK (b), calculated as the multi-annual average over the years 1901-2005 (historical period) for each CMIP5 model (grey lines) and for their multi-model mean (MMM, black line). The solid blue and red lines represent the mean annual cycle of precipitation over the years 2006-2100 in the RCP 4.5 and the RCP 8.5 future scenarios, respectively, for the CMIP5 MMM. The CRU and GPCC observations with the pink and green lines, respectively.

The MMM overall shows an overestimation, compared to observations, of the climatological precipitation annual cycle in both HKK and Himalaya regions all over the year (see Fig. 4.6). This wet bias is consistent with the bias commonly seen in the precipitation simulated by the state-of-the-art GCMs over high-elevated terrains, such as the Tibetan Plateau, as reported in *Su et al (2012)*. However, the models exhibit a large spread relative to the MMM. The inter-model differences are particularly important in the HKK region, where precipitation annual cycles with very different characteristics are simulated.

We grouped the CMIP5 models providing a similar representations of the annual precipitation cycle in the HKK sub-region using the hierarchical clustering analysis technique, with a standard Euclidean distance as a distance metric and a complete linkage scheme for linking clusters together, so assuming no a priori knowledge about the features of any model. We identified four model clusters in the HKK region, giving rise to the four precipitation annual cycles shown in Fig. 4.7 (the shaded area includes the individual model realizations, the MMM is shown with the black solid line with symbols, the CRU and GPCC observations are shown with the pink and green lines respectively).

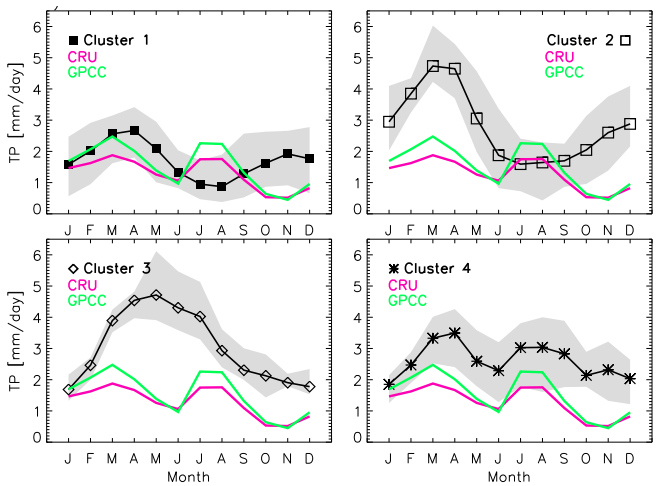

Figure 4.7: Mean annual cycle of precipitation in the HKK simulated by all models within each cluster (the grey shaded areas indicate the variability range of the models) and by their MMM. CRU and GPCC observations are shown with the pink and green lines, respectively.

Models in the first and in the second cluster simulate very small amounts of precipitation during

summer compared to winter/early spring precipitation. The main difference between them is that the models in the second cluster simulate on average larger precipitation amounts. The models in the third cluster display high precipitation values from March to August and one peak around May; all over the year precipitation values are strongly overestimated with respect to the CRU and GPCC observations. Finally, models in the fourth group present a simulated annual cycle which is most similar to the CRU and GPCC observations, in which the yearly precipitation distribution exhibits two peaks, one in late winter/early spring and the other in summer. This seasonal distribution of precipitation has been described and discussed in *Palazzi et al (2013)* and reflects the two main seasonal precipitation sources in the area, the wintertime western weather patterns and the summer monsoon. A third, lower, maximum in November can be mainly attributed to one single model (MRI-CGCM3). The mean annual distribution of precipitation reproduced by these models, however, exhibits a systematic wet bias relative to the observations. All models belonging to this cluster have a resolution of either 1.125° 1.25° longitude (high-resolution models), except the NorESM family models, having a coarser resolution of 2.5° longitude.
It was hardly possible, however, to clearly identify what model features play a dominant role in simulating precipitation annual cycles with a certain shape or amplitude, or in simulating the long-term precipitation trends that are in best agreement with the observations.

As for the historical (1901-2005) trends simulated by the CMIP5 GCMs, we found that only seven GCMs simulate, in agreement with the CRU and GPCC observations, a statistically significant decreasing trend in the Himalaya during summer. Five of these models are linked each other by sharing the same lineage. The seven GCMs listed above do not have particularly high horizontal resolution (from 1.875 to 2.8125° longitude), but all of them account for the indirect effect of sulfate aerosols and have an interactive aerosol scheme. Three models, on the other hand, simulate statistically significant trends of opposite sign for the historical period in this region and season. The other models simulate generally lower trends, either positive or negative, that are not statistically significant at the 95% level of confidence. In the Himalaya during winter, the MMM does not indicate significant precipitation trends in the historical period: about half of the models provide negative trends of precipitation, the other half provides positive, increasing precipitation trends. On the other hand, only two models give a statistically significant trend, indicating a decrease of total precipitation at a rate of about -0.2 mm/day per century in the period 1901-2005. It is worth pointing out, however, that the two observational datasets give different pictures of the historical winter precipitation trend in the Himalayan region: CRU data show a slight, positive and not significant trend, while GPCC shows a negative, statistically significant precipitation trend (-0.36 mm/day per century). In the HKK region, both observational datasets indicate positive, though not significant, precipitation trends in summer in the period 1901-2005. The MMM indicates a significant positive trend in this region and season, probably due to the significant positive trends, in the range from 0.3 to ~0.6 mm/day per century, simulated by five models. In the HKK region in winter, the MMM indicates negative precipitation trends throughout the historical period, statistically significant at the 95% confidence level.

4.3.2 Simulation of the current snow depth in the HKKH region

The HKKH mountains feed the most important Asian river systems, providing water to about 1.5 billion people. As a consequence, changes in snow dynamics in this area could severely impact water availability to downstream populations. Despite their importance, the snow amount, spatial distribution and seasonality in the region are still poorly known, owing to the limited availability of surface observations in such remote high elevation areas. Owing to the lack of reliable observations, we have analyzed the snow depth representation for the HKKH region in a set of CMIP5 GCM simulations. We found that the models with high spatial resolution (between 0.75-1.25 degrees) represent a more realistic spatial pattern of the winter snowpack with respect to the lower resolution models. The seasonal snow cycle displays a unimodal regime, as shown in Fig. 4.8, with a snow

depth maximum in February/March and almost complete melting in summer. The models generally indicate thicker snow depth compared to the ERA-Interim/Land reanalysis for the control period 1980-2005.

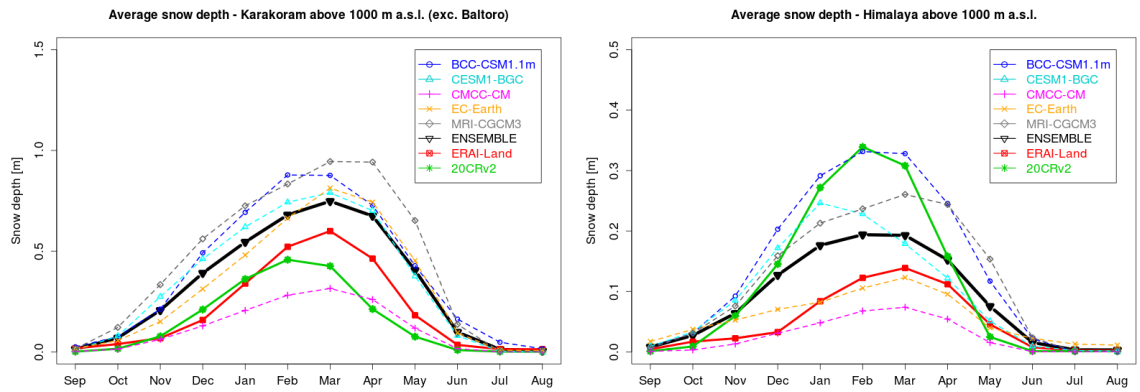

Figure 4.8: Seasonal variability of snow depth in HKK (left) and Himalaya (right) above 1000 m a.s.l., obtained from the high resolution CMIP5 GCMs. The panels refer to the multiannual monthly averages over the reference period 1980-2005.

During the historical period, the average winter snow depth ranges between 5.8 and 27.6 cm in the Himalaya region and from 24.6 to 91.6 in the Hindu-Kush Karakoram region, depending on the model. We recall that since these values represent averages over two large boxes, which include snow-free areas, they are not representative of the actual average snow height in snow-covered areas. The overall historical trends indicate a decrease of snow depth. The Hindu-Kush Karakoram mountains experienced a significant decrease of -2.7 cm/100y while the Himalaya registered a weaker, statistically non-significant decrease of -1.2 cm/100y (equivalent to decreases of 3.9%/century and 6.7% per century respectively, compared to the historical average).

Figure 4.9 shows the spatial patterns of the DJFMA snow depth trends for each of the high-resolution GCMs in the period 1911-2005 (95-years long period). We reported only the statistically significant trends at the 95% confidence level. We compared the GCM results to the 20CRv2 reanalysis.

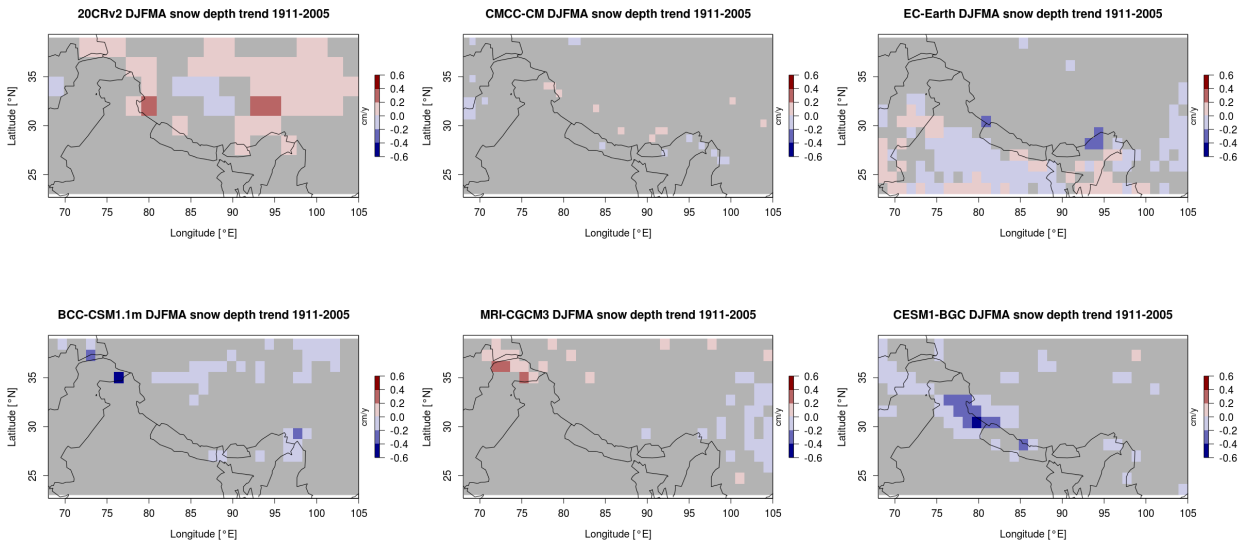

Figure 4.9: Spatial distribution of the winter (DJFMA) snow depth trends, estimated over the period 1911-2005 and significant at the 95% confidence level

While the reanalysis displays a snow depth increase especially over the Tibetan Plateau and Western Himalaya, the GCMs show more stable snow depth conditions, except for some scattered areas. The MRI-CGCM3 model identifies a positive trend in the HKK region and CESM1-BGC

produces a negative trend in the western Himalaya.

Absolute validation of GCM results against "ground truth" remains a challenge in such orographically complex areas, owing to the insufficient availability of surface observations. This consideration, together with the remarkable inter-model variability detected here, should be taken into account when applying the snow output of a single GCM for hydrological modeling or impact studies of climate change.

4.3.3 Circulation patterns and the NAO-precipitation relationship in the HKK

Winter precipitation in the Hindu-Kush Karakoram (HKK) is generated by westerly perturbations (Western Weather Patterns, WWPs) originating from the Mediterranean/north Atlantic region. The dynamics of these mid-latitude perturbations is affected by the North Atlantic Oscillation (NAO) in such a way that larger precipitation in HKK is typically recorded during the positive NAO phase. This can be clearly seen in Fig. 4.10, where the correlation coefficients between a NAO index and winter precipitation from three observation-based gridded datasets and the ERA40 reanalyses are shown. We found that the link between NAO and winter precipitation in the HKK is not simply due to the propagation of westerly perturbations but it is the product of a complex synoptic pattern of moisture transport and evaporation from low-latitude seas. To identify the main sources of moisture for the HKK precipitation, we analyzed the links between evaporation, tropospheric winds, sea surface temperatures, precipitable water and the NAO index over an area extending approximately from the Mediterranean to the Indian subcontinent: these relationships are shown in Fig. 4.11. The results indicate that the most important moisture sources are localized in the Persian Gulf, the northern Arabian Sea and the Red Sea. Enhanced moisture transport from these reservoirs to the HKK region occurs during the positive NAO phase, through a mechanism that involves NAO-induced changes in evaporation and tropospheric circulation. The enhanced humidity over northern Pakistan and northern India during the positive NAO phase is picked up by the WWPs coming from the Mediterranean, leading to significant precipitation as these systems reach the HKK mountain slopes.

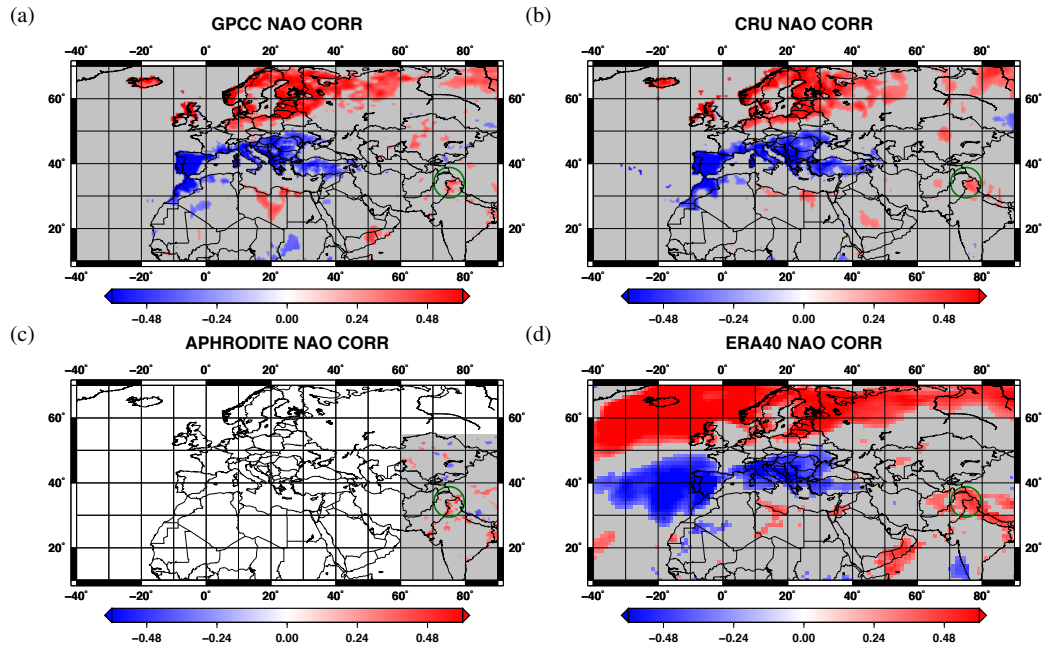

Figure 4.10: Correlation coefficients between NAOI and winter precipitation from (a) GPCC, (b) CRU, (c) APHRODITE and (d) ERA40. Colors indicate statistically-significant correlations at the 95 percent confidence level. Non-significant correlations are marked in gray. The green circle highlights the area of positive correlation centered on HKK.

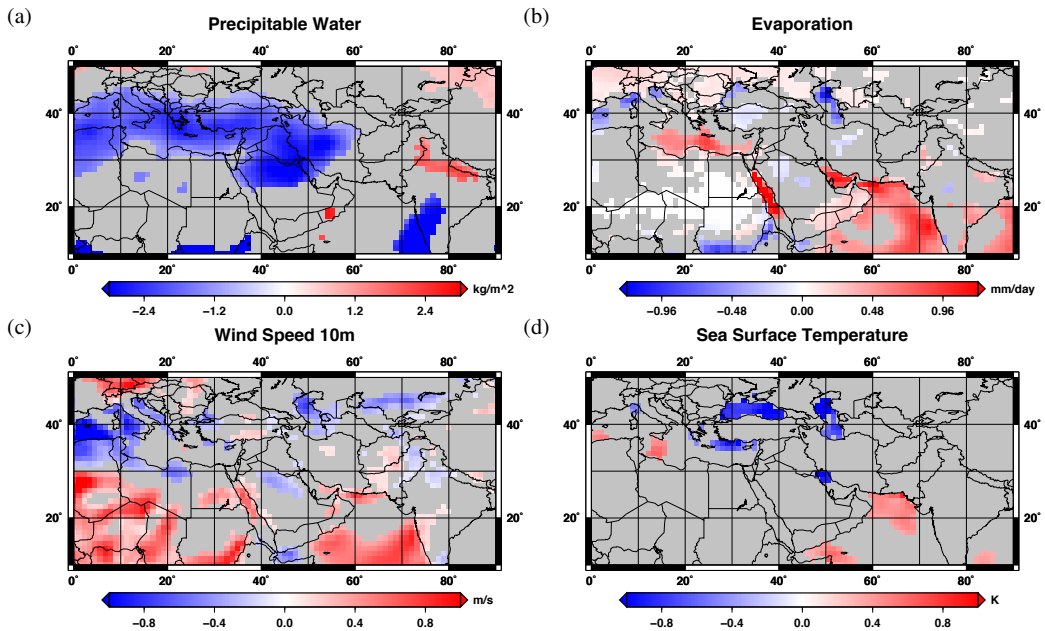

Figure 4.11: Difference between the positive and the negative NAO composites of (a) precipitable water, (b) evaporation, (c) 10m wind speed and (d) sea surface temperature. Colors indicate statistically significant values at the 95 percent confidence level; gray indicates non-significant values.

4.3.4 Aerosol and climate in the Himalayas

4.3.4.1 Global simulations with ECHAM-HAM

We used a coupled aerosol-atmosphere-ocean model ECHAM 5.4+HAM1+OPA 8.2+LIM2 to analyze the relationship between aerosol and the Asian summer monsoon. Experiments were performed starting from a 80 years long spinup at constant forcing typical for the year 2000, following the CMIP5 protocol for forcing data. The forcings include the concentrations of well-mixed green-house gases and incoming solar irradiance; the seasonally varying ozone distribution is repeated every year and is based on the 2000-year climatology. For aerosols, the emission dataset is based on the AeroCom aerosol model inter-comparison project inventories for the year 2000 (*Dentener et al., 2006).* The model climatology is compared with data from the ERA40 global atmospheric reanalysis product and with the Global Precipitation Climatology Project (GPCP) gridded rainfall observational product.

To analyze large scale spatial variations of the Indian monsoon with the loading of absorbing aerosols, we define a monthly mean aerosol index as in *Lau et al. (2006)* is developed averaging model ABS over the region (70°-90°E, 20-30°N) in the pre-monsoon season April-May, and by considering the anomaly of the resulting time-series with respect to its mean. From this index we select strong (weak) years of aerosol loading corresponding to years with an amount of absorbing aerosols larger (smaller) than 1 standard deviation and these years are used to build composites of strong minus weak years of precipitation, temperature and wind fields during the monsoon season (see fig. 4.12).

Results show that when increased aerosol loading is found on the Himalayas slopes in the pre-monsoon period (April-May), intensification of early monsoon rainfall over India and increased low-level westerly flow follow, in agreement with the Elevated-Heat-Pump (EHP) mechanism (*Lau et al., 2006*). The increase in rainfall and cloudiness during the early monsoon has a cooling effect on the land surface. We find that enhanced surface cooling is also produced through the solar dimming by the presence of more dust from the deserts brought by an increased low-level westerly flow in the early monsoon season.

The surface cooling causes subsequent reduction in monsoon rainfall over India, with a beginning of this decrease in northern India. An observed time-lagged and reasonably realistic response to aerosol forcing suggests that absorbing aerosols, besides their potential key roles in impacting monsoon water cycle and climate, may be considered as a possible source of seasonal predictability of the Asian summer monsoon over the Indian subcontinent.

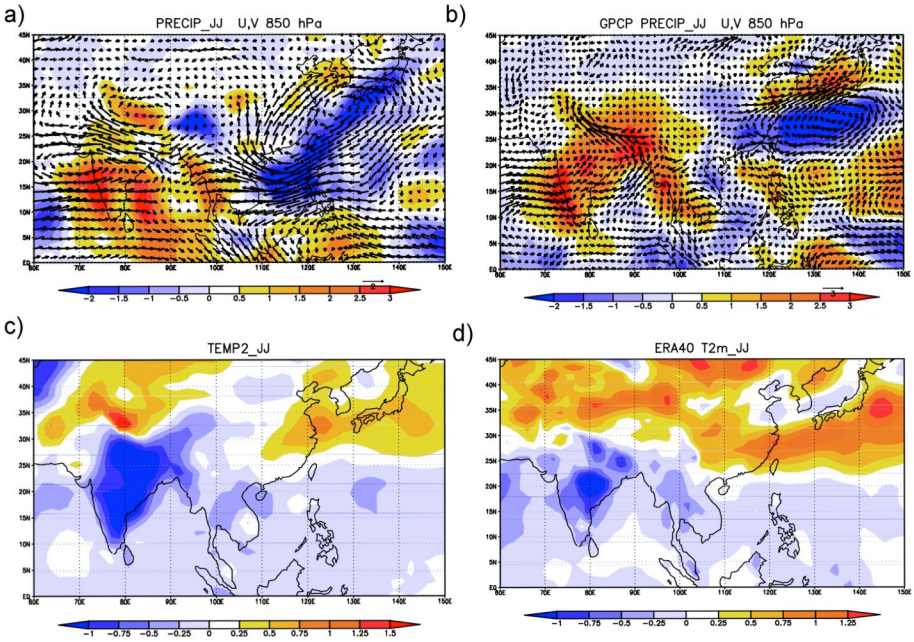

Figure 4.12: June-July composite of rainfall (mm day^{-1}) and 850 hPa wind pattern (m sec^{-1}) for the model and b) the observed rainfall anomalies GPCP and 850hPa ERA40 winds; c) June-July two metre temperature (K) anomaly composite for the model and d) the two metre temperature observed. For ERA40 and GPCP observations, the weak years (1982, 1983, 1990, 1992) and the strong years (1980, 1985, 1988, 1991) were selected, following *Lau et al.* [2006].

4.3.4.2 Hydrostatic regional simulations with the RegCM4 model

In the context of PAPRIKA we used the regional climate model RegCM4 to evaluate the regional climatic impact of aerosol in the HKKH region and to perform a climate change experiment aiming at analyzing future climatic condition over the PAPRIKA domain (see report on WP5 for a discussion on regional projections), including the aerosol component. In particular, we have studied the climate response to aerosol forcing (considering only direct and semi-direct effects) at high resolution (50km) using the ICTP RegCM4 regional model. Complementarily to the GCM approach also adopted in PAPRIKA, the expected added values of RegCM4 lie in a more accurate description of aerosol and associated forcing, as well as a better resolution of the aerosol climatic signal, notably over the Karakoram-Himalayan region. As a first step in our model analysis we validated the model against satellite observations in terms of Aerosol Optical Depth (AOD at 550 nm) and vertical distribution of aerosol optical properties (aerosol extinction and effective single scattering albedo, SSA). As for the AOD, for example, we found that RegCM4 reproduces quite well the main patterns of the observed AOD, especially in the dust-dominated regions (Arabian sea, Pakistan maxima, Gobi desert). A number of deficiencies pointed out by *Nair et al. (2012)* relative to soil texture/sand blasting and emission size distribution characteristics have been fixed in the PAPRIKA simulations, resulting in an improved representation of dust aerosol AOD. As for the anthropogenically polluted regions, the model reproduces reasonably well the magnitude and patterns of AOD over China. In the Eastern Indo-gangetic, Bangladesh and Bengal gulf regions,

there is a clear underestimation of the model with respect to the observations. This could be also attributed to uncertainties in the emission inventories.
To evaluate the impact of aerosols on precipitation in the HKKH region, we run RegCM4 with and without aerosol and analyzed the model output over the HKKH region in terms of precipitation amounts, time series and historical trends. Figure 4.13, for example, shows the monthly time series of the simulated and observed precipitation, averaged over a box encompassing the whole Himalayan region. We used the TRMM and APHRODITE precipitation products already used in *Palazzi et al. (2013)* and the results of the two simulations with and without aerosols are plotted.
The model tends to overestimate precipitation over the HKKH region, especially in winter, compared to the observations; adding the aerosol results in a significant reduction of the precipitation bias. The improvement of simulated precipitation field is more effective in summer than winter: aerosols tend to reduce the simulated precipitation of about 14% on average over the monsoon and pre-monsoon season compared to the simulation without aerosols.

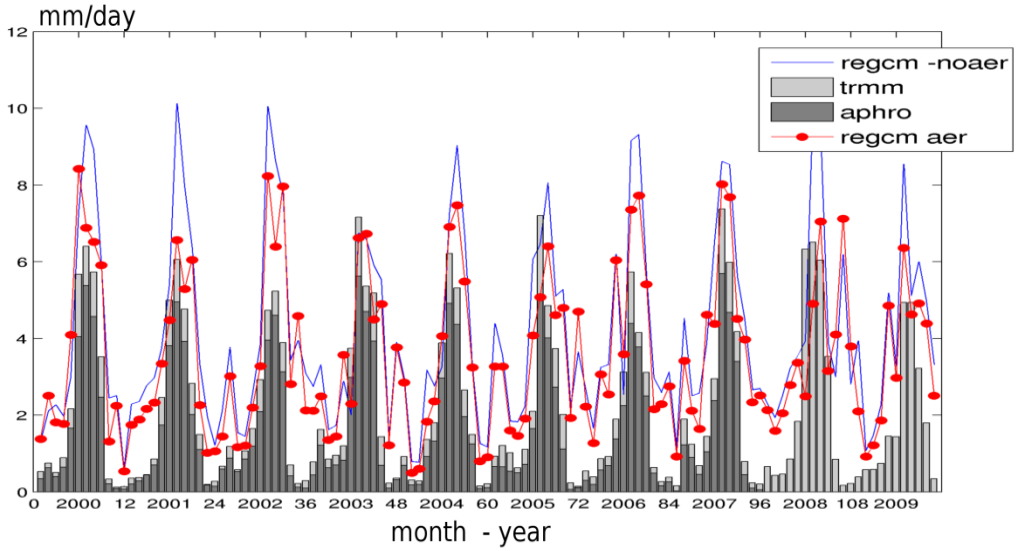

Figure 4.13: Monthly time series of simulated (lines) and observed (bars) precipitation over the HKKH region. See the legend for details.

4.3.4.3 Aerosol variability and atmospheric transport in the Himalayan region inferred from satellite data and back-trajectories

The Himalayan Plateau is surrounded by regions with high natural and anthropogenic aerosol emissions having a strong impact on regional climate. This is particularly critical for the Himalayan glaciers whose equilibrium is also largely influenced by the radiative effects induced by aerosol burden. In the framework of PAPRIKA we have focused on the spatial and vertical distribution of different aerosol types, their seasonal variability and sources. The analysis of the 2007-2010 yr of CALIPSO vertically resolved satellite data allowed the identification of spatial patterns of desert dust and carbonaceous particles in different atmospheric layers. Clusters of Lagrangian back-trajectories highlighted the transport pathways from source regions during the dusty spring season. The analysis showed a prevalence of dust; at low heights they are distributed mainly north (with a main contribution from the Gobi and Taklamakan deserts) and west of the Tibetan Plateau (originating from the deserts of South-West Asia and advected by the westerlies). Above the Himalayas the dust amount is minor but still not negligible (detectable in around 20 % of the measurements), and transport from more distant deserts (Sahara and Arabian Peninsula) is important. Smoke aerosol, produced mainly in North India and East China, is subject to shorter range transport and is indeed observed closer to the sources while there is a limited amount reaching the top of the plateau. Data analysis has revealed a clear seasonal variability in the

frequencies of occurrence for the main aerosol types, as shown in Fig. 4.14; dust is regulated principally by the monsoon dynamics, with maxima of occurrence in spring. Relevant interannual differences also emerged from our study, showing a larger presence of aerosol in the region during 2007 and 2008 yr. The developed database is currently applied to model evaluation studies.

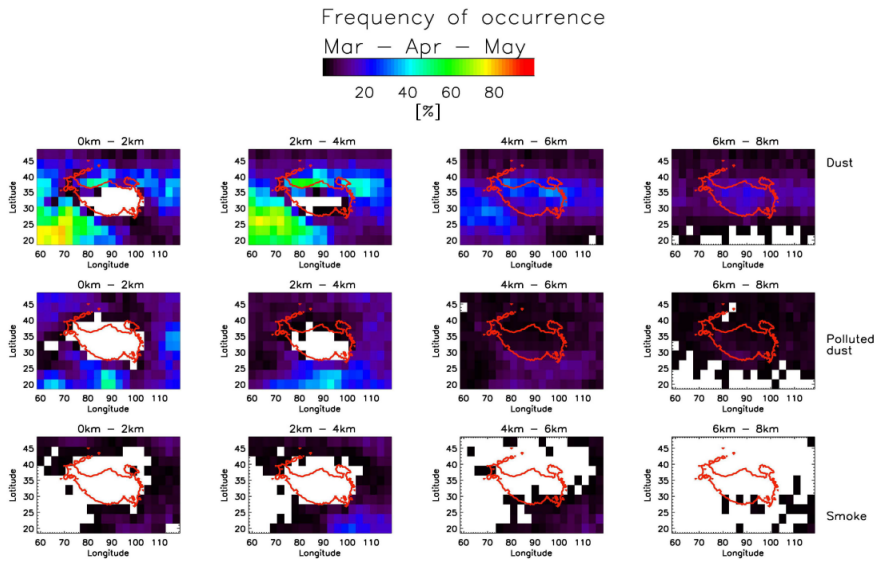

Figure 4.14: Aerosol frequency of occurrence for the MAM season. Different aerosol types (dust, polluted dust, smoke) are reported from top to bottom. Different vertical layers are reported from left to right.

Key reference: Bucci, S., Cagnazzo, C., Cairo, F., Di Liberto, L., and Fierli, F.: Aerosol variability and atmospheric transport in the Himalayan region from CALIOP 2007–2010 observations, Atmos. Chem. Phys. Discuss., 13, 15271-15299, doi:10.5194/acpd-13-15271-2013, 2013.

4.3.5 Non-hydrostatic high-resolution simulation of extreme events with WRF

Estimating current and future water resources in high mountain regions with complex orography is a difficult but crucial task. The ability of having a good precipitation estimate (QPE) at a fine resolution is the starting point to address this important scientific question. In this framework, we have explored the predictive ability of the WRF (Weather Research Forecast) model, operated at very fine-resolution, in reproducing extreme hydro-meteorological phenomena over the most complex topography region of HKKH. In the framework of PAPRIKA we have focused on the 2010 Pakistan floods which began in late July 2010, producing heavy monsoon rains in the Khyber Pakhtunkhwa, Sindh, Punjab and Balochistan regions of Pakistan and affecting the Indus River basin. Approximately one-fifth of Pakistan's total land area was underwater, with a death toll of about 2000 people. This event has been simulated with the WRF model (v3.3) in cloud-permitting mode (d01 14 km and d02 3.5 km) for the period July 26-30, 2010: different convective closures (explicit and KF) and microphysics parameterizations (WSM6 and Thompson) have been used (see Fig. 4.15). A deeper understanding of the processes responsible for this event has been gained through comparison of the model outputs with rainfall depth observations, radiosounding data, geostationary/polar satellite images and cloudsat observations. The impact of the different day of initialization on the output simulation is also examined, as shown in Fig. 4.16.

Our study demonstrates that the quality of the initial conditions were a prominent factor to retrieve a satisfying representation of the event. WRF capacity to reproduce clouds and precipitation processes at the fine scale was almost satisfying even if more experiment are needed to use the WRF model as a dynamic “downscaler” over an area with a so complex topography.

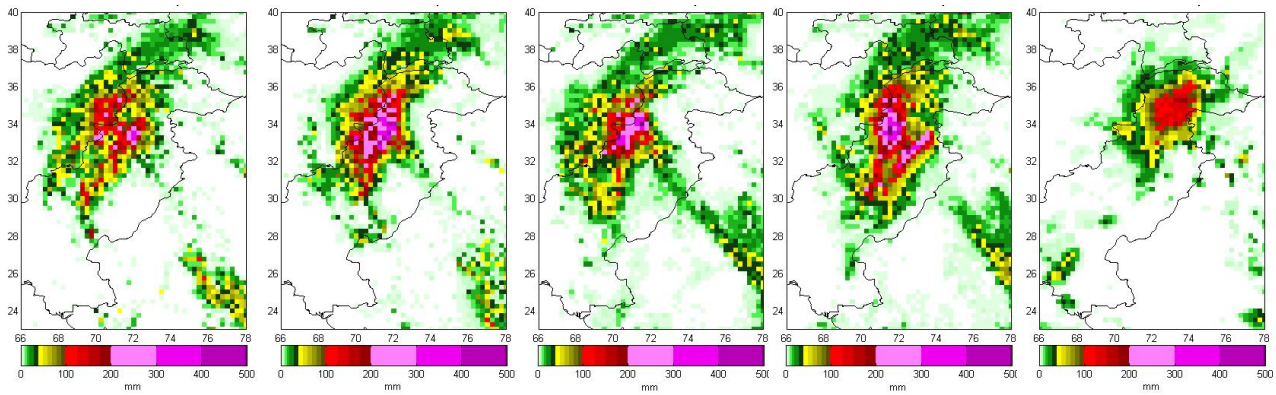

Figure 4.15: Comparison between WRF configurations in terms of QPE (left panels, from left to right: Explicit convection WMS6 microphysic scheme, Explicit convection Thompson microphysic scheme, Kain- Fritsch convection WMS6 microphysic scheme, Kain- Fritsch convection Thompson microphysic scheme) and TRMM daily rainfall (right panel). All the rainfall fields are here presented at 0.25° horizontal resolution.

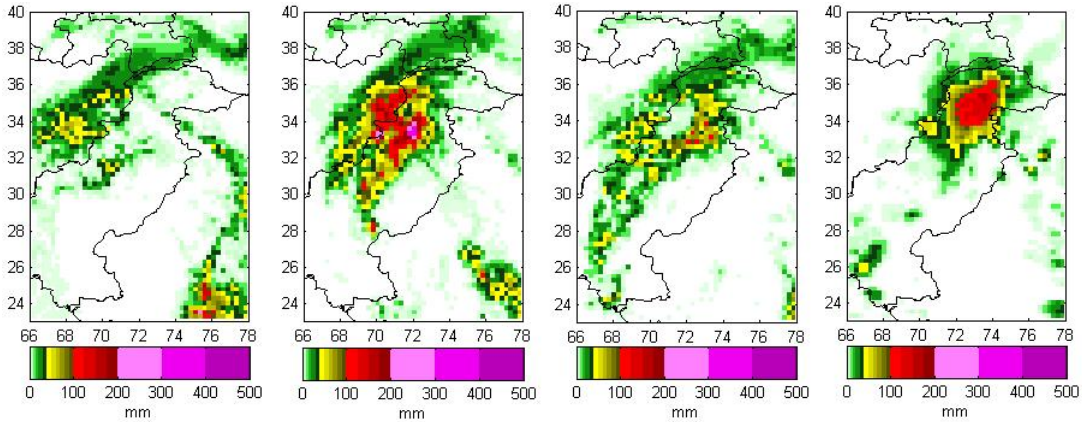

Figure 4.16: Comparison between WRF QPE for different days of initialization (left panels, from left to right: July 24th initialization, July 26th initialization and July 28th initialization) and TRMM daily rainfall (right panel) at 0.25° resolution in the study area, on July 29th 2010.

4.3.6 Stochastic rainfall downscaling of satellite data in poorly gauged regions

In the framework of PAPRIKA, we applied the RainFARM stochastic downscaling procedure to satellite precipitation data (TRMM, ~25km resolution) over the Karakoram area (Northern Pakistan) to obtain new precipitation fields at ~1km resolution. Figure 4.16 shows, as an example of a rainfall downscaling for the day 30/04/2010, one original TRMM field at 25 km resolution (panel a) and the downscaled TRMM field at 1 km resolution (panel b), obtained after applying RainFARM to the satellite precipitation data. It is clear from this snapshot that the employed method is able to add small-scale variability at the scale not resolved by the original TRMM data (i.e., below 25 km), but preserving the large scale properties of the original field (for example, the total rainfall volume and amount into each original TRMM pixel).

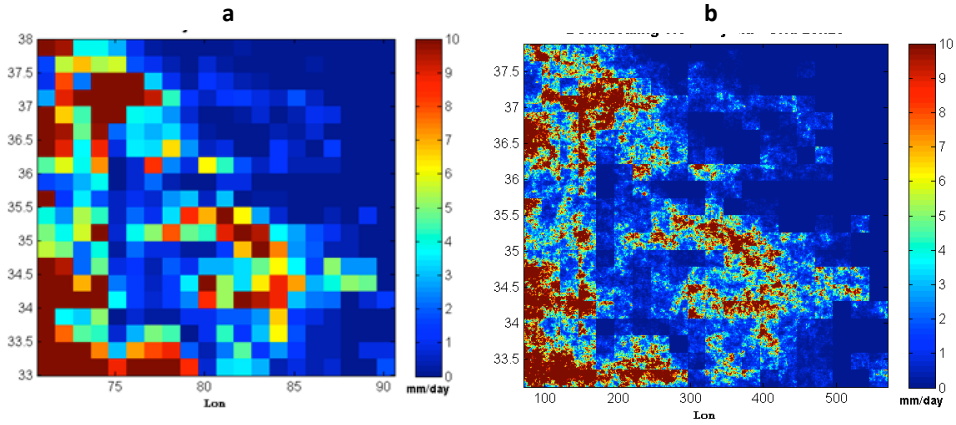

Figure 4.17: Example of daily precipitation map (April 30, 2010) from TRMM: a) original data and b) downscaled data

We compared the statistical properties (such as the shape of the precipitation power spectrum and probability density functions, PDFs) of the downscaled TRMM precipitation fields with the few observations available for this area, essentially provided by the Pakistani meteorological Department (PMD) and the Water and Power Development Authority (WAPDA). We performed our analysis on a seasonal basis and focusing on the time periods 1998-2012. In Fig. 4.18 we show, as an example, the probability density function of the winter (DJFM) precipitation intensity from the original (blue line) and downscaled TRMM (red line) precipitation, and from an ensemble of seven rain gauge stations located in Northern Pakistan and managed by the PMD. The figure shows that the downscaled TRMM precipitation PDFs agree better with the station-based observed precipitation PDFs than the precipitation PDFs from the original TRMM data, in terms of amplitude distribution and capability of represent the precipitation extremes.

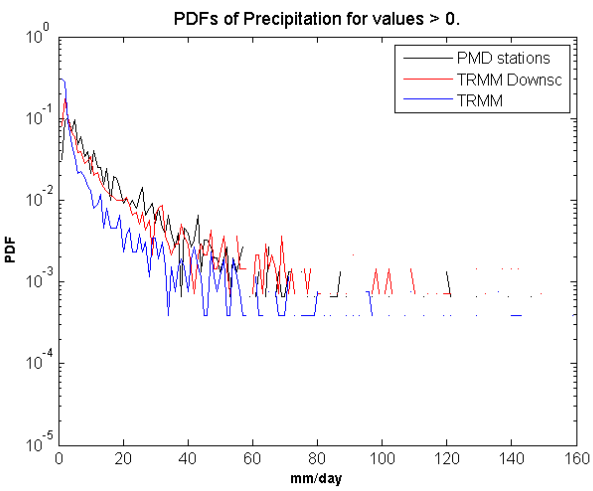

Figure 4.18: PDF of DJFM precipitation from all PMD station in Northern Pakistan (black), TRMM (blue), and downscaled TRMM (red).

For ungauged or poorly-gauged regions, therefore, a stochastic rainfall downscaling method like RainFARM applied to coarse-scale observations (for example, to satellite measurements) is an effective mean to obtain reliable, high-resolution synthetic precipitation fields.

4.3.7 Hydrological model performance

We ran a 33-years long simulation with the glacio-hydrological model, obtaining daily estimations of in channel discharge at Shigar bridge. We compared the results with the average of monthly

mean discharges during 1985-1997, and with the 2012 daily discharge data from our installed station. We evaluated the performance of the model in providing acceptable depiction of i) ice flow velocities against those estimated from the available literature (2003-2008), ii) average monthly flows against those provided by the WAPDA hydrometric station in Shigar (1985-1997), and iii) daily flows against those estimated during 2012 using data from our hydrometric station in Shigar, validated during May-November. The modeled ice flow velocity has its maximum at Concordia and the mean velocity estimated based upon remote sensing images during 2003-2008 is 107 my^{-1} (*Quincey et al., 2011*), while that estimated by the model is 99 my^{-1}. The spatial pattern of ice velocity seems generally visually consistent between the model (as per altitude belts), and the satellite estimates, particularly on the main body of the glacier, indicating an acceptable performance of the ice flow model.

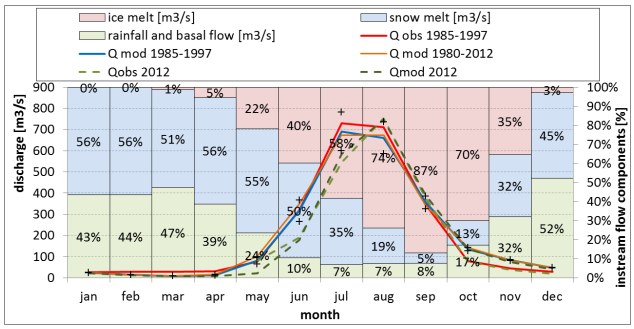

Figure 4.19: monthly calibration 1985-1997

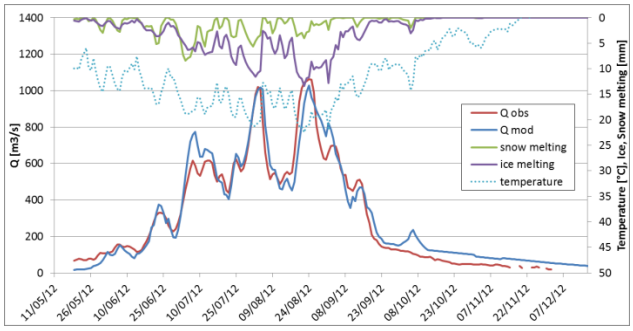

Figure 4.20: daily calibration 2012

The model estimates a mean annual discharge value of 203m^3s^{-1} during 1985-1997, against an observed value of 202m^3s^{-1} (*bias* = -0.79%). In Figure 4.19 we report modeled monthly mean discharges, during 1985-1997, against their observed counterparts (Archer, 2003), and display the contribution to flow of three components, namely rainfall (plus base flow), ice melt, snow melt, as estimated by the model on average during 1985-1997. Clearly, snow melting carries half of the total discharge until May, and then moves to a lower share in favor of ice melting, which in August and September represents a very large share of total instream flow.

Comparing daily discharges from the model during May-November 2012 against observations (Fig. 4.20), we obtained a Nash Suthcliffe Efficiency *NSE* = 0.94, and a random mean square error *RMSE* = 69.2 m^3s^{-1}, with a "good" level of agreement. We also try to compare the snow accumulation from two snow pits taken in August 2011 and the accumulation coming from the model finding an error less than 8% on the last three years accumulation.

References

Arakawa, A., (2004), The Cumulus Parameterization Problem: Past, Present, and Future. J. Climate, 17, 2493–2525. doi: http://dx.doi.org/10.1175/1520-0442(2004)017<2493:RATCPP>2.0.CO;2

Bocchiola, D., Diolaiuti, G., Soncini, A., Mihalcea, C., D'Agata, C., Mayer, C., Lambrecht, A., Rosso, R., Smiraglia, C., 2011. Prediction of future hydrological regimes in poorly gauged high altitude basins: the case study of the upper Indus, Pakistan, Hydrol. Earth Syst. Sci., 15, 2059-2075, 2011.

Dentener, F., S. Kinne, T. Bond, O. Boucher, J. Cofala, S. Gen- eroso, P. Ginoux, S. Gong, J. Hoelzemann, A. Ito, L. Marelli, J. Penner, J.-P. Putaud, C. Textor, M. Schulz, G.v.d. Werf, and J. Wilson: Emissions of primary aerosol and precursor gases in the years 2000 and 1750 -prescribed data-sets for AeroCom, Atmos. Chem. Phys., 6, 4321–4344, 2006

D'Onofrio, D., Palazzi, E., von Hardenberg, J., Provenzale, A. and Calmanti, S.: Stochastic rainfall downscaling of climate models, Journal of Hydrometeorology, doi: 10.1175/JHM-D-13-096.1, 2014

Groppelli, B., Soncini, A., Bocchiola, D. and Rosso, R., 2011. Evaluation of future hydrological cycle under climate change scenarios in a mesoscale Alpine watershed of Italy, Nat. Haz. Earth Sys. Scie., 11, 1769-1785.

Hazeleger, W., et al. (2012), EC-Earth v2.2: description and validation of a new seamless earth system prediction model, Clim. Dynam., pp. 1–19, doi:10.1007/s00382-011-1228-5.

Hong, S. Y., Noh, Y., & Dudhia, J. (2006), A new vertical diffusion package with an explicit treatment of entrainment processes, Monthly Weather Review, 134(9), 2318-2341

Lau, K. M., M. K. Kim, and K. M. Kim (2006), Asian monsoon anomalies induced by aerosol direct effects, Clim. Dyn., 26, 855– 864, doi:10.1007/s00382-006-0114-z.

Lamarque, J.-F., Bond, T. C., Eyring, V., Granier, C., Heil, A., Klimont, Z., Lee, D., Liousse, C., Mieville, A., Owen, B., Schultz, M. G., Shindell, D., Smith, S. J., Stehfest, E., Van Aardenne, J., Cooper, O. R., Kainuma, M., Mahowald, N., Mc- Connell, J. R., Naik, V., Riahi, K., and van Vuuren, D. P.: Historical (18502000) gridded anthropogenic and biomass burning emissions of reactive gases and aerosols: methodology and application, Atmos. Chem. Phys., 10, 7017-7039, 2010.

Lohmann, U. and Hoose, C.: Sensitivity studies of different aerosol indirect effects in mixed-phase clouds, Atmos. Chem. Phys., 9, 8917–8934, 2009

Madec, G., P. Delecluse, I. Imbard and C . Levy (1999): OPA 8.1 Ocean General Circulation Model reference manual. Note du Pôle de modélisation No. 11, Inst. Pierre-Simon Laplace (IPSL), France, 91 pp.

Masson D, Knutti R (2011) Climate model genealogy. Geophysical Research Let- ters 38, DOI 10.1029/2011GL046864

Meehl GA, Washington WM, Arblaster JM, Hu A, Teng H, Tebaldi C, Strand WG, III JBW (2012) Climate system response to external forcings and climate change projections in ccsm4. J Climate 25:3661–3683, DOI 10.1175/JCLI-D-11-00240.1

Moss, R. H., et al. (2010), The next generation of scenarios for climate change research and assessment, Nature, 463(7282), 747–756, doi:10.1038/nature08823.

Nair, V. S., F. Solmon, F. Giorgi, L. Mariotti, S. S. Babu, and K. K. Moorthy (2012), Simulation of South Asian aerosols for regional climate studies, J. Geophys. Res., 117, D04209, doi:10.1029/2011JD016711.

Oerlemans, J., 1997. Climate sensitivity of Franz Josef Glacier, New Zeland, as Revealed by NumericalModeling. Artic and Alpine Research, Vol. 29, No. 2, 1997, pp 233-239.

Oerlemans, J., 2001. Glaciers and climate change, 148 pp., A. A. Balkema Publishers, Brookfield, Vt.
Wallinga, J., van de Wal, R.S.W., 1998. Sensitivity of Rhonegletscher, Switzerland, to climate change:experiments with a one-dimensional flowline model. Journal of Glaciology, 44(147), 383-393.

Ohara, T., Akimoto, H., Kurokawa, J., Horii, N., Yamaji, K., Yan, X., and Hayasaka, T.: An Asian emission inventory of an-thropogenic emission sources for the period 1980–2020, Atmos. Chem. Phys., 7, 4419–4444, 2007.

Palazzi E, von Hardenberg J, Provenzale A (2013) Precipitation in the hindu- kush karakoram himalaya: Observations and future scenarios. J Geophys Res 118:85–100, DOI 10.1029/2012JD018697

Quincey, D.J., Glasser N.F., Braun, M., Bishop, M.P., Hewitt, K. and Luckman, A., 2011. Karakoram glacier surge dynamics, Geophysical Research Letters, 38, doi: 10.1029/2011GL049004.

Rebora, N., L. Ferraris, J. von Hardenberg, and A. Provenzale, 2006: RainFARM: Rainfall downscaling by a Filtered AutoRegressive Model. J. Hydrometeor., 7, 724–738.

Roeckner, E., Baeuml, G., Bonaventura, L., Brokopf, R., Esch, M., Giorgetta, M., Hagemann, S., Kirchner, I., Kornblueh, L., Manzini, E., Rhodin, A., Schlese, U., Schulzweida, U. and Tompkins, A.: The atmosphere general circulation model ECHAM5. PART I: Model description, Report 349, Max Planck Institute for Meteorology, Hamburg, Germany, available from http://www.mpimet.mpg.de, 2003.

Su F, Duan X, Chen D, Hao Z, Cuo L (2012) Evaluation of the global climate models in the cmip5 over the tibetan plateau. J Climate 26:3187–3208, DOI 10.1175/JCLI-D-12-00321.1

Taylor KE, Stouffer RJ, Meehl GA (2012) An overview of cmip5 and the ex- periment design. Bull Amer Meteor Soc

93:485–498, DOI http://dx.doi.org/10. 1175/BAMS-D-11-00094.1

Timmermann, R., H. Goosse, G. Madec, T. Fichefet, C. Ethé, and V. Dulière (2005): On the representation of high latitude processes in the ORCA-LIM global coupled sea ice ocean model, Oc. Model., 8, 175-201.

van der Werf, G. R., Randerson, J. T., Giglio, L., Collatz, G. J., Mu, M., Kasibhatla, P. S., Morton, D. C., DeFries, R. S., Jin, Y., and van Leeuwen, T. T.: Global fire emissions and the contribu- tion of deforestation, savanna, forest, agricultural, and peat fires (19972009), Atmos. Chem. Phys., 10, 11707–11735, 2010.

Vignati, E., Wilson, J. and Stier, P.: M7: An efficient size-resolved aerosol microphysics module for large-scale aerosol transport models, J. Geophys. Res., 109, D22202, 2004

Wilcox LJ, Highwood EJ, Dunstone NJ (2013) The influence of anthropogenic aerosol on multi-decadal variations of historical global climate. Environ Res Lett 8, DOI 10.1088/1748-9326/8/2/024033

WP5: Future scenarios on water availability

Elisa Palazzi, Jost von Hardenberg, Silvia Terzago, Antonello Provenzale (ISAC-CNR)

Fabien Solmon, Filippo Giorgi (ICTP)

Daniele Bocchiola and co-workers (POLIMI)

5.1. Introduction

This report focuses on the climate projections developed during the project for the Karakoram and Himalaya regions. Precipitation and snow depth projections provided by the state-of-the art GCMs participating in the CMIP5 effort, are presented and discussed. Future hydrological scenarios obtained by using the glacio-hydrological model developed during the project driven by the climatic input derived from the GCM projections are also discussed.

5.2. GCM climate projections

5.2.1 Simulation of the future precipitation in the HKKH region

Daily precipitation data from the EC-Earth model (see the WP4 chapter for a model description) have been used for analyzing projections of summer and winter precipitation in the HKK and Himalaya regions in the two emission scenarios RCP 4.5 and RCP 8.5. We have extended the individual EC-Earth simulation discussed in the WP4 chapter and considered an ensemble of independent realizations created, under the same forcing conditions, by the participants in the EC-Earth consortium. Figure 5.1 shows the time series of precipitation (after filtering with a 5 years running mean) from the resulting eight-member ensemble in the period 1850-2100 (*Palazzi et al., 2013*).

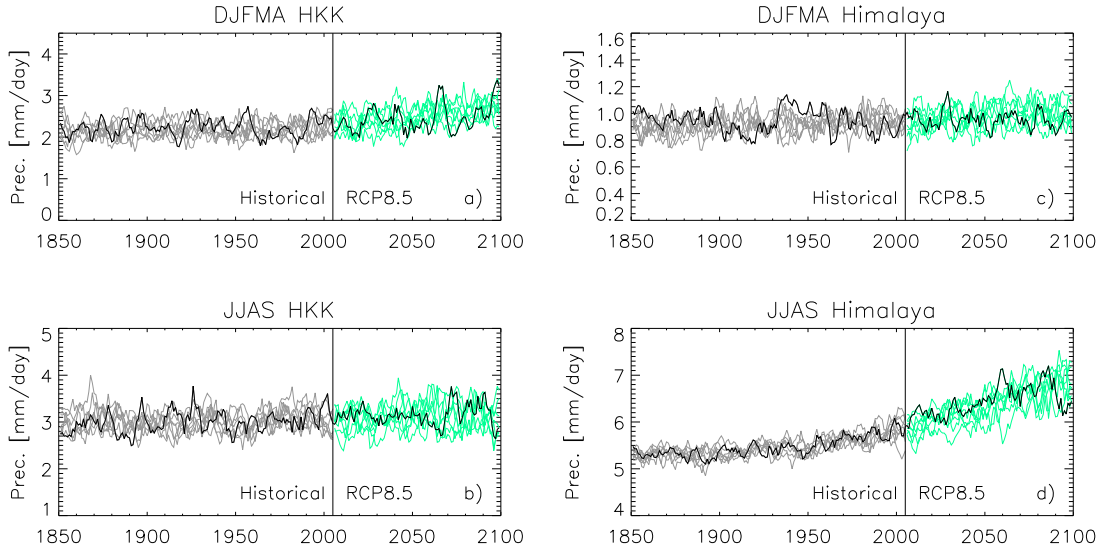

Figure 5.1: Time series of precipitation over (a and b) HKK and (c and d) the Himalaya domain during DJFMA (a and c) and JJAS (b and d) from the eight realizations of the EC-Earth model ensemble for the period (1850–2100) in the RCP 8.5 scenario (for 2006-2100). The individual member of the EC-Earth ensemble run at ISAC-CNR is indicated with a thick black line. The time series have been filtered with a 5 years running mean.

The most extreme RCP 8.5 scenario for the period 2006-2100 is shown in the figure (the results obtained under the intermediate RCP 4.5 scenario are discussed but not shown for brevity). In order to highlight the interannual variability of the model precipitation, we report the EC-Earth simulation run at ISAC-CNR with a thick black line.

In Himalaya during summer the EC-Earth model members indicate an increasing trend in precipitation under the most extreme RCP 8.5 scenario (Fig. 5.1d), corresponding to an increase of about 0.008 to 0.014 mm/d/yr. In the RCP 4.5 scenario the increasing precipitation trend continues till about 2050, when it stabilizes and a slight decrease starts, giving rise to no statistically significant trend in summer precipitation. In the Himalaya during winter, one out of eight EC-Earth members provides a statistically significant increase in precipitation in the RCP 4.5 scenario, and another member shows a trend in future precipitation in the RCP 8.5 scenario. Three (five) out of eight EC-Earth members give a statistically significant increasing trend in winter precipitation in the HKK of about 0.3 to 0.4 (0.4 to 0.7) mm/d/(95 years) under the RCP 4.5 (RCP 8.5) scenario. No statistically significant precipitation trend is found during summer in the HKK in the RCP 4.5 scenario, while in the RCP 8.5 scenario, two members give an increase in summer precipitation of about 0.5 mm/d/(95 years).

Also for the analysis of future precipitation projections, we have extended the model study performed with EC-Earth to the 32 CMIP5 models already employed for the investigation of the historical precipitation climatology (WP4 chapter). Figure 5.2 shows the seasonal time series of the precipitation anomalies from 1870 to 2100 in the Himalayan and HKK regions. The anomaly is evaluated relative to the average precipitation in the baseline period (1901-2005). The individual GCM outputs are shown with the grey area, the multi-model mean (MMM) with the black solid line (historical period), and with blue (RCP 4.5) and red (RCP 8.5) thick lines. The CRU and GPCC precipitation anomalies are shown with the pink and green lines, respectively.

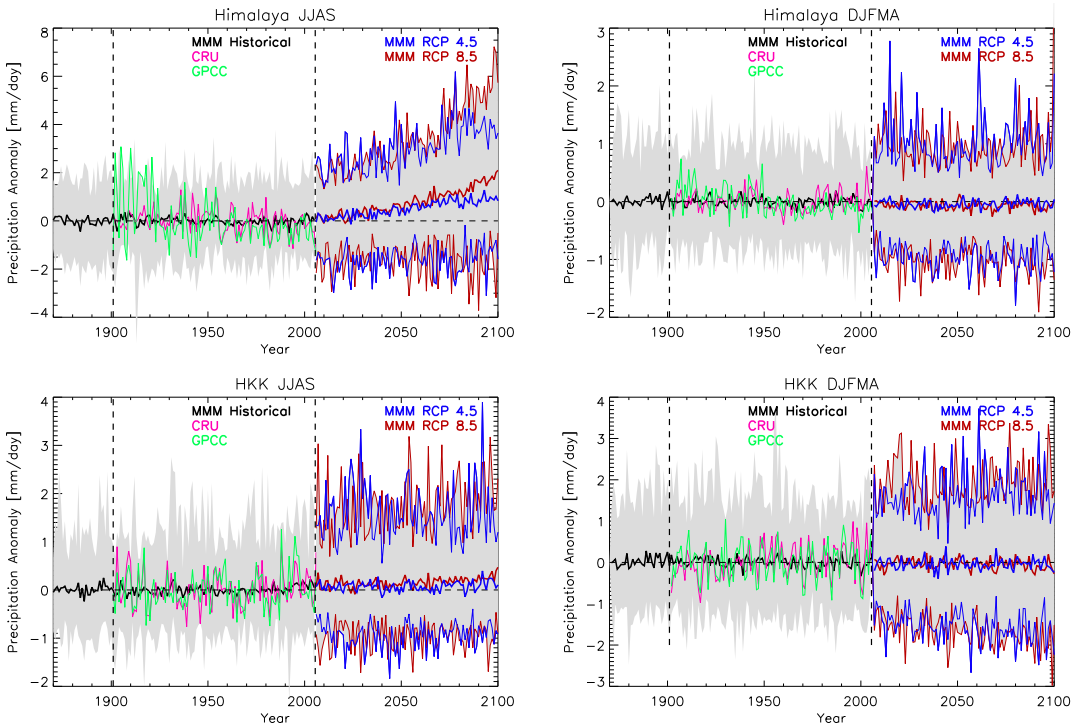

Figure 5.2: Time series of precipitation anomalies in the Himalaya (top) and in the HKK (bottom) during summer (left) and winter (right) from 1870 to 2005 and from 2600 to 2100. The top and bottom bounds of the shaded grey area are the maximum and minimum of the annual value from the 32 GCM simulations. The multi-model mean (MMM) is shown with the black (historical period), blue (RCP 4.5 scenario) and red (RCP 8.5 scenario) solid lines. CRU and GPCC observations are shown with the pink and green lines, respectively. The anomalies are evaluated with respect to the 1901-2005 baseline period.

We show the future (2006-2100) trends of summer and winter precipitation (in mm/day/century) in

the Himalaya and HKK regions in Tables 5.1 and 5.2, respectively. The model precipitation trends in the historical period is also shown for completeness and compared to the trend inferred from the two observational data sets.

Table 5.1. Trends (in mm/day per century) in the Himalaya during JJAS and DJFMA, in the periods 1901-2005 and 2006-2100 (RCP4.5 and RCP8.5 scenarios) for the CMIP5 models and the MMM. Historical precipitation trends for the CRU and GPCC datasets are also indicated. Bold figures indicate statistically significant trends.

	JJAS			DJFMA		
	Historical 1901-2005	RCP4.5 2006-2100	RCP8.5 2006-2100	Historical 1901-2005	RCP4.5 2006-2100	RCP8.5 2006-2100
Observations						
CRU	**-0.369**			0.048		
GPCC	**-1.445**			**-0.355**		
CMIP5 models						
bcc-csm1-1-m	0.010	0.171	**0.827**	0.170	-0.131	-0.066
bcc-csm1-1	0.026	0.847	**2.076**	-0.015	0.391	**0.797**
CCSM4	0.283	0.507	**1.746**	-0.123	-0.084	-0.127
CESM1-BGC	-0.114	**0.837**	**1.866**	-0.042	-0.088	-0.193
*CESM1-CAM5	-0.395	**2.588**	**3.806**	0.020	0.033	0.135
EC-Earth	**0.516**	0.003	**1.082**	0.101	**0.162**	0.097
FIO-ESM	0.042	**-1.547**	-0.828	0.000	-0.099	-0.328
GFDL-ESM2G	0.164	**0.711**	**4.198**	0.101	-0.040	0.242
GFDL-ESM2M	-0.014	**1.445**	**2.534**	0.127	0.140	**0.299**
MPI-ESM-LR	-0.114	-0.356	0.183	-0.082	-0.188	-0.233
MPI-ESM-MR	0.464	0.153	-0.011	-0.262	-0.044	**-0.483**
***CanESM2**	**-1.009**	**1.553**	**2.214**	0.003	-0.012	**0.331**
CMCC-CMS	0.136	0.610	-0.035	0.047	**-0.484**	**-0.460**
CNRM-CM5	0.194	0.567	**1.769**	0.034	0.238	**0.462**
***CSIRO-Mk3-6-0**	-0.079	0.162	**0.785**	-0.084	**0.165**	0.129
***GFDL-CM3**	**-0.799**	**4.873**	**6.583**	0.134	0.022	-0.182
INM-CM4	0.073	**0.758**	**1.874**	-0.036	0.054	**-0.238**
IPSL-CM5A-LR	-0.088	**0.860**	**1.021**	-0.215	0.135	**-0.641**
IPSL-CM5A-MR	0.039	**1.498**	**2.603**	-0.031	0.069	-0.310
IPSL-CM5B-LR	-0.133	**1.042**	**1.602**	-0.012	0.172	0.315
***MRI-CGCM3**	0.031	-0.265	0.330	-0.123	-0.022	0.215
CMCC-CM	-0.161	0.239	**0.956**	0.161	-0.212	**-0.524**
FGOALS-g2	**0.313**	**0.914**	**2.215**	0.190	**-0.261**	**-0.351**
***HadGEM2-AO**	**-0.436**	**1.228**	**1.129**	**-0.150**	0.061	-0.051
***ACCESS1-0**	**-0.476**	**0.699**	**1.150**	-0.105	-0.063	**-0.183**
***ACCESS1-3**	**-0.537**	**1.953**	**2.996**	0.076	-0.017	-0.071
***HadGEM2-CC**	**-0.746**	**1.662**	**1.507**	-0.086	**0.227**	-0.076
***HadGEM2-ES**	**-0.445**	**1.356**	**1.295**	**-0.189**	0.012	-0.091
***MIROC5**	**0.585**	**2.210**	**3.769**	-0.064	0.062	**0.292**
***MIROC-ESM**	0.358	**1.620**	**2.432**	-0.239	0.266	-0.036
***NorESM1-M**	-0.045	**1.838**	**2.469**	0.103	0.053	-0.110
***NorESM1-ME**	-0.075	**1.976**	**2.295**	0.230	-0.017	-0.182
MMM	-0.076	**1.127**	**1.860**	-0.011	0.016	-0.051

It is interesting to observe that, regardless of the model picture of the historical precipitation trends, almost all GCMs simulate increasing summer precipitation trends in the Himalaya up to 2100 in both emission scenarios, and in most cases these trends are statistically significant (particularly for the RCP 8.5 scenario). The multi-model mean shows, for the Himalaya in summer, statistically significant increasing trends in 2006-2100 of about 1.13 mm/day per century (RCP 4.5) and 1.86 mm/day per century (RCP 8.5). The Himalayan region is therefore expected to experience a future, and overall significant, increase in total precipitation amounts during the monsoon season. In the Himalaya during winter, the MMM does not indicate significant precipitation trends in the future decades. Future projections of winter precipitation in the Himalayan region are much less clear than for summer. In the RCP 8.5 scenario, we find a slight prevalence of models giving statistically significant decreasing precipitation trends, but no conclusive considerations can be drawn from our analysis.

In the HKK region (Table 5.2), future precipitation projections in summer indicate, on average (MMM), a positive trend in both scenarios, statistically significant only in the RCP 8.5 hypothesis. Looking at the results of the individual models displaying statistically significant trends, it is interesting to note that, while in the RCP 4.5 scenario both positive and negative trends are simulated, in the RCP 8.5 scenario the statistically significant trends are all positive, indicating that, in this scenario, not only the Himalayan region, but also the HKK is expected to experience a future increase in summer precipitation. In the HKK region in winter, the MMM indicates negative precipitation trends throughout the historical period and the future decades. Future precipitation trends are statistically significant under the RCP 8.5 scenario.

Table 5.2. The same as Table 5.1, but for the HKK region.

	JJAS			DJFMA		
	Historical 1901-2005	RCP4.5 2006-2100	RCP8.5 2006-2100	Historical 1901-2005	RCP4.5 2006-2100	RCP8.5 2006-2100
Observations						
CRU	0.083			**0.399**		
GPCC	0.101			0.002		
CMIP5 models						
bcc-csm1-1-m	**0.544**	0.596	0.493	-0.091	0.126	-0.078
bcc-csm1-1	-0.061	0.158	0.054	-0.238	-0.198	0.011
CCSM4	-0.019	0.004	0.255	-0.264	-0.089	-0.292
CESM1-BGC	-0.352	0.522	-0.193	-0.271	-0.117	-0.529
*CESM1-CAM5	**0.550**	**-0.739**	0.054	-0.045	-0.058	0.226
EC-Earth	0.186	0.023	0.033	-0.013	**0.458**	0.344
FIO-ESM	0.335	0.116	0.184	-0.228	-0.506	**-1.141**
GFDL-ESM2G	-0.003	0.297	**0.674**	0.159	-0.070	0.025
GFDL-ESM2M	**0.628**	0.254	**0.613**	0.017	-0.126	0.044
MPI-ESM-LR	-0.013	-0.064	-0.258	-0.510	-0.528	**-1.140**
MPI-ESM-MR	-0.052	0.173	0.005	-0.286	0.199	**-1.010**
***CanESM2**	0.030	-0.104	0.011	0.000	-0.114	0.181
CMCC-CMS	0.261	-0.013	-0.129	-0.194	**-0.871**	**-0.840**
CNRM-CM5	0.040	-0.102	**0.338**	0.339	0.160	**0.989**
***CSIRO-Mk3-6-0**	0.079	0.143	-0.054	-0.242	**0.378**	**0.554**
***GFDL-CM3**	-0.071	**0.334**	0.296	0.039	-0.066	-0.398
INM-CM4	0.044	0.052	0.196	-0.178	-0.098	**-0.591**
IPSL-CM5A-LR	-0.009	**-0.287**	-0.120	-0.250	0.426	-0.600
IPSL-CM5A-MR	0.188	0.065	**0.300**	-0.373	0.469	-0.234
IPSL-CM5B-LR	-0.015	0.151	**0.633**	-0.106	0.476	**0.736**
***MRI-CGCM3**	**0.462**	-0.214	**0.470**	0.014	0.275	**1.117**
CMCC-CM	0.147	-0.045	0.073	-0.163	0.332	0.305
FGOALS-g2	0.055	**-0.204**	0.192	0.185	**-0.578**	**-0.608**
***HadGEM2-AO**	0.003	0.206	0.044	-0.128	0.254	**0.418**
***ACCESS1-0**	-0.133	**-0.423**	-0.196	0.181	0.013	0.167
***ACCESS1-3**	0.062	**-0.276**	-0.351	0.142	0.085	**0.300**
***HadGEM2-CC**	-0.243	0.189	0.142	-0.099	**0.345**	0.187
***HadGEM2-ES**	-0.206	**0.271**	0.265	-0.046	-0.009	0.242
***MIROC5**	**0.300**	0.238	**1.100**	-0.037	-0.017	-0.248
***MIROC-ESM**	-0.160	-0.216	0.002	0.019	-0.166	**-0.598**
***NorESM1-M**	-0.115	0.290	0.412	0.023	-0.131	-0.105
***NorESM1-ME**	**0.534**	0.281	0.425	0.308	**-0.452**	**-0.530**
MMM	**0.094**	0.054	**0.186**	**-0.073**	-0.006	**-0.097**

In order to analyse in detail how precipitation may change the near and farther future, we compare averages over the periods 2021-2050 and 2071-2100 with a 1971-2000 present-day reference period. In Figs. 5.3 and 5.4 we show the seasonal-mean percentage precipitation change in 2021-2050 relative to 1971-2000 (left column) and in 2071-2100 relative to 1971-2000 (right column) simulated by each GCM in the Himalaya and HKK regions, respectively. Results obtained in the RCP 4.5 (RCP 8.5) scenario are shown with the grey (black) histograms: filled histograms are used

for the models giving statistically significant differences between future and historical average conditions.

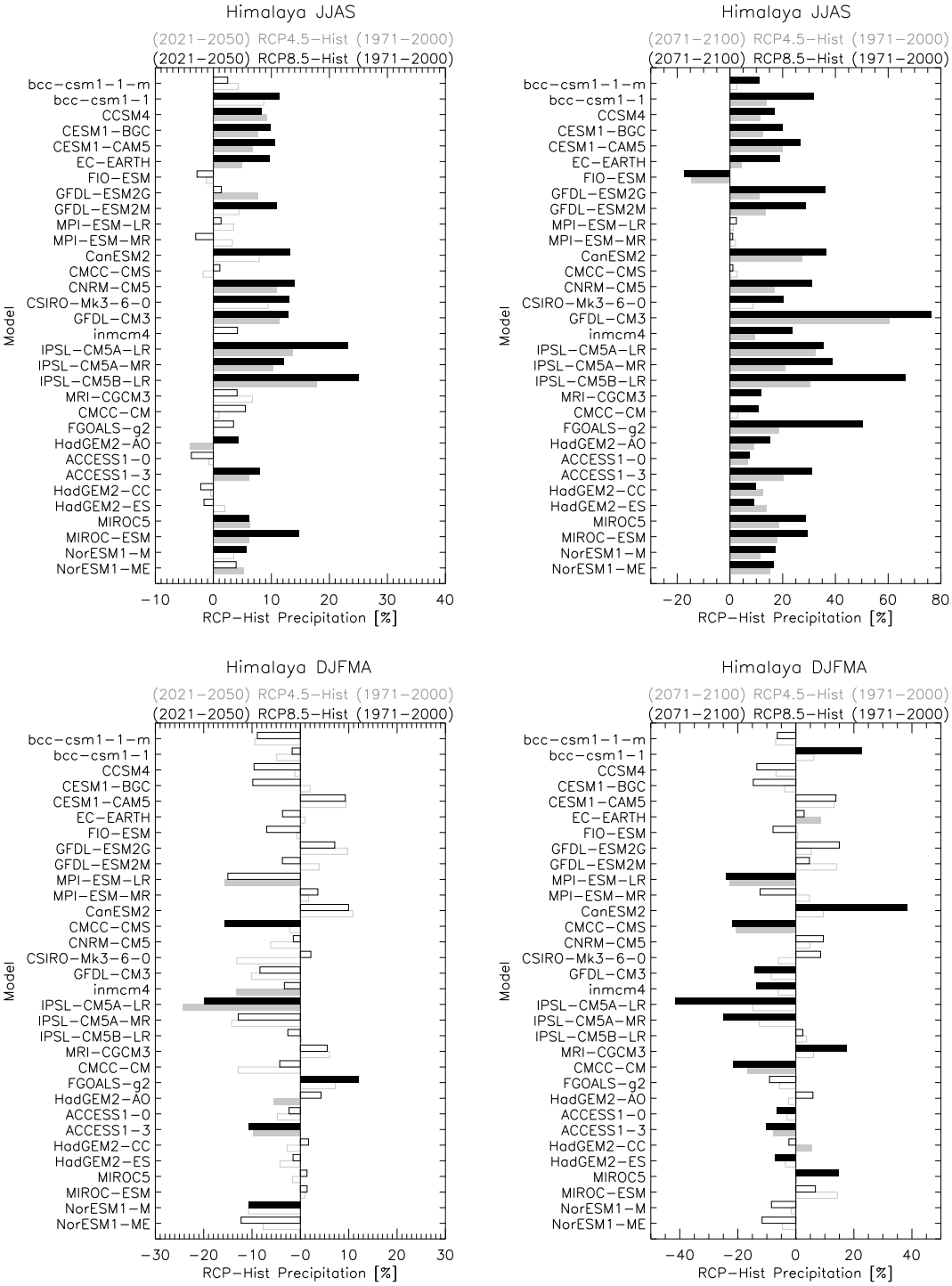

Figure 5.3: Percentage change in summer (top) and winter (bottom) precipitation in the Himalaya in 2021-2050 (left column), in the period 2071-2100 (right column) and the precipitation av- eraged over the historical reference period 1971-2000. For the models displaying statistically significant precipitation changes we use filled histogram

Twenty out of thirty-two models display statistically significant precipitation changes in 2021-2050 relative to 1971-2000 in the Himalaya during summer (top left panel of Fig. 2), either in the RCP 4.5 or RCP 8.5 scenario or (mostly) in both scenarios. For all these models (except HadGEM2-AO in the RCP 4.5 scenario) the simulated change is positive, indicating that the GCMs simulate a

wetter future in this region and season. Positive and statistically significant precipitation changes (ranging from less than ~10% to ~80% in the RCP 8.5 scenario) are also found in 2071-2100 relative to 1971-2000 for almost all models: only three GCMs (CMCC-CMS, MPI-ESM-LR, MPI-ESM-MR) - built on the same atmospheric model-, in fact, provide not-significant positive precipitation changes, while only one model (FIO-ESM) simulates significantly drier future conditions.

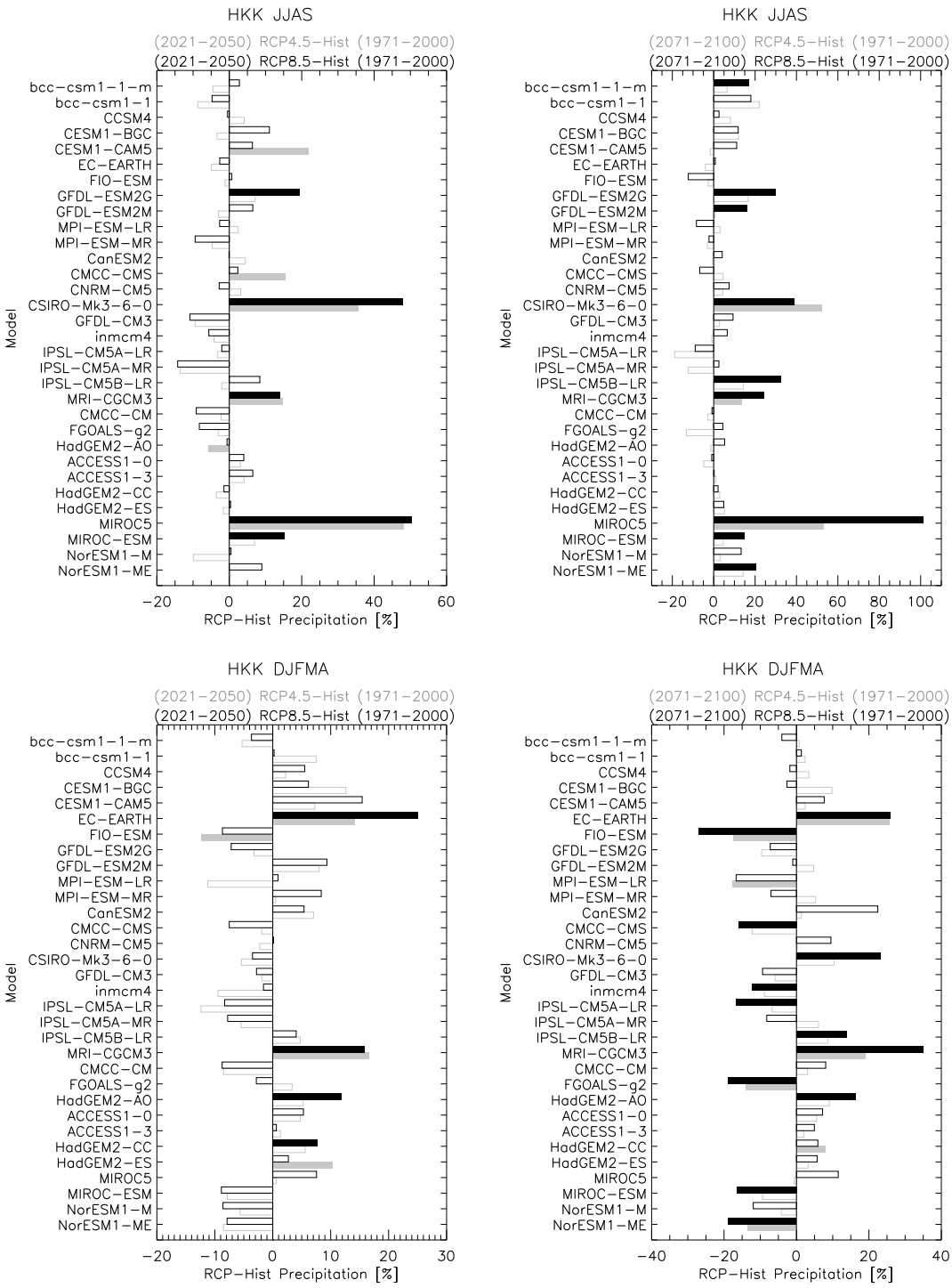

Figure 5.4: The same as Fig. 3 but for the HKK region.

Therefore, the CMIP5 models overall simulate a gradual increase of JJAS precipitation in the Himalaya throughout the twenty-first century, giving rise to positive precipitation changes in both the near and far future with respect to the historical (1971-2000) precipitation. A less clear signal

emerges for winter precipitation changes in the Himalaya. Only five models simulate statistically significant negative changes in 2021-2050 relative to 1971-2000, either in the RCP 4.5 and RCP 8.5 scenarios, while one model gives a positive, significant change. The number of GCMs simulating either positive or negative significant changes increases when the precipitation changes are evaluated in 2071-2100 relative to 1971-2000, with a slight prevalence towards a drier future under the RCP 8.5 scenario. The model picture of precipitation change in the HKK region indicates wetter conditions in summer in both 2021-2050 and 2071-2100, relative to 1971-2000, as well as positive winter precipitation changes in the nearest future. However, only a few models simulate statistically significant changes. Modeled winter precipitation change in 2071-2100 relative to 1971-2000 in the HKK is not homogeneous: a few models show significant wetter future conditions, a few others simulate a drier future (especially under the RCP 8.5 scenario). Overall, with respect to the Himalaya region, in the HKK a larger number of GCMs simulate no significant seasonal precipitation changes.

5.2.2 Future projections of snow depth in the HKKH region

The future changes of snow depth in the HKKH region are estimated considering only the five CMIP5 GCMs with highest resolution, being these models able to capture the more realistic distribution of snow depth and area in the HKKH mountains. For each model, the fields have been temporally averaged over the winter season (DJFMA) and spatially averaged in the two domains, HKK and Himalaya, weighting each pixel by its fraction of area above 1000 m a.s.l.

Figure 5.5 shows the average winter snow depth time series and the corresponding ensemble mean for the HKK and the Himalaya.

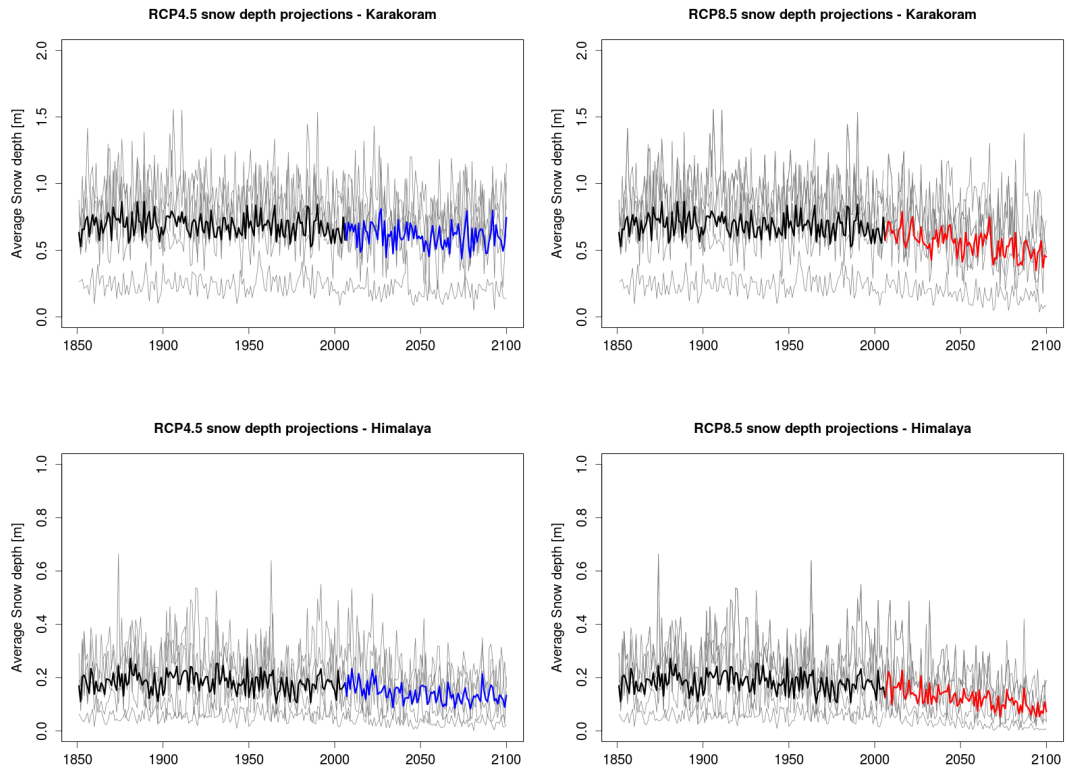

Figure 5.5: Winter snow depth projections for the historical period and for the 21st century (RCP4.5 and RCP8.5 scenarios) in Hindu-Kush Karakoram (top) and Himalaya (bottom), averaged by weighting by the fraction of area of each pixel with altitude above 1000 m a.s.l.. Gray lines represent high-resolution CMIP5 models, bold lines represent the ensemble means of historical (black), RCP4.5 (blue) and RCP8.5 (red) simulations.

In future projections, snow depth is found to significantly decrease in both regions and for both scenarios. The simulations for the Hindu-Kush Karakoram, in the RCP4.5 scenario, indicate a snow

depth decrease which is about twice stronger with respect to that estimated for the historical period (-5.5cm/100y); the more extreme RCP8.5 scenario indicates an even stronger, and highly significant, snow depth reduction of -19.2cm/100y. These are equivalent to respectively 8% and 28% reductions in snow depth per century, compared to the historical average. In the Himalaya, the models predict a strong and highly significant snow depth decrease of -5.4 cm/100y and -8.9 cm/100y in the RCP4.5 and RCP8.5 scenarios respectively (equivalent to decreases of 30% and 49% per century respectively). The expected relative decrease is much stronger in the Himalayan range, in agreement with previous studies that found Himalayan glaciers more sensitive to climate change.

Figure 5.6 shows the spatial patterns of the DJFMA snow depth trends for each of the high-resolution GCMs for the period 2006-2100 in the RCP8.5 scenario: future projections under this scenario indicate a clear signal emerging from all models, an overall snow depth decrease along all the Hindu-Kush Karakoram Himalaya mountain range.

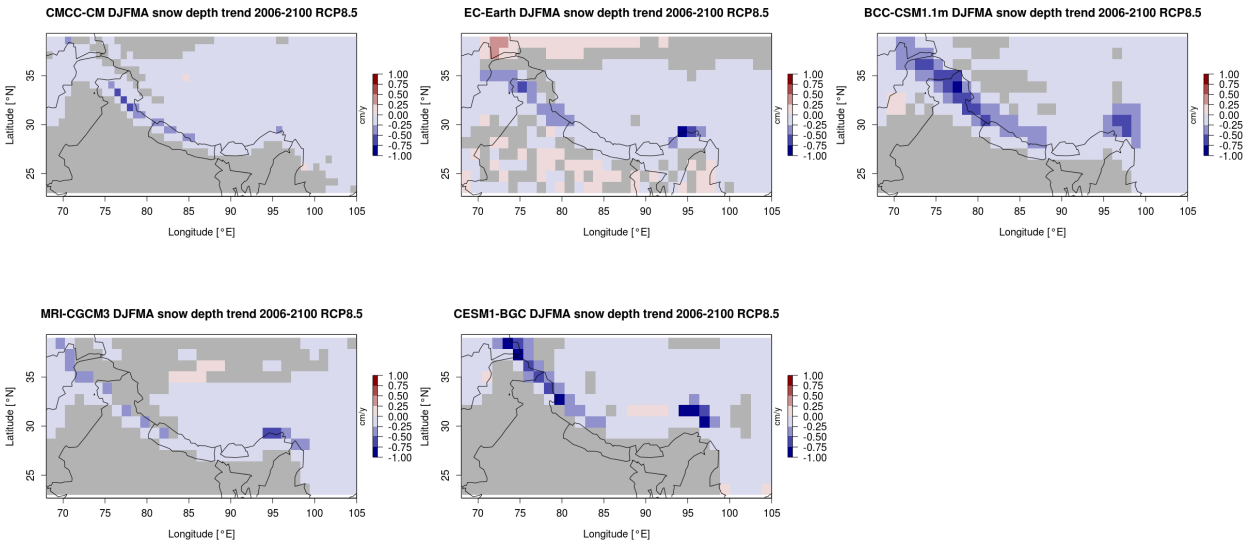

Figure 5.6: Projections of winter (DJFMA) snow depth trend over the period 2006-2100 (RCP8.5, 95% confidence level).

5.3. Hydrological projections

To evaluate future hydrological scenarios in the Karakoram region, the coarse-scale temperature and precipitation output of the EC-Earth projections (under the RCP 2.6, RCP 4.5, RCP 8.5 emission scenarios) has been downscaling. Precipitation downscaling, in particular, was performed using a random cascade approach (*e.g. Groppelli et al., 2011*).

The hydrological projections have been then obtained for the time period 2012-2100 by running the glacio-hydrological model driven by the high-resolution temperature and precipitation data obtained by downscaling the three EC-Earth projections. In order to evaluate future changes relative to present-day conditions, we have focused upon two reference future decades, namely 2045-2054, and 2090-2099.

The hydrological projections indicate future changes in different aspects of the hydrological cycle in the Shigar river basin, particularly in in stream flows, ice and snow cover, and accumulation within the catchment. Figure 5.7 shows the modified monthly discharge as per reference decade under the three considered scenarios. Annual mean discharge variations during 2045-2054 are projected to be positive, with an increase between +5% and +25% for the three RCP hypotheses. Towards the end of the century (2090-2099) the situation is expected to be similar in the RCP 4.5 and RCP 8.5 scenarios, while a negative variation is found in the most moderate RCP 2.6 scenario (-10%).

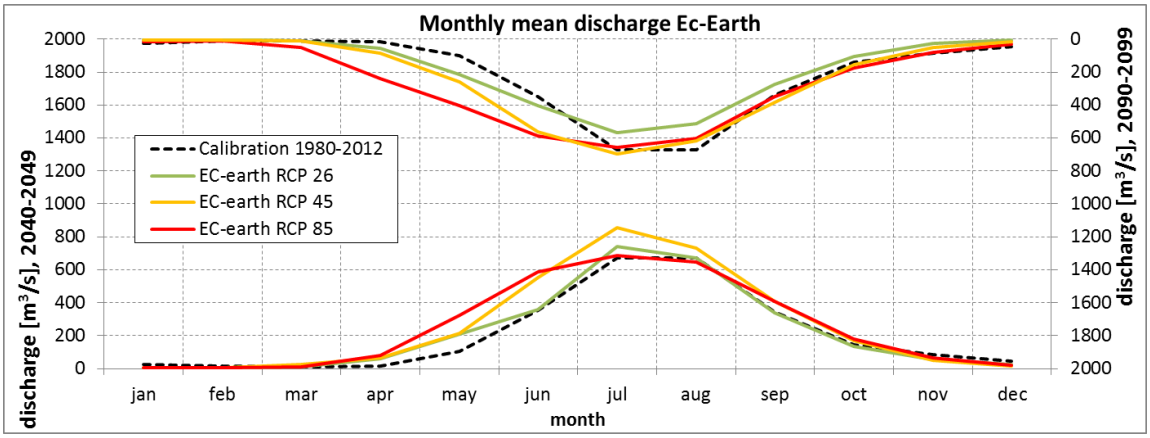

Figure 5.7: monthly mean discharge

Future snow cover area variations (SWE, m^3 of water) at October 1st, averaged over the two future reference decades (2040-2049, 2090-2099) are shown in Fig. 5.9.

Thick enough snow cover is a requisite for ice survival during Summer: our results indicate that the shielding effect of snow would decrease from moderately to largely until the end of the century. Our model provides ice area cover and approximate ice volume, and suggests that at mid-century ice cover area would remain quite constant with a slight change in ice volume (suggesting that the "Karakoram anomaly" might substantially persist in the near future).

Towards the end of the century, the three RCP scenarios provide different results concerning ice-covered areas (-22.92%, -22.92%, -45.36% on average, in the RCP 2.6, RCP 4.5, RCP 8.5, respectively), and ice volume (-63.87%, -76.55%, -91.00%). Thus, even with little to moderate area change, ice volume would decrease largely until the end of the century. Lack of ice cover would then start to impact in stream flows, which would start decreasing.

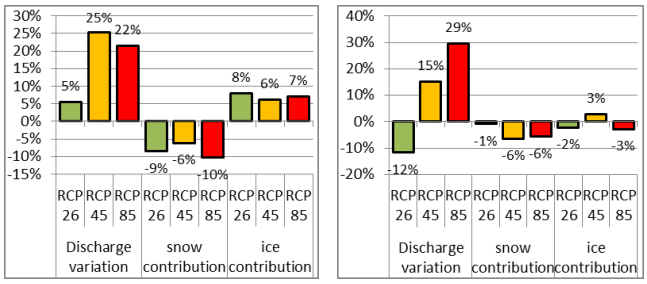

Figure 5.8: discharge, snow and ice contribution variations in a) 2040-2049 and b) 2090-2099

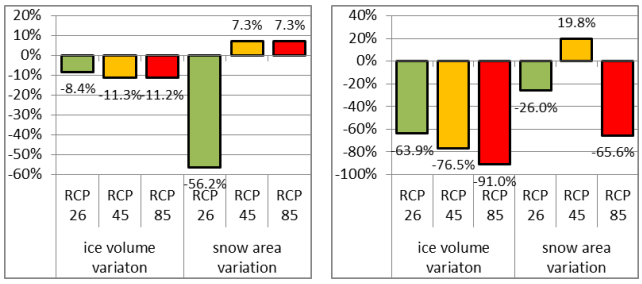

Figure 5.9: ice volume and snow covered area variations in a) 2040-2049 and b) 2090-2099

References

Groppelli, B., Soncini, A., Bocchiola, D. and Rosso, R., 2011. Evaluation of future hydrological cycle under climate change scenarios in a mesoscale Alpine watershed of Italy, Nat. Haz. Earth Sys. Scie., 11, 1769-1785.

Palazzi E, von Hardenberg J, Provenzale A (2013) Precipitation in the hindu- kush karakoram himalaya: Observations and future scenarios. J Geophys Res 118:85–100, DOI 10.1029/2012JD018697

WP6: Impacts and Adaptation (SEED Project)

Franco Mari (SEED)

E. Vuillermoz, G. P. Verza, M. Gallo, D. Milanesi, V. Carminati (EV-K2-CNR)

The SEED activities within PAPRIKA-Italy, also in collaboration with the KARAKORUM TRUST II project, were focused on the Central Karakoram National Park (CKNP) area, one protected area in the Karakoram region.
One of the most comprehensive and clear definition of a "Protected Area" was developed by IUCN-WCPA in 2007: *a clearly defined geographical space, recognized, dedicated and managed, through legal or effective means, to achieve the long-term conservation of nature with associated ecosystem services and cultural values*.

The first notification of the Central Karakorum National Park was made in 1993: it did not include, however, a clear definition of the Park boundaries and of the Protected Area internal zoning system, functional to define the management indications. A first revision of the Park boundaries was made three years later, in 1996.

As a preliminary step of the SEED activities within PAPRIKA-Italy, all the available data and information regarding the CKNP area were collected and analyzed, both in terms of scientific publications and technical documents, together with the various Management Plan implemented by different institutions during the years, but never approved formally at the institutional level.

Three main issues for the Park management were in particular tackled:

1. The lack of a clear boundaries delineation and internal zoning system.

2. The presence of laws and related rules (es. Wildlife Act, 1975) excluding all the traditional human activities; this was inadequate to support the necessity of the local communities highly dependent on natural resources.

3. The poor availability and/or reliability of data and their sparseness, making it difficult to evaluate the possible impact of climate change on the Park ecosystems. It is worth recalling that glaciers occupy about the 38% of the Park area, with a potential strong effect of glacierss modifications on local communities.

The SEED activities were aimed at identifying key thematic areas and related information requirement for the management of the CKNP. Specific aims were to improve the quality of life of the local communities and the conservation of environment, architectural and cultural heritage; enhance the capacity of local communities and institutions to adapt to climate change in the Central Karakorum area, by promoting sustainable development through the coordination of ongoing initiatives; strengthen the decision support system; strengthen institutional mechanisms to better manage the CKNP, and enhance capacity of local communities and institutions to face climate change.

To address these aims, the main actions, were focused on:

a) development and sharing of standardized inventory methodologies for the different research fields;

b) promotion of the research activities – on environment and social sciences - strongly oriented towards a management approach

c) data collection and analysis in selected study areas with an approach based on the use of a geographic information system (GIS)

d) set-up and use of an integrated modelling approach to produce mid- and long-term scenarios of future water availability and stream flow regimes, due to the high impact of these process on ecosystems and local communities.

A twofold research approach was employed:

- *Basic research*

The research aimed at providing products such as Digital Elevation Maps, Land cover maps, glacier inventories for the CKNP area, as well as modelling tools to better understand the impacts of claimte changes in the CKNP region.

- *Vertical and Horizontal research*

All research lines addressed to management issues and aimed at answering the needs for local communities, based on the background information coming from the basic research. As a first step, the vertical research activities were developed, focused on specific themes in the field of environmental and social sciences. Then, some horizontal research activities, based on a multidisciplinary approach and linking different vertical research activities were activated.

This approach led, in October 2012, to the first draft of the CKNP Management Plan the and related research protocols (Version 1.0). The final version (*Integrated Park Management Plan for CKNP - Version 1.1*), requiring a participatory approach, was released in March 2013, calling for a real restructuring of the CKNP through the definition of:

- New park's boundaries;
- A Core Zone and a Buffer Zone inside the Park boundaries;
- Core Zone and Buffer Zone internal zonation;
- Management indications within the different areas identified.

The CKNP boundaries and internal zonation and the related management indications contained in the Management Plan were shared and discussed with both institutional bodies and local communities living in the vicinity of the Park, giving rise to an evaluation and consultation process as shown in Figure 6.1.

This version of the Management Plan was provisionally approved by the Chief Secretary Gilgit Baltistan on November 6, 2013, to be eventually revised by the relevant Departments.

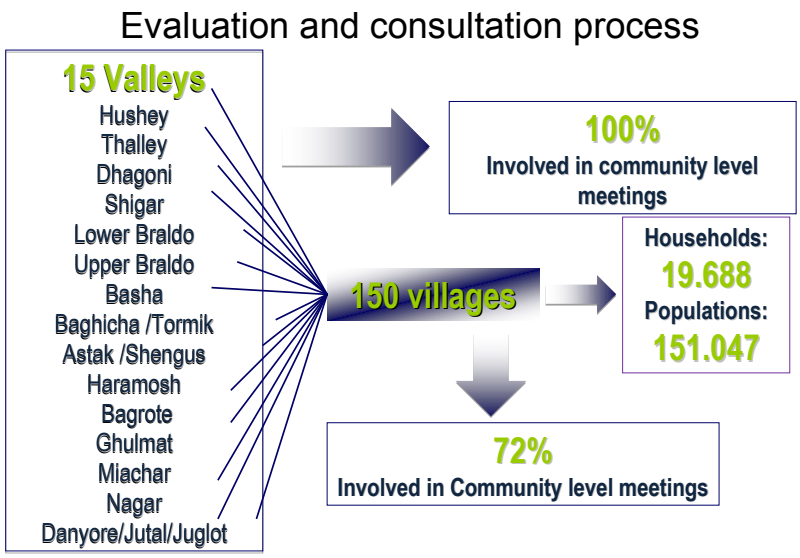

Figure 6.1. Diagram illustrating the evaluation and consultation process following the realization of the CKNP Management Plan.

WP7: Capacity Building

Elisa Vuillermoz (EV-K2-CNR)

YEAR 2010

Kick-off meeting of the PAPRIKA-HIMALAYA project

On March 12, 2010, the kick-off meeting of the PAPRIKA-France Project, focused on the Himalayan area, was held in Grenoble, France. Besides presenting the 3-years activity plan foreseen for the different work-packages, the interactions with the PAPRIKA-Italy project were also discussed, especially in terms of the exchange of measured data and model simulation outputs in the Khumbu region. One of the main scientific objectives of the two twin PAPRIKA projects was to achieve a better understanding of the impact of absorbing aerosols on glacier dynamics, through both experimental activities and climate model simulations,

First project meeting to identify partners and define the activity plan

A coordination meeting was held in summer 2010 to finalize the project document and the different research groups involved in the various activities. The identified partners and their main tasks were:

- CNR-ISAC (Institute of Atmospheric Sciences and Climate): Characterization of the physical properties and the chemical composition of the atmosphere, of the atmospheric circulation and climate patterns, of the hydrological cycle with particular emphasis on precipitation and snow, with both observations and models
- CNR-ISE (Institute for Ecosystem Studies): water quality
- University of Milan-Earth Sciences Department and Bavarian Academy of Sciences: cryospheric observations
- Polytechnic of Milan: hydrological modelling
- International Centre for Theoretical Physics (ICTP): new regional simulations with the RegCM4 regional climate model
- National Institute of Geophysics and Vulcanology (INGV): inspection of the Baltoro glacier ice thickness using radar system
- Euro-mediterranean center on climate change (CMCC) in collaboration with CNR-ISAC: climate and atmospheric variability simulations

Annual Meeting, December 13-14, 2010, Bergamo , Italy

On December 13-14, 2010 the first annual meeting of the PAPRIKA-Italy Project was held in Bergamo, to present the results of the first-year activities in the Karakoram and Himalaya regions. After presentations by the individual partners on their specific activities, an open discussion followed to facilitate the integration of the collected results, discuss further activities and eventually plan new research strategies..

YEAR 2011

Project meetings

- On January 25 and 26, 2011, a joint meeting between PAPRIKA-Italy and PAPRIKA-France was held in Grenoble, hosted by the LGGE-CNRS laboratory.

- On November 8, 2011 the second annual meeting of PAPRIKA Project was held in Bergamo. Researchers presented the results they obtained during the second year and shared the activity plan for the third year, in line with the objectives of the scientific program.

YEAR 2012

Project meetings

On November 30, 2012 the annual project meeting was held in Turin, hosted by CNR-ISAC.

Researchers presented their results on the following activities:

- Experimental campaigns, modeling activities and future hydrological scenarios in the framework of PAPRIKA (D. Bocchiola et al., Polytechnic of Milan);
- Inventory of glaciers in the Central Karakoram National Park (CKNP) and results of the summer 2012 glaciological campaign (A. Senese, University of Milan);
- Development of a RES system for the analysis of the Baltoro glacier (S. Urbini, INGV);
- Comparison of the 2011 and 2012 water chemistry data in the Shigar watershed (A. Lami, ISE-CNR)
- Measurements of atmospheric composition at Askole (Baltoro) during summer 2012 (P. Cristofanelli, ISAC-CNR);
- Analysis of meteorological data in the Baltoro and in northern Pakistan and interaction between western weather patterns and the monsoon (E. Palazzi and L. Filippi, ISAC-CNR);
- Atmospheric aerosol variability in the Himalayan Region (Silvia Bucci, CMCC);
- High-resolution non-hydrostatic simulations of extreme rainfall events: the case of Pakistan flood 2010 (A. Parodi, CIMA);
- An overview of regional climate simulations including aerosol in the context of PAPRIKA (F. Solmon, ICTP).

YEAR 2013

Alpine Summer school on Climate Change and the Mountain Environment, Valsavarenche, Valle d'Aosta (Italy), 18-28 June, 2013

Course directors: Antonello Provenzale, ISAC-CNR – Italy, Elisa Vuillermoz, Ev-K2-CNR – Italy, Isabella Zin, LGGE - France
Presentation of the Course: Mountains are the "sentinels of climate change" because they respond rapidly, and intensely, to climatic and environmental modifications. The report of the UN Conference on Sustainable Development (Rio+20, 2012, items 210-212) states that: "... the benefits derived from mountain regions are essential for sustainable development. Mountain ecosystems play a crucial role in providing water resources to a large portion of the world's population; fragile mountain ecosystems are particularly vulnerable to the adverse impacts of climate change, deforestation and forest degradation, land use change, land degradation and natural disasters; and mountain glaciers around the world are retreating and getting thinner, with increasing impacts on the environment and human well-being." Mountain areas are the "water towers" of entire regions: climatic and environmental alterations in the hydrological cycle in high mountains can have significant effects on the availability of water resources for energy production, agriculture, economy, urban settlements and societies living in the surrounding regions. It is therefore essential

to increase our knowledge of the current and expected modifications in high mountains, and use this knowledge to developed sustainable adaptation strategies and improve the quality of life of peoples living in the mountains.
This summer school is devoted to understanding how the mountain environment is changing in response to climate variability and the global temperature rise, with specific emphasis on monitoring current conditions, reconstructing past variability and develop projections for future decades. Specific focus themes of the lectures are: (1) atmospheric circulation and air quality in high-altitude areas, including the role of aerosols, pollution and the properties of precipitation; (2) changes in the hydrological cycle in mountain regions, with a specific attention to snow and glacier dynamics; (3) ecosystems and biodiversity in high-altitude areas and their response to climate and environmental change; and (4) reconstruction of past variability in mountain regions by ice and sediment core data; (5) climate modeling in mountain regions.

Lecturers and topics:

Introduction	
Antonello Provenzale	The specificity of the mountain environment
Theme 1: Atmospheric dynamics in mountain regions	
Roy Rasmussen	Principles of Orographic Winter Precipitation
	The Future of the Water Cycle in Complex Terrain
Klaus Fraedrich	Precipitation estimates in mountain regions: the example of the Tibetan plateau and more
Guoxiong Wu	Multi-Scale Forcing and the Formation of Subtropical Desert and Monsoon
	Impacts of the Tibetan Plateau on the Asian Climate
Angela Marinoni	Aerosols, impact on health and climate
	Aerosol in mountain environments
Elisa Vuillermoz	Field measurements in high-altitude regions
Elisa Palazzi	Precipitation in HKKH and Western Weather Patterns
Vincenzo Levizzani	Satellites, sensors, clouds and precipitation: What can/can't we observe?
	Advances in clouds and precipitation remote sensing
Theme 2: Hydrological cycle in the mountains	
Isabella Zin	Hydrological cycle in the mountains - including scale interactions
Bodo Bookhagen	The role of hydrology and sediment flux from mountain catchments for downstream regions
	What are the key contributing factors to discharge in mountain catchments and how can we measure them?
Samuel Morin	Snow on the ground : observation and understanding of physical properties

	and their time evolution
	Snow on the ground : implementation of physical processes into numerical modeling platforms of various levels of complexity for a diversity of mountain applications
Vincent Favier	Glacier monitoring and glacier modeling
Theme 3: Ecosystems and biodiversity	
Sandra Lavorel	Biodiversity patterns and processes in high altitude areas
	Impacts of climate change on mountain biodiversity and ecosystem services. From observations to scenarios
Marino Gatto	Mountain ecosystem dynamics and climate change
Graziano Rossi	Climate and vegetation
Ramona Viterbi	Measurements of biodiversity in the Italian Alps
Giovanni Amori	Predator-prey dynamics and climate change in the mountains
Theme 4: Past climate variations in mountain regions	
Valter Maggi	Sources and transport of atmospheric mineral dust
	Paleoclimatic and climatic effects of mineral dust
Carlo Barbante	Climatic Archives: reconstructing the climate of the past
	Climate proxies in terrestrial and marine archives
Theme 5: Climate modelling in mountain regions	
Antonio Parodi	Non-hydrostatic models in mountain regions and scenario simulation of severe hydro-climatological events
Dieter Kranzlmüller	Hydrometeorological and hydroclimatological science on European e-Infrastructures
Antonello Provenzale	The problem of small-scale climate projections and downscaling methods
Martin Beniston	Climate projections for the Alps: Modeling issues
	Climate projections for the Alps: Assessing extremes and impacts in the Alps

PAPRIKA Publications 2010-2013

Bocchiola, D., Diolaiuti, G., Soncini, A., Mihalcea, C., D'Agata, C., Mayer, C., Lambrecht, A., Rosso, R., Smiraglia, C.: Prediction of future hydrological regimes in poorly gauged high altitude basins: The case study of the upper Indus, Pakistan (2011) Hydrology and Earth System Sciences, 15 (7), pp. 2059-2075.

Bocchiola, D., Diolaiuti, G.: Recent (1980-2009) evidence of climate change in the upper Karakoram, Pakistan (2013) Theoretical and Applied Climatology, 113 (3-4), pp. 611-641.

Bonasoni, P., Cristofanelli, P., Marinoni, A., Vuillermoz, E., Adhikary, B. Atmospheric pollution in the Hindu Kush-Himalaya region (2012) Mountain Research and Development, 32 (4), pp. 468-479.

Bucci, S., Cagnazzo, C., Cairo, F., Di Liberto, L., and Fierli, F.: Aerosol variability and atmospheric transport in the Himalayan region from CALIOP 2007–2010 observations, Atmos. Chem. Phys. Discuss., 13, 15271-15299, doi:10.5194/acpd-13-15271-2013, 2013

Mayer, C., Lambrecht, A., Mihalcea, C., Bel, M., Diolaiuti, G., Smiraglia, C., Bashir, F. Analysis of glacial meltwater in Bagrot Valley, Karakoram (2010) Mountain Research and Development, 30 (2), pp. 169-177.

Minora, U., Bocchiola, D., D'Agata, C., Maragno, D., Mayer, C., Lambrecht, A., Mosconi, B., Vuillermoz, E., Senese, A., Compostella, C., Smiraglia, C., and Diolaiuti, G.: 2001–2010 glacier changes in the Central Karakoram National Park: a contribution to evaluate the magnitude and rate of the "Karakoram anomaly", The Cryosphere Discuss., 7, 2891-2941, doi:10.5194/tcd-7-2891-2013, 2013.

Palazzi, E., J. von Hardenberg, and A. Provenzale (2013), Precipitation in the Hindu-Kush Karakoram Himalaya: Observations and future scenarios, J. Geophys. Res. Atmos., 118, 85–100, doi: 10.1029/2012JD018697.

Provenzale, A. (2011): The Ev-K2-CNR SHARE Project PAPRIKA- Karakoram: Cryospheric responses to anthropogenic pressures in the Hindu Kush-Karakorum-Himalaya region: impacts on water resources and availability. Le modificazioni climatiche e i rischi naturali, Polemio M. (Ed), ISBN 9788890508806, CNR IRPI, Bari 2011.

Submitted and/or under revision

Putero, D., P. Cristofanelli, P. Laj, A. Marinoni, P. Villani, A. Broquet, M. Alborghetti, U. Bonafè, F. Calzolari, R. Duchi, T.C. Landi, G. P. Verza, E. Vuillermoz and P. Bonasoni. New atmospheric composition observations in the Karakorum region: influence of local emissions and large-scale circulation during a summer field campaign. Submitted to Atmospheric Environment

Soncini, A.; D. Bocchiola; G. Confortola; A. Bianchi; R. Rosso; C. Mayer; A. Lambrecht; E. Palazzi; C. Smiraglia; G. Diolaiuti: Future hydrological regimes in the upper Indus basin: a case study from a high altitude glacierized catchment, Submitted to Journal of Hydrometeorology.

Terzago, S., J. von Hardenberg, E. Palazzi, A. Provenzale, Snow depth changes in the Hindu-Kush Karakoram Himalaya from CMIP5 Global Climate Models, under revision for Journal of Hydrometeorology